

Efficient Meso-Scale Modeling of Alkali-Silica-Reaction Damage in Concrete

Présentée le 9 décembre 2021

Faculté des sciences et techniques de l'ingénieur
Laboratoire de modélisation mécanique multi-échelle
Programme doctoral en mécanique

pour l'obtention du grade de Docteur ès Sciences

par

Ali FALSAFI

Acceptée sur proposition du jury

Prof. B. T. A. Lecampion, président du jury
Prof. W. Curtin, T. Junge, directeurs de thèse
Prof. J. Segurado, rapporteur
Prof. D. Kochmann, rapporteur
Dr G. Anciaux, rapporteur

Acknowledgements

This thesis reflects the outcome of my rewarding stay as a Ph.D. student at the **Laboratory for Multi-scale Mechanics Modeling (LAMMM)** at the **École Polytechnique Fédérale de Lausanne (EPFL)**. My doctoral research was made possible by a Ambizione grant 174105 entitled *Open-Source Platform for Efficient FFT-based Continuum Mesoscale Modelling* from the **Swiss National Science Foundation**. Here are a few words of thanks to conclude this very interesting and life-changing scientific journey.

My deepest gratitude is extended first and foremost to my thesis advisor, Dr. Till Junge, who has provided me with guidance, trust, and support throughout my studies. Having his mentorship and encouragement has enabled me to continue my academic journey. Having the opportunity to work with him has been an honor and a pleasure. I would also like to express my gratitude to Prof. William Curtin for his support and supervision during my PhD research. It is through his insight that all LAMMM members feel confident about their research.

I am also grateful to our collaborators on μ spectre project; Prof. Lars Pastewka. Richard J. Leute, and Indre Jödicke from Albert-Ludwigs-Universität Freiburg; and Prof. Jan Zeman, Prof. Ivana Pultarová and Dr. Martin Ladecký from the Czech Technical University in Prague. Without their collaboration and assistance, I would not have been able to conduct this research. I am particularly thankful to Martin Ladecký for fruitful discussions on the mathematical foundations of this research.

In addition, I would like to thank the jury members for participating in my PhD examination and their thoughtful comments and questions. I am also thankful to the current and former members of LAMMM: Mostafa Khosrownejad, Francesco Maresca, Wolfram Nöhring, Max Hodapp, Ali Tehranchi, Markus Stricker, Binglun Yin, Predrag Andric, Xiao Zhou, Carolina Baruffi, Manura Liyanage, You Rao, Rasool Ahmad, Alireza

Acknowledgements

Ghafarollahi, Ankit Gupta, Yi Hu, Eleanor Mak, Daniel Marchand, Shankha Nag, Ekin Kubilay, Xin Liu, Terrence Moran, and Masoud Rahbarniazi. I also wish to thank the ever smiling secretary of LAMMM, Ms. Géraldine Palaj, for her diligent work and assistance on daily issues. I've been fortunate to work with such a wonderful group of people.

My sincere gratitude extends to my parents, Tahmineh and Esmaeil as well as my siblings, Nader, Nazi, Nima, and Negar. Thank you also to my in-laws, Boshra and Mehrdad, for their support and kindness.

Last but not least, I would like to express my gratitude and dedicate this work to my wife, Shekoofeh. Her presence has been a pillar of support and reliance for me through good times and tough times. As a companion, she has provided me with innumerable forms of unconditional love, support, and assistance. The completion of this thesis would not have been possible without her continued patience, support, and encouragement.

Lausanne, September 28, 2022

A. F.

Abstract

The alkali-silica reaction (ASR), also known as concrete cancer, is one of the most prevalent causes of concrete degradation. In this chemical reaction, amorphous silica in the aggregates reacts with alkalis in the pore solution. By absorbing water, hydrophilic ASR products generate highly localized internal pressure that causes expansion and cracking. The detrimental effects of ASR on concrete pose a major threat to the safety and operability of concrete infrastructure in all parts of the world.

The long lifespan of concrete structures and their high economic significance make it crucial to evaluate the effect of ASR-induced degradation. ASR has therefore been the subject of extensive research over the past few decades. Modeling and experimental studies have provided fundamental insight into the physics of ASR at the meso-scale of concrete. However, the impact of the mesoscopic ASR damage evolution on the macro-scale, or structural scale, on concrete is not well understood yet. Investigating the structural outcome of the ASR damage necessitates robust meso-scale solvers faster than the existing meso-scale models that conventionally use finite element method (FEM) as the solution scheme.

Over the past 30 years, fast Fourier transform (FFT)-based methods have gained much attention as fast and reliable alternatives to conventional FEM solvers because they can exploit regular grid structures, use lightweight iterative solvers, and speed up meso-scale simulations by orders of magnitude. However, it has not been feasible to effectively utilize them in damage mechanics problems due to two shortcomings: ringing artifacts and incapability to solve non-elliptic problems, in their recent efficient implementations, where conjugate gradient (CG) is used as the linear solver.

In the present thesis, we have resolved the shortcomings of the FFT-based solution scheme for being effectively used in damage mechanics problems. All of the developed methods are implemented in an open-source FFT-accelerated software package capable

Abstract

of solving generic homogenization problems for other use cases as well. The developed library is capable of solving non-convex problems (non-elliptic partial differential equation (PDE)) containing phases with extremely high contrast with a ringing-free scalable FFT-accelerated solver.

The developed fast and robust numerical framework is employed to conduct ASR meso-scale simulations. The obtained results show good agreement with the results obtained using the conventional FEM solver. The developed solution scheme is 200 times faster than the solution of the same problem with conventional FEM solvers. Therefore, it enables comprehensive multi-scale structural ASR damage modeling with reasonable computational costs.

Keywords: Alkali-Silica Reaction, FFT-accelerated homogenization, Non-convex solvers, Ringing-free spectral solver, FFT-accelerated solver with FEM discretization, Preconditioned FEM

Zusammenfassung

Die Alkali-Kieselsäure-Reaktion (AKR), auch bekannt als Betonkrebs, ist eine der häufigsten Ursachen für die Zerstörung von Beton. Bei dieser chemischen Reaktion reagiert amorphes Siliziumdioxid in den Zuschlagstoffen mit Alkalien in der Porenlösung. Durch die Absorption von Wasser erzeugen hydrophile AKR-Produkte einen hohen lokalisierten Innendruck, der zu Ausdehnung und Rissbildung führt. Die nachteiligen Auswirkungen der AKR auf Beton stellen eine große Gefahr für die Sicherheit und die Funktionsfähigkeit von Betoninfrastrukturen in allen Teilen der Welt.

Die lange Lebensdauer von Betonbauwerken und ihre hohe wirtschaftliche Bedeutung machen es entscheidend, die Auswirkungen der AKR-induzierten Degradation zu bewerten. AKR ist daher in den letzten Jahrzehnten Thema umfangreicher Forschungsarbeiten gewesen. Modellierung und experimentelle Studien haben einen grundlegenden Einblick in die Physik der AKR im Mesomaßstab des Betons geliefert. Allerdings sind die Auswirkungen der mesoskopischen AKR-Schadensentwicklung auf die Makroebene bzw. die strukturelle Skala des Betons, ist noch nicht gut verstanden. Die Untersuchung der strukturellen Ergebnisse des ASR-Schadens erfordert eine robuste Mesoskala Löser, die schneller als die bestehenden mesoskaligen Modelle (die herkömmlich FEM als Lösungsschema verwenden) sind.

In den letzten 30 Jahren haben FFT-basierte Methoden viel Aufmerksamkeit als schnelle und zuverlässige Alternativen zu konventionellen FEM-Lösern gewonnen. Der Grund dafür ist, dass sie regelmäßige Gitterstrukturen ausnutzen können, leichtgewichtige iterative Löser verwenden und Simulationen im Meso-Maßstab um Größenordnungen beschleunigen. Allerdings ist es bisher nicht durchführbar, sie bei Problemen der Schadensmechanik effektiv zu nutzen, da zwei Unzulänglichkeiten: Ringing-Artefakte und die Unfähigkeit, nicht-elliptische Probleme zu lösen, wenn CG als linearer Löser verwendet wird.

In der vorliegenden Arbeit haben wir die Unzulänglichkeiten des FFT-basierten Lösungs-

Zusammenfassung

schemas für den effektiven Einsatz bei Problemen der Schadensmechanik gelöst. Alle entwickelten Methoden sind in einem quelloffenen, FFT-beschleunigten Softwarepaket implementiert, das in der Lage ist, generische Homogenisierungsprobleme zu lösen. Die entwickelte Bibliothek ist in der Lage, nicht-konvexe Probleme (nicht elliptische PDE) enthalten extrem hoch kontrastierte Phasen mit einem schwingungsfreien, skalierbaren FFT-beschleunigten Löser zu lösen.

Der entwickelte schnelle und robuste numerische Rahmen wird zur Durchführung von ASR-Simulationen im Meso-Maßstab eingesetzt. Die erzielten Ergebnisse zeigen eine gute Übereinstimmung mit den Ergebnissen, die mit dem herkömmlichen FEM-Löser erzielt wurden. Das entwickelte Lösungsschema ist etwa 200-mal schneller als die Lösung desselben Problems mit herkömmlichen FEM-Solvern. Daher ermöglicht es eine umfassende mehrskalige strukturelle AKR Schadensmodellierung mit angemessenen Rechenkosten.

Stichwörter: Alkali-Kieselsäure-Reaktion, FFT-beschleunigte Homogenisierung, Nicht-konvexe Löser, Ringing-freier Spektral-Löser, FFT-beschleunigter Löser mit FEM-Diskretisierung, Vorkonditionierte FEM

Résumé

La réaction alcali-silice (RAS), également connue sous le nom de cancer du béton, est l'une des causes les plus courantes de la dégradation interne du béton. Dans cette réaction, la silice amorphe des agrégats réagit avec les alcalis présents dans la solution des pores. En absorbant l'eau, les produits hydrophiles de la RAS génèrent une pression interne très localisée qui provoque l'expansion du béton et sa fissuration. Les effets néfastes de la RAS constituent une menace majeure pour la sécurité et l'exploitabilité des infrastructures en béton dans toutes les régions du monde. La durabilité des structures en béton et leur grande importance économique rendent cruciale l'évaluation de la dégradation du béton induite par la RAS.

La RAS a donc été l'objet de recherches approfondies au cours des dernières décennies. Des études expérimentales et de modélisation ont fourni des informations fondamentales sur la physique de la RSA à l'échelle méso. Cependant, l'impact à l'échelle macro - ou échelle structurelle - de l'évolution mésoscopique des dommages causés par le RAS n'est pas encore bien compris. L'étude des conséquences structurelles des dommages causés par la RAS nécessite l'utilisation des solveurs à l'échelle méso plus rapides que ceux existants, typiquement basés sur la méthode des éléments finis (FEM). Au cours des 30 dernières années, les méthodes basées sur la transformée de Fourier rapide (FFT) ont gagné beaucoup d'attention en tant qu'alternatives rapides et fiables aux solveurs FEM conventionnels, car elles peuvent exploiter des structures de grille régulières, utiliser des solveurs itératifs légers, et accélérer les simulations à méso-échelle. Cependant, il n'a pas été possible de les utiliser efficacement dans les problèmes de mécanique de l'endommagement en raison de deux inconvénients : les artéfacts d'oscillations parasites et l'incapacité à résoudre des problèmes non-elliptiques.

Dans la présente thèse, nous avons résolu les défauts du schéma de solution basé sur la FFT pour leur utilisation efficace dans les problèmes de mécanique de l'endommagement. Toutes

Résumé

les méthodes développées sont implémentées dans un logiciel open-source capable de résoudre des problèmes d'homogénéisation génériques. La librairie développée est capable de résoudre des problèmes non convexes (non-elliptiques PDEs) avec un solveur accéléré par FFT sans oscillations parasites. Le schéma numérique développé, rapide et robuste, est employé pour réaliser des simulations méso-échelle de la RAS. Les résultats obtenus montrent un bon accord avec les résultats obtenus en utilisant le solveur conventionnel FEM. Le schéma numérique développé est 200 fois plus rapide que la solution du même problème avec les solveurs FEM conventionnels. Par conséquent, il permet de modéliser des dommages structuraux multi-échelles de manière exhaustive et avec des coûts de calcul raisonnables.

Mots-clés : Réaction alcali-silice, homogénéisation accélérée par FFT, solveurs non convexes, solveur spectral sans oscillations parasites, solveur accéléré par FFT avec discrétisation FEM, FEM préconditionnée.

Contents

Acknowledgements	i
Abstract (English/Deutsch/Français)	iii
List of Figures	xi
List of Tables	xiv
Introduction	1
Motivation and objectives	1
Outline	3
1 State of the art computational homogenization	7
1.1 Notation	13
1.2 Nonlinear small-strain elasticity	13
1.3 Strain-based (projection-based FFT-accelerated) scheme	15
1.3.1 Projection operator	17
1.3.2 Discretization	18
1.3.3 Linearization	20
1.4 Displacement-based (preconditioned FFT-accelerated FEM) scheme	22
1.4.1 Discretization	22
1.4.2 Linearization	24
1.4.3 Preconditioning	25
1.4.4 Preconditioner inversion	27
2 State of the art ASR simulation	29
2.1 ASR process	29

ix

Contents

2.2	ASR simulation	31
3	Voigt and laminate homogenized pixels	37
3.1	Derivation	38
3.1.1	Voigt homogenization	39
3.1.2	Laminate homogenization	40
3.2	Examples and results	46
3.2.1	Inclined square inclusion example	47
3.2.2	Circular square inclusion example	48
3.2.3	Simple square example	50
3.3	Conclusion	53
4	Equivalence of the strain-based and displacement-based schemes	55
4.1	Derivation	58
4.1.1	Projection operator with a reference material	59
4.1.2	Termination criterion	61
4.2	Examples and Result	64
4.2.1	Homogenization of a hyper-elasto-plastic micro-structure	64
4.3	Conclusion	67
4.4	Algorithms	68
5	Non-Convexity	71
5.1	Method	72
5.1.1	Trust region solver	72
5.2	Examples and Results	79
5.2.1	Minimal 1-dimensional (1D) non-convex example	79
5.2.2	Convex example	81
5.3	Conclusion	86
5.4	Algorithms	87
6	Algorithmically consistent tangent for the strain-based FFT-accelerated scheme	89
6.1	Derivation	90
6.2	Examples and results	96

6.2.1	Comparison with the analytical solution of Eshelby	96
6.2.2	Stiffness reduction of cracked solids	98
6.2.3	Homogenization of a Hyper-elasto-plastic micro-structure	100
6.2.4	Homogenization of an Neo-Hookean elastic representative volume element (RVE)	102
6.3	Conclusion	103
7	Meso-scale Alkali-Silica reaction damage simulation	105
7.1	RVE preparation	106
7.2	Constitutive laws	108
7.3	Stress control in spectral methods	117
7.4	Simulation and results	119
7.5	Conclusion	128
8	Conclusion	131
8.1	Summary and conclusions	131
8.2	Perspectives	133
	Bibliography	135
	Abbreviations	148
	Curriculum Vitae	

List of Figures

1	multi-scale simulation scheme alkali silica reaction induced damage . . .	4
1.1	Regular and irregular meshes at interface boundaries	9
1.2	Hourglass mode	10
1.3	Arbitrary displacement expression in voxel grid	10
1.4	Crack pattern in a concrete micro-structure, with and without ringing .	11
1.5	2D cell illustration	14
1.6	Regular finite element meshes	21
2.1	Alkali silica reaction across scales	31
2.2	Alkali silica reaction: a chemo-mechanical process	32
3.1	Laminate homogenization scheme	41
3.2	Inclined square example geometry	47
3.3	Square inclusion problem strain response	49
3.4	Square inclusion problem stress response	49
3.5	Circular inclusion example geometry	50
3.6	Circular inclusion example strain response	51
3.7	Circular inclusion example stress response	52
3.8	Simple square example solution step count	52
4.1	Global plastic strain of a two-phase elasto-plastic RVE	66
5.1	Schematic of trust region method in a 2-dimensional (2D) state space .	73
5.2	1D spring example schematic	81
5.3	1D spring example results	82
5.4	Cylindrical Eshelby example geometry and solution	84

List of Figures

5.5	Cylindrical Eshelby example solution step count	85
6.1	Spherical inclusion bulk and shear modulus	98
6.2	Geometry of a solid domain containing a single crack	99
6.3	Effective tangent of the single cracked solid domain	100
6.4	Effective tangent calculation error of the hyper-elasto-plastic example .	101
6.5	Error and time consumption of Effective tangent computation of the Neo-Hookean example	103
7.1	2D concrete micro-structure	108
7.2	Schematic of the damage constitutive law	115
7.3	Alkali silica reaction crack evolution	120
7.4	Discretization and load step study of alkali reaction silica damage . . .	122
7.5	Schematic stress-strain response of a bilinear strain-softening damage constitutive law	123
7.6	Stiffness reduction of concrete microstructures due to Alkali silica reaction damage with zero mean stress	126
7.7	Stiffness reduction of concrete microstructures due to Alkali silica reaction damage under uniaxial stress	127
7.8	Crack pattern for different regular finite element discretizations	128

List of Tables

3.1	interlaminar and intralaminar categorization of tensor components . . .	42
3.2	Blocks of the stiffness tangent based on the type of the components . . .	44
4.1	Solution step count for solution schemes and different reference materials	67
5.1	Solvers used to solve the 1D spring example	80
7.1	Material properties of concrete phases	121

Introduction

Motivation and objectives

The alkali-silica reaction (ASR) is the most common type of the alkali-aggregate reaction, which occurs when silica within concrete aggregates react with alkaline of concrete pore solution. ASR manifests itself at the scale of an aggregate in the form of local silica dissolution; expansion of ASR products; initiating micro-cracks; and the expansion of the aggregates, cement paste, and concrete. Cracking and expansion caused by ASR impact negatively on the civil engineering infrastructure including bridges and concrete dams worldwide. ASR consequences have considerable financial implications for large structures like dams, bridge piers, and sea walls. It is therefore necessary to study ASR in order to have a better understanding of its process, predict its severity in the existing structures, determine if any remedial action is necessary and also prevent its manifestation in new structures

Clusters of alkali-silicate gel are formed as a result of the ASR products accumulating inside pre-existing cracks (Gaboriaud et al. (2002)). The newly formed alkali-silicate clusters are referred to as pockets. The expansion of ASR gel pockets, due to their water absorption, cause internal loading on aggregates, which can lead to cracking. The resulting cracks originate in the aggregates and extend into the cement paste. The openings of induced cracks could be much larger than those of the pre-existing cracks and the initial ASR gel pocket sizes. As the ASR process advances, its outcomes, expansion and cracks also reveal in the structural scale. The Swiss Committee on Dams (Sellier et al. (2017)) reported that approximately 50% of 154 Swiss dams are affected by this problem. As engineering structures of great economic significance, dams is the focus of

discussions about the macro-scale effects of ASR.

Field observations and experimental data suggest that ASR involves a combination of multiple phenomena that occur at the same time and chemical, structural, and environmental factors are all involved in this process. It is indispensable to use numerical modelling in order to understand and predict the behavior of such a complex system. Results obtained by Dunant and Scrivener (2010); Cuba Ramos (2017) show that the meso-scale and macro-scale damage processes can not be separated in modeling ASR damage. At the structural scale, a model of a concrete dam with sufficiently fine discretization size yields $10^{14} - 10^{15}$ elements (discretizing a concrete dam with volume of 10^6 m^3 to elements with size of 1 mm^3). This makes full resolution of structural ASR damage modeling unfeasible with existing computational infrastructure. Multi-scale modeling (as depicted in Figure 1) reduces the complexity of the model. Finite element method (FEM) is commonly used for both micro-scale and macro-scale simulations, resulting in FE squared (FE^2) schemes. Despite using the FE^2 model to model ASR, multi-scale modeling is still extremely computationally challenging due to the large gap between the spatial scale of the ASR gel formation and initiating damage at microscopic scale and the scale of the concrete dam structure. As a result of the simple and regular structure of the meso-scale model, schemes such as fast Fourier transform (FFT)-accelerated schemes can be used to accelerate the solution process.

Continuum meso-scale modeling (or computational homogenization) involves computing the overall response of periodic unit cells of material, a representative volume element (RVE), to an average strain (i.e., macroscale). FEM is commonly used for this purpose. However, generally, FFT-accelerated solvers are computationally advantageous since unlike FEM they can leverage the simplicity of the geometry of the regular periodic solution domain. On the other hand FEM cannot benefit from its main strength, the capability of handling complex geometries. By introducing spectral methods, Moulinec and Suquet (1994) have developed a faster alternative method for modeling periodic RVEs compared to FEM. In terms of computation cost and memory footprint, this new method is considerably superior to FEM for solving the core problem of computational homogenization (Eisenlohr et al. (2013)), but has not been fully exploited yet for the present problem.

Specifically, for meso-scale ASR damage modeling the following characteristics of the problem make use of FFT-accelerated schemes challenging: i. ringing artifacts ubiquitous in the FFT-accelerated solution schemes make the results of continuum damage modeling non-physical, ii. In the modern and efficient implementations FFT-accelerated solver, employed iterative solvers (e.g. conjugate gradient (CG)) are incapable of handling non-convex problems such as damage mechanics. Note that the solver (fixed-point) originally used by Moulinec and Suquet (1994) despite its capability of handling non-convexity suffers from other major issues like conditional convergence and also cannot cope with cell containing phases with high contrasts. Overcoming these problems enables to reduce the complexity of a multi-scale ASR damage modeling to $10^6 - 10^7$ instead of $10^{14} - 10^{15}$ in a fully resolved FEM model, which makes ASR damage modeling feasible.

The goal of this project is to overcome and resolve the existing challenges in meso-scale modeling of ASR damage with the FFT-accelerated homogenization scheme. This creates the possibility of fast and efficient ASR damage modeling. In addition, a robust and fast algorithmic consistent tangent evaluation scheme is introduced in this thesis. Besides, all the developed and introduced methods are implemented in an open source software package μ Spectre. The μ Spectre project, is an open-source platform for efficient FFT-based continuum mesoscale modeling (Junge et al. (2022)) applicable to solve generic homogenization problems.

Outline

The following chapters of this dissertation are organized as follows:

Chapter 1 discusses the literature on computational homogenization. This chapter elaborates on FFT-accelerated homogenization schemes and presents two recent FFT-accelerated homogenization schemes developed by the μ Spectre team in detail.

Chapter 2 reviews the literature on ASR expansion and cracking mechanisms. The existing models for concrete deterioration due to ASR are described and categorized.

Chapter 3 introduces two ringing mitigation schemes based on two different local homogenization schemes at the interphases of the solution domain. With the examples

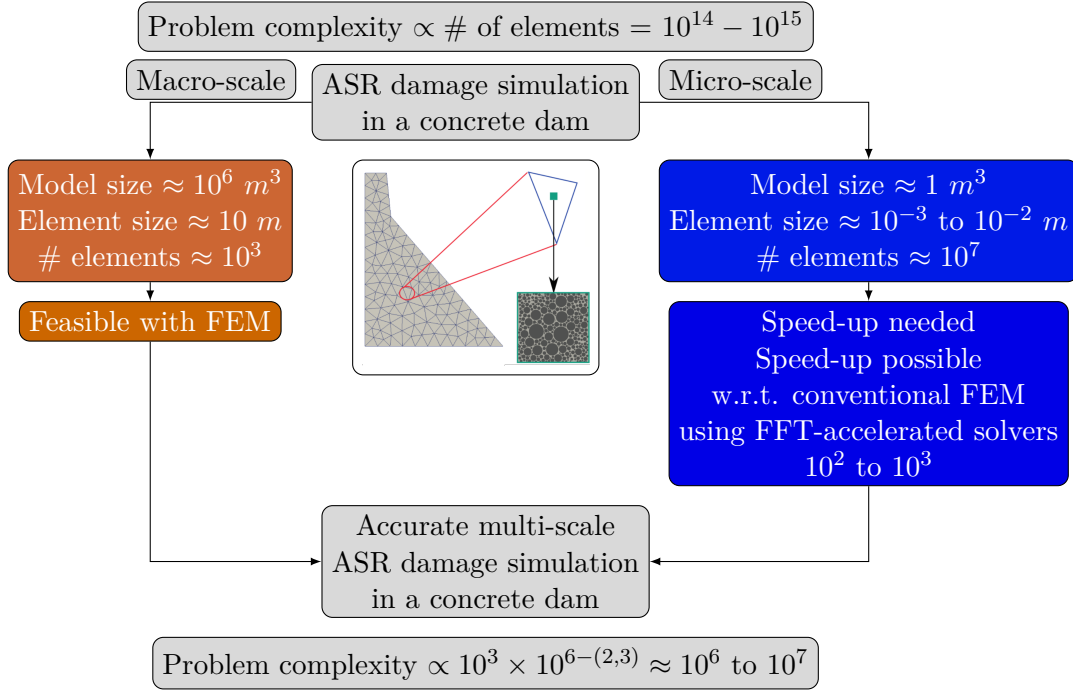


Figure 1: schematic of the multi-scale model of ASR damage

presented in this chapter, the effectiveness of proposed methods is evaluated.

In Chapter 4, the equivalence of two ringing-free FFT-accelerated homogenization schemes developed by μ Spectre development team, namely the generalized projection based solver with finite element (FE) discretization scheme (strain-based scheme developed by Leute et al. (2021)) and the preconditioned FFT-accelerated FEM scheme (displacement-base scheme developed by Ladecký et al. (2022b)) is shown. I am a co-author of both of these papers. Their equivalence is first expressed both in their mathematical formulation. Afterwards, their equivalence is also empirically shown through the comparison of their solution to a nonlinear homogenization problem. The strain-based scheme is used in Chapter 7 to simulate ASR damage.

Chapter 5 introduces a modified trust region solver that uses a first order approximation for the energy functional. This solver, as a non-convex solver that does not require explicit energy functional, enables us to benefit from the speed-up of FFT-accelerated homogenization schemes for non-convex problems. This solver is used in Chapter 7 to solve non-convex ASR damage problem.

Chapter 6 describes an algorithmic consistent tangent I introduced for the strain-based solution scheme. The introduced algorithmic consistent tangent merely involves solution of the linearized RVE problem at equilibrium. I have used potential energy minimization to derive the tangent. The developed effective tangent evaluation algorithm is exact within the limits (tolerance) of the solver used to solve the corresponding linear system of equations. The accuracy of the developed and implemented algorithmic consistent tangent is validated against analytical solutions. In addition, the accuracy and the speed-up of the algorithmic consistent tangent is compared to finite difference (FD) tangent approximation in presented examples in the chapter. The algorithmic consistent tangent is used in Chapter 7 for evaluating the reduction of the tangent due to ASR damage.

In Chapter 7, the machinery prepared in the previous chapters (chapters 3-6) is employed to model ASR damage in a regular periodic RVE. A compression-tension asymmetric damage material devoid of singularity issue in its tangent evaluation is also presented in this chapter and used as the constitutive law of the aggregate and the cement paste composing the RVE. The obtained results are tested against the literature and the influence of the external load (mean stress in uni-axial compression) is studied. The effect of using different regular FE discretization is also studied in this chapter.

The thesis is concluded, in Chapter 8, by the summary of the main results and an outlook on the possible further developments.

1 State of the art computational homogenization

Mechanical homogenization, motivated by the idea of representing a heterogeneous micro-structure as an equivalent homogeneous medium, aims to calculate effective mechanical properties of micro-structures, including homogenized elastic constants and the stress-strain response given the micro-structure and constitutive laws of the individual components. For simple micro-structures (e.g. micro-structures containing only linear elastic phases and simple geometries) the effective properties of a heterogeneous material can be estimated analytically (Budiansky (1965); Mori and Tanaka (1973); Norris (1985); Hill (1985); Milton and Sawicki (2003); Milton (1995); Nemat-Nasser and Hori (2013)). However, when the micro-structure gets more complex, analytical methods are generally no longer suitable for the determination of the effective properties.

Computational homogenization, on the other hand, is an effective method in up-scaling the behavior of complex micro-structures especially those consisting of, i. highly nonlinear, or ii. evolving phases (Hill (1963); Geers et al. (2010)). Computational homogenization methods are based on the construction of a micro-scale boundary value problem, the so-called cell problem, discretizing the solution domain and solving the governing equation, equilibrium equation for instance, using numerical schemes such as FEM (Schröder (2014)) or spectral methods (Moulinec and Suquet (1994); Eisenlohr et al. (2013)).

For solving the homogenization problem numerically, the spectral Fourier-basis solvers (Boyd (2000)) are efficient with a potential speed up compared to FEM solvers (Eisenlohr et al. (2013)). They are also appropriate for homogenization problems as the periodic

boundary condition is the most robust and realistic boundary condition among the possible RVE boundary conditions, namely, i. uniform displacement ii. uniform traction iii. periodic boundary conditions).

Following the seminal works of Moulinec and Suquet (1994, 1998), FFT based homogenization methods developed rapidly ; see, e.g. work of Schneider (2021); Lucarini et al. (2021). The spectral solvers can be efficiently used to solve partial differential equation (PDE)s corresponding to the quasi-dynamic mechanical equilibrium of microstructure. The availability of highly optimized FFT implementations (like *FFTW* Frigo and Johnson (2005) and *PFFT* Pippig (2013)) enabled the development of efficient spectral solvers that can beat standard FEM implementations significantly in terms of computational costs and computationally accessible system sizes. Increasing the resolution and improving solution accuracy is straightforward in spectral methods. As a result, large-scale micro-structures simulations are more efficient using spectral methods compared to conventional FEM.

In spite of their simplicity and efficiency for solving multiphase elastic problems, FFT methods suffer from mathematical artifacts in the form of spurious oscillations. These numerical artifacts appear in the homogenization solution as oscillatory overshoots specifically pronounced in the vicinity of abrupt phase transitions. Since the introduction of spectral solvers, several studies have tried to find the causes of the numerical artifacts in the solution of homogenization problem solved with spectral solvers and resolving them (see e.g. Müller (1996); Willot et al. (2014); Brisard and Dormieux (2012); Willot (2015); Schneider et al. (2016b); Kaßbohm et al. (2006); Khorrami et al. (2020); Ma et al. (2021)). Based on the findings in the literature, the following are the main causes of numerical artifacts persisting in the solution of the spectral solvers:

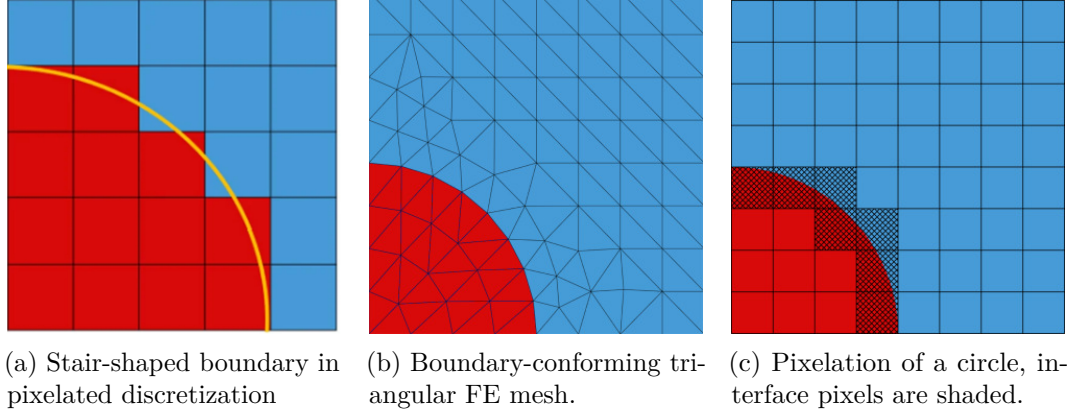


Figure 1.1: Comparison of a boundary-conforming and a regular voxel mesh obtained from Kabel et al. (2015)

1. In his work, Doitrand et al. (2015) proposed that voxel-shaped discretization is the cause of oscillations. In voxel meshes, in contrary to conventional FE discretization, non-smooth "zig-zag" interfaces between phases are inevitable (see Figure 1.1c), and modeling interfaces that are not aligned with the regular grid results in stair-shaped interface boundary (depicted in Figure 1.1c). This shortcoming results in artificial oscillatory behavior, specifically, in modeling curvilinear interfaces. The stair-cased shape transition contributes to spurious oscillations in the solution of spectral methods.
2. In accordance with Moulinec and Suquet (1998), Gibbs ringing might be caused by the fact that discrete Fourier transform (DFT) cannot satisfy Shannon's theorem for heterogeneous fields, in other words, DFT is not equal to Fourier Transform. To be consistent with Shannon's theorem, the cutoff frequency (i.e. the frequency above which the Fourier transform disappears) must be lower than half the sampling frequency. However, in mechanics, a heterogeneous field does not have a cut-off frequency.
3. Another possible origin of numerical artifacts in Fourier-accelerated method is reported to be the hourglass effect (Rüter (2019)), which is well known to cause numerical oscillations in FEM and has also been observed in spectral methods (Leuschner and Fritzen (2018)). The specific type of discretization employed in spectral methods (voxels) produces non-physical and oscillatory solutions due to the presence of

deformation modes that are not associated with energy changes. A typical example of such deformation for a rectangular 2-dimensional (2D) element with only one integration point in the center is depicted in Figure 1.2. The deformation depicted in Figure 1.2 yields a strain of zero at the integration point (noted as Q in Figure 1.2) and therefore corresponds to zero energy in the integration scheme of the element. This problem in a more general form corresponds to the incapability of voxel grided domain to express arbitrary compatible deformation field (χ in Figure 1.3a), i.e. only one strain or placement gradient tensor per voxel is insufficient to represent a general deformation and can merely present parallelograms. An example of a deformation making a parallelogram is depicted as ψ in Figure 1.3b.

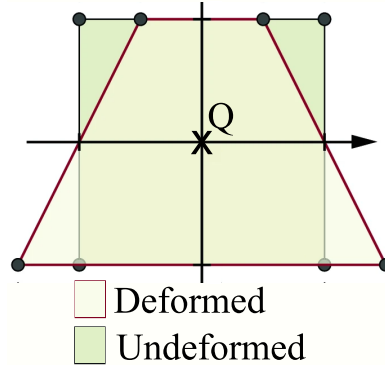


Figure 1.2: Hourglass mode in a single rectangular element with only one integration (quadrature point) at its center.

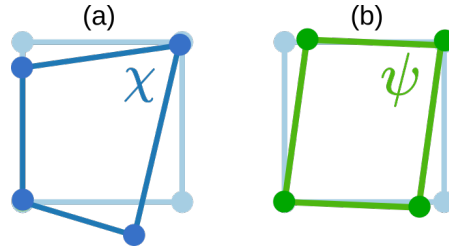


Figure 1.3: (a) arbitrary deformation vs (b) parallelogram deformation of a rectangular voxel. The undeformed voxel is shown in both subfigures in light blue while in subfigure (a) the dark blue shows arbitrary deformation noted with χ while the green shape in subfigure (b) shows the closest parallelogram deformed shape to the arbitrary deformation field that is obtainable in voxel grid discretization with one node per voxel (Figure is obtained from Leute et al. (2021)).

A sharp phase transition can cause oscillations in the solution field due to ringing artifacts, which are exacerbated by the increasing contrast between the touching phases. Damage

mechanics problems are the most susceptible to Gibbs ringing artifacts among all mechanical homogenization problems for the following reasons. Firstly, The most important phenomenon that drives damage mechanics is localization, i.e. local overestimation of the solution field causes non-physical damage initiation or growth, which makes the solution path of the system non-physical. Solving a damage mechanics problems by the original spectral method yields checker-board damage pattern (as shown in Figure 1.4a) which is obviously non-physical.

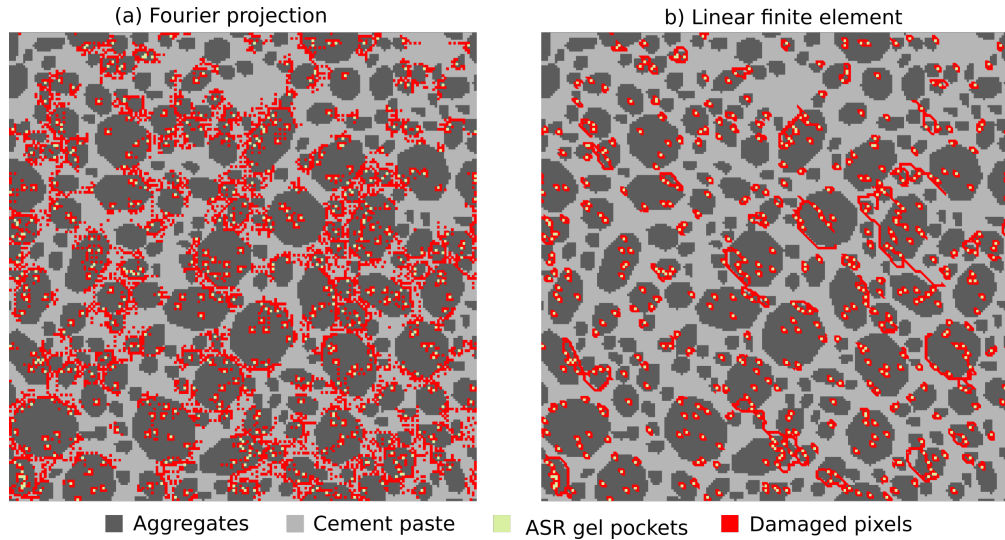


Figure 1.4: Crack pattern in a concrete micro-structure using a.spectral method susceptible to ringing artifacts, b.ringing-free solver using a finite element discretization (Figure is obtained from Leute et al. (2021)).

In addition, the high phase contrast between the damaged and intact phases (ratio of infinity in practice) also makes the solution particularly prone to high ringing artifacts. Therefore, for carrying out a physical solution for homogenization of damage mechanics and specifically ASR damage modeling, it is essential to address the ringing artifact.

Different strategies have been adopted, in the literature, to address the ringing artifact in spectral methods. Generally, the approaches can be categorized into the following groups.

1. Smoothing the phase interfaces: remedies in this category try to smooth the interface of the underlying phases of the solution domain Doitrand et al. (2015); Kabel et al. (2015); Charière et al. (2020); Ma et al. (2019) by introducing the

composite voxels as an example. We derive, implement, and test two sub-pixel homogenization approaches in Chapter 3. These methods can merely mitigate the artifacts in the solution.

2. Employing standard finite difference derivatives: These methods focus on the basis function used in the spectral method which implicitly is the Fourier basis in the original spectral scheme introduced by Moulinec and Suquet (1994). Some of the studies in the literature employed finite difference discrete derivatives. For instance, Müller (1996) utilized finite difference discretization, whereas Willot (2015) and Schneider et al. (2016b) describe a central-difference scheme on a staggered grid. In the literature, there are also other FFT-accelerated solution schemes using finite differences (Lebensohn and Needleman (2016); Vidyasagar et al. (2017)). These methods also can mitigate the ringing artifacts.
3. Altering the discretization: These methods focus on altering the discretization (regular voxel grid) as well as the basis function conventionally employed in spectral methods. Schneider et al. (2016a) also used linear hexahedral discretization in their FFT-accelerated solution scheme and Leuschner and Fritzen (2018) have developed an accelerated solution scheme based on Galerkin discretization with a FE basis. Recently, Leute et al. (2021) have developed a ringing free version of the projection-based spectral scheme using FE discretization and basis function and Ladecký et al. (2022b) have developed a FFT-accelerated preconditioned FEM scheme that is mathematically equivalent to the scheme of Leute et al. (2021). These methods can completely eliminate the ringing artifacts from the solution of the spectral methods. As shown in Figure 1.4b, such schemes are proper to model problems with localized phenomena such as damage mechanics.

In the rest of this chapter, after defining the nonlinear small-strain elasticity problem, I will elaborate on the projection-based spectral scheme using FE basis function that I co-developed with Leute et al. (2021), called, afterwards strain-based scheme since the degree of freedom (DoF) of the scheme is strain, and the FFT-accelerated preconditioned FEM scheme (Ladecký et al. (2022b)), called, from here on, displacement-based scheme since the DoF of the scheme is displacement, similar to previous work of Lucarini and Segurado

(2019b) where the authors also used displacement as the DoF of a FFT-accelerated solution scheme. I co-developed these two schemes with the μ Spectre development team and implemented them in μ Spectre Junge et al. (2022). They are used as the numerical solver in this dissertation.

1.1 Notation

We denote d -dimensional vectors and matrices by boldface letters: $\mathbf{a} = (a_\alpha)_{\alpha=1}^d \in \mathbb{R}^d$ or $\mathbf{A} = (A_{\alpha\beta})_{\alpha,\beta=1}^d \in \mathbb{R}^{d \times d}$. Matrix-matrix and matrix-vector multiplications are denoted as $\mathbf{C} = \mathbf{B}\mathbf{A}$ and $\mathbf{c} = \mathbf{B}\mathbf{a}$, which in the Einstein summation notation reads as $C_{\alpha\gamma} = B_{\alpha\beta}A_{\beta\gamma}$ and $c_\alpha = B_{\alpha\beta}a_\beta$ respectively. Greek letters (α, β, γ etc.) will be reserved for spatial indexes in range of 1 to d . The colon $:$ is the double dot product, a tensor contraction over two indices; therefore, $\mathbf{A} : \mathbf{B}$ can be noted in the index notation as $A_{\alpha\beta}B_{\beta\alpha}$.

Vectors and matrices arising from the discretization will be denoted by \mathbf{a} and \mathbf{A} , to highlight their special structure. These notations correspond to matrices and vectors defined on a d -dimensional grid and defined on all of the discretization points of the grid. The (I) -th component of \mathbf{a} will be denoted as $\mathbf{a}[I]$ and (I, J) -th component of \mathbf{A} will be denoted as $\mathbf{A}[I, J]$. We consider a general d -dimensional setting throughout the paper. However, for the sake of readability, I use $d = 2$ in the expanded form of matrices, such as in equation (1.2).

1.2 Nonlinear small-strain elasticity

A d -dimensional rectangular periodic cell $\Omega = \prod_{\alpha=1}^d \left[-\frac{l_\alpha}{2}, \frac{l_\alpha}{2}\right]$ is considered as the solution domain corresponding to the RVE schematically shown in 2D in Figure 1.5. The schemes explained in the following use the Mandel notation for the derivation as the symmetry of the small strain formulation elasticity allows. Doing so, we can reduce the dimension of the symmetric strain tensor from

$$\boldsymbol{\varepsilon} = \boldsymbol{\partial}\mathbf{u} : \Omega \rightarrow \mathbb{R}_{\text{sym}}^{d \times d} \quad (1.1)$$

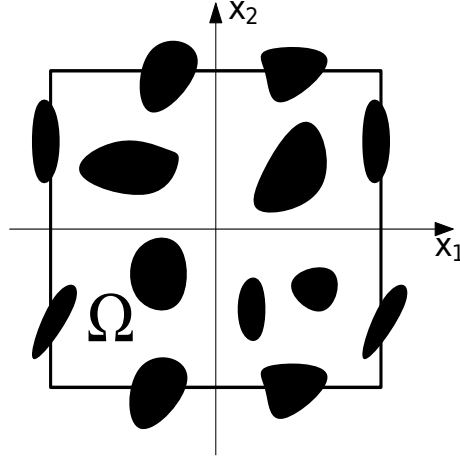


Figure 1.5: Rectangular two-dimensional cell with outlined periodic micro-structure obtained from Ladecký et al. (2021).

to $\boldsymbol{\partial}\mathbf{u} : \Omega \rightarrow \mathbb{R}^{d_m}$, where $d_m = \frac{(d)(d+1)}{2}$ and the symmetrized gradient operator $\boldsymbol{\partial}$ is in 2D defined as:

$$\boldsymbol{\partial}\mathbf{u} = \begin{pmatrix} (\nabla_s \mathbf{u})_{11} \\ (\nabla_s \mathbf{u})_{22} \\ \sqrt{2}(\nabla_s \mathbf{u})_{12} \end{pmatrix} = \begin{pmatrix} \frac{\partial}{\partial x_1} & 0 \\ 0 & \frac{\partial}{\partial x_2} \\ \frac{\sqrt{2}}{2} \frac{\partial}{\partial x_2} & \frac{\sqrt{2}}{2} \frac{\partial}{\partial x_1} \end{pmatrix} \begin{pmatrix} u_1 \\ u_2 \end{pmatrix}. \quad (1.2)$$

Accordingly, the fourth rank $\mathbb{C} : \Omega \rightarrow \mathbb{R}^{d \times d \times d \times d}$ can be represented as $\mathbf{C} \rightarrow \mathbb{R}^{d_m \times d_m}$ defined in the 2D case as:

$$\mathbf{C} = \begin{pmatrix} \mathbb{C}_{1111} & \mathbb{C}_{1122} & \sqrt{2}\mathbb{C}_{1112} \\ \mathbb{C}_{2211} & \mathbb{C}_{2222} & \sqrt{2}\mathbb{C}_{2212} \\ \sqrt{2}\mathbb{C}_{1211} & \sqrt{2}\mathbb{C}_{1222} & 2\mathbb{C}_{1212} \end{pmatrix}. \quad (1.3)$$

We split the overall strain of the RVE, $\boldsymbol{\varepsilon}$, to its mean, \mathbf{E} , and periodic fluctuation $\tilde{\boldsymbol{\varepsilon}} = \boldsymbol{\partial}\tilde{\mathbf{u}}$ contributions,

$$\boldsymbol{\varepsilon}(\mathbf{x}) = \mathbf{E} + \boldsymbol{\partial}\tilde{\mathbf{u}}(\mathbf{x}) \quad \forall \mathbf{x} \in \Omega. \quad (1.4)$$

The placement field $\tilde{\mathbf{u}}$ belongs to the space of admissible functions $V \left\{ \tilde{\mathbf{v}} : \Omega\text{-periodic} \rightarrow \mathbb{R}^d \right\}$ and $\int_{\Omega} \tilde{\mathbf{v}} \, d\mathbf{x} = \mathbf{0}$. The mechanical equilibrium equation as the governing equation can be

1.3 Strain-based (projection-based FFT-accelerated) scheme

written in our notation as (Belytschko et al. (2014)):

$$\boldsymbol{\partial}^T \boldsymbol{\sigma}(\mathbf{x}, \mathbf{E} + \boldsymbol{\partial} \tilde{\mathbf{u}}(\mathbf{x}), \mathbf{h}(\mathbf{x})) = \mathbf{0} \quad \forall \mathbf{x} \in \Omega, \quad (1.5)$$

where \mathbf{h} represents the internal parameters of the materials and $\boldsymbol{\sigma}$ is the stress field and $\boldsymbol{\partial}^T$ denotes the divergence operator. Various phases of a micro-structure can be described by different material models in a finite- or small-strain formulation. As mentioned earlier we take small-strain as the formulation; however, it is straightforward to extend the derivation to finite-strain.

The equilibrium equation (1.5) can be reformulated in the weak form as:

$$\int_{\Omega} \tilde{v}(\mathbf{x})^T \left(\boldsymbol{\partial}^T \boldsymbol{\sigma}(\mathbf{x}, \mathbf{E} + \tilde{\boldsymbol{\varepsilon}}(\mathbf{x}), \mathbf{h}(\mathbf{x})) \right) d\mathbf{x} = 0 \quad \forall \tilde{v} \in V \quad (1.6)$$

where \tilde{v} is the test function.

1.3 Strain-based (projection-based FFT-accelerated) scheme

Homogenization schemes, mostly, combine equations (1.1) and (1.6), which yield a set of 2^{nd} order differential equations. In the case of small strain formulation, they become the well-known Navier-Lamé equations. By contrast, equilibrium solution with Fourier techniques, typically, treat equations (1.6) and (1.1) as two sets of first-order differential equations separately (e.g. Lahellec et al. (2003); Vondřejc et al. (2014); Zeman et al. (2017); de Geus et al. (2017)). In such methods, the strain tensor $\boldsymbol{\varepsilon}$ is the DoF of the solution (in small strain), i.e. the equations are solved to directly obtain $\boldsymbol{\varepsilon}$. Equation (1.1) can be regarded as a constraint that enforces compatibility of the strain tensor, i.e. being the symmetric gradient of the respective placement map.

As proposed in the Fourier-Galerkin (FG) scheme developed by Zeman et al. (2017); de Geus et al. (2017), the projection based solution solves equations (1.5) and (1.1) in the subspace of compatible second-order tensors such that the pair of first-order differential equations reduces to the single first-order differential Eq. (1.5). This is formulated mathematically by a projection operator \mathbb{G} that maps any second-order tensor onto its compatible part and thereby into the subspace of compatible tensors.

The compatibility projection operator can be mathematically formulated according to Helmholtz decomposition.

In the strain-based scheme, the equilibrium equation (1.6) using the divergence theorem can be reformulated as:

$$\int_{\Omega} \left(\check{\check{\zeta}}(\mathbf{x}) \right)^T \boldsymbol{\sigma}(\mathbf{x}, \mathbf{E} + \tilde{\boldsymbol{\varepsilon}}(\mathbf{x}), \mathbf{h}(\mathbf{x})) \, d\mathbf{x} = 0, \\ \forall \check{\check{\zeta}} \in \mathcal{E} = \{ \partial \tilde{\mathbf{u}}(\mathbf{x}), \tilde{\mathbf{u}}(\mathbf{x}) : \text{periodic} \} \quad (1.7)$$

with $\check{\check{\zeta}} = \partial \tilde{v}$. The space of the compatible strain fields is denoted as \mathcal{E} . Note that the boundary terms vanish due to periodicity of the domain. It is also notable that, in addition to $\check{\check{\zeta}}$, $\tilde{\boldsymbol{\varepsilon}}(\mathbf{x})$ also needs to belong to \mathcal{E} which is often overlooked in the derivations in the literature. This is because the employed iterative solvers update the solution with iterates that are in the compatible field. This automatically makes the $\tilde{\boldsymbol{\varepsilon}}(\mathbf{x})$ to be a compatible field (Vondřejc et al. (2014)). This makes explicit application of the compatibility operator on the resultant fluctuation strain field unnecessary.

The test function in the strain-based scheme, $\check{\check{\zeta}}$ in (1.7), should be in a compatible strain space while in the FEM formulation, the test function is a displacement field. Therefore, the test function of the strain-based scheme is not an arbitrary field (unlike FEM). On the other hand, proceeding with the Galerkin discretization necessitates having a fully arbitrary test function. As a result, in order to apply the Galerkin discretization on (1.7), it is necessary to impose compatibility on the test variable. Zeman et al. (2017) have introduced a compatibility projection operator \mathbb{G} based on the Fourier discretization to impose compatibility. The Operator \mathbb{G} maps any second-order tensor to its compatible (periodic gradient) contribution. Applying the projection operator on the test variable $\check{\check{\zeta}}(\mathbf{x})$ makes it possible to continue with the Galerkin discretization and solve directly for strain field.

1.3.1 Projection operator

The key element of the strain-based scheme is the projection operator \mathbb{G} which enforces compatibility on an arbitrary field $\tilde{\zeta}(\mathbf{x})$ as:

$$\begin{aligned}\check{\zeta}(\mathbf{x}) &= [\mathbb{G} \star \tilde{\zeta}](\mathbf{x}) \\ &= \int_{\Omega} \mathbb{G}(\mathbf{x} - \mathbf{y}) : \tilde{\zeta}(\mathbf{y}) \, d\mathbf{y} \quad \forall \mathbf{x} \in \Omega.\end{aligned}\tag{1.8}$$

Applying the projection yields the compatible contribution $\check{\zeta}(\mathbf{x})$ of the original field $\tilde{\zeta}(\mathbf{x})$. In (1.8), \star denotes the convolution operator. The convolution format of Eq. (1.8) makes its application in Fourier space convenient, since convolution in real space is equivalent to contraction in Fourier space. Accordingly, (1.8) can be rewritten as:

$$\check{\zeta}(\mathbf{x}) = \mathcal{F}^{-1} \{ \hat{\mathbb{G}}(\mathbf{k}) : \mathcal{F} \{ \tilde{\zeta}(\mathbf{k}) \} \} \tag{1.9}$$

where $\hat{\mathbb{G}}(\mathbf{k})$ is the compatibility operator in the Fourier space, and \mathbf{k} is the discrete frequency vector in the Fourier domain. Leute et al. (2021) derived a general expression for the operator $\hat{\mathbb{G}}$ which can be expressed as an explicit function of a second rank tensor $\hat{\mathbf{g}}$: $(\hat{\mathbb{G}} = \hat{\mathbb{G}}(\hat{\mathbf{g}}))$. Considering that the objective of the $\hat{\mathbb{G}}$ operator is projecting a field as close as possible to its compatible contribution, they derived the operator $\hat{\mathbf{g}}$ by minimizing the difference of the $\check{\zeta}$ and $\partial \tilde{v}$ as:

$$\hat{\mathbf{g}}_{\alpha\beta}(\mathbf{k}) = \hat{\mathcal{D}}_{\alpha}(\mathbf{k}) \left(\hat{\mathcal{D}}_{\theta}^*(\mathbf{k}) \hat{\mathcal{D}}_{\theta}(\mathbf{k}) \right)^{-1} \hat{\mathcal{D}}_{\beta}^*(\mathbf{k}) \tag{1.10}$$

in index notation, where $\hat{\mathcal{D}}$ is the derivative operator (∂) in Fourier space, and $*$ denotes the Hermitian transpose, the derivation will be worked out in :FEM. The form of the projection operator $\hat{\mathbb{G}}$ as a function of $\hat{\mathbf{g}}$ is different in small strain and finite strain formulations (further details can be found in Zeman et al. (2017); Leute et al. (2021)).

In the original projection based method developed by Zeman et al. (2017), $\hat{\mathcal{D}}$ was expressed based on the Fourier basis as $\hat{\mathcal{D}}(\mathbf{k}) = i\mathbf{k}$ which yields a second rank tensor of

$\hat{\mathbf{g}}$ of the form:

$$\hat{\mathbf{g}}_{\alpha\beta}(\mathbf{k}) = \begin{cases} \mathbf{0} & \text{if } \mathbf{k} = \mathbf{0}, \\ \frac{\mathbf{k}_\alpha \mathbf{k}_\beta}{k^2} & \forall \mathbf{k} \neq \mathbf{0}. \end{cases} \quad (1.11)$$

\mathbf{k} s are normalized discrete Fourier wave-vectors. Leute et al. (2021) showed that, based on the general form of the projection operator according to (1.10) it is possible to derive projection operators using gradient operator ($\hat{\mathcal{D}}$) obtained from different discretizations and basis sets of choice. For instance, Leute et al. (2021) worked out a projection operator based on a linear FE discretization and showed that using the basis functions of a FE discretization results in elimination of Gibbs ringing artifact. This makes use of FE discretization suitable for problems with localized phenomena such as damage mechanics which is the target problem in this dissertation.

Choosing different $\hat{\mathcal{D}}$ in a projection based spectral method is equivalent to choosing different element types and shape functions in the conventional FEM formulation. The operator $\hat{\mathcal{D}}$, in case of using FE discretization, is calculated using the derivative of the corresponding shape functions. Similar to a FE scheme, the strain, stress, and tangents are evaluated at the quadrature point of the FE discretization. In the following, the discretized equilibrium equation is derived following a FE discretization process.

The projection operator, corresponding to a regular discretization grid, is denoted as \mathbf{G} . The Fourier parts of the application of the projection operator is dropped from now on for sake of brevity and the action of the projection operator on a discretized field $\tilde{\boldsymbol{\zeta}}$ in the discretized format is, in the following, noted as:

$$\tilde{\boldsymbol{\zeta}} = \mathbf{G} \tilde{\boldsymbol{\zeta}}. \quad (1.12)$$

1.3.2 Discretization

The weak form (1.7) can be discretized using the Galerkin method with FE basis functions conforming to a regular space-filling discretization. Such a discretization can be generated by periodic repetition of a space-filling discretization stencil, examples of which in 2D

1.3 Strain-based (projection-based FFT-accelerated) scheme

are shown in Figure 1.6. Inspired by the standard FE discretization procedure, the weak form (1.7) can be written as:

$$\begin{aligned} & \int_{\Omega} (\check{\check{\zeta}}(\mathbf{x}))^T \boldsymbol{\sigma}(\mathbf{x}, \mathbf{E} + \check{\check{\varepsilon}}(\mathbf{x}), \mathbf{h}(\mathbf{x})) d\mathbf{x} \\ & \approx \sum_{Q=1}^{N_Q} (\check{\check{\zeta}}(\mathbf{x}^Q))^T \boldsymbol{\sigma}(\mathbf{x}^Q, \mathbf{E} + \check{\check{\varepsilon}}(\mathbf{x}^Q), \mathbf{h}(\mathbf{x}^Q)) w^Q, \end{aligned} \quad (1.13)$$

where N_Q is the number of the quadrature points \mathbf{x}^Q . Strain and stress fields are evaluated at quadrature points \mathbf{x}_q^Q , $Q \in \{1, 2, \dots, N_Q\}$. On the other hand, the displacement fields are evaluated at discretization (nodal) points. Every component \tilde{u}_α of the unknown vector $\tilde{\mathbf{u}}$ is approximated by a linear combination of interpolating finite element basis functions

$$\tilde{u}_\alpha(\mathbf{x}) \approx \tilde{u}_\alpha^N(\mathbf{x}) = \sum_{I=1}^{N_I} \tilde{u}_\alpha^I \phi_\alpha^I(\mathbf{x}) \quad \text{for all } \mathbf{x} \in \Omega, \quad (1.14)$$

the coefficients $\tilde{u}_\alpha^I = \tilde{u}_\alpha^N(\mathbf{x}^I)$ correspond to the values of \tilde{u}_α^N at the discretization points \mathbf{x}^I and ϕ^I are the FE interpolation basis functions.

As noted before, the compatibility of the $\check{\check{\varepsilon}}$, $\check{\check{\zeta}}$ is not primarily satisfied. By definition $\check{\check{\varepsilon}}$, $\check{\check{\zeta}}$ are formulated as:

$$\check{\check{\varepsilon}}_{\alpha\beta}^N(\mathbf{x}^Q) = \sum_{I=1}^{N_I} \tilde{u}_\alpha^N(\mathbf{x}^I) \frac{\partial \phi^I(\mathbf{x}^Q)}{\partial x_\beta}, \quad \text{and} \quad \check{\check{\zeta}}_{\alpha\beta}^N(\mathbf{x}^Q) = \sum_{I=1}^{N_I} \tilde{v}_\alpha^N(\mathbf{x}^I) \frac{\partial \phi^I(\mathbf{x}^Q)}{\partial x_\beta}. \quad (1.15)$$

The compatibility can be enforced using the discrete operator $\mathbf{G} \in \mathbb{R}^{d_m N_Q \times d_m N_Q}$ introduced in (1.12) and accordingly left hand of (1.13) can be rewritten as:

$$(\mathbf{G}\check{\check{\zeta}})^T \mathbf{W}\boldsymbol{\sigma}(\mathbf{E} + \mathbf{G}\check{\check{\varepsilon}}, \mathbf{h}) = 0 \quad \forall \quad \check{\check{\zeta}} \in \mathbb{R}^{d_m N_Q}, \quad (1.16)$$

where $\mathbf{W} \in \mathbb{R}^{d_m N_Q \times d_m N_Q}$ are quadrature weight matrices in 2D with form of:

$$\mathbf{W} = \begin{bmatrix} \mathbf{W}_m & \mathbf{0} & \mathbf{0} \\ \mathbf{0} & \mathbf{W}_m & \mathbf{0} \\ \mathbf{0} & \mathbf{0} & \mathbf{W}_m \end{bmatrix}, \quad (1.17)$$

consisting of d_m identical diagonal matrices $\mathbf{W}_m[Q, Q] = w^Q$. considering that the test field $\tilde{\zeta}$ is now arbitrary, the discretized equilibrium (1.16) casts to:

$$\mathbf{G}^T \mathbf{W} \boldsymbol{\sigma}(\mathbf{E} + \mathbf{G} \tilde{\boldsymbol{\varepsilon}}, \mathbf{h}) = 0, \quad (1.18)$$

Where the strain field is defined on quadrature points of the FEM discretization. It is notable that the action of \mathbf{G}^T operator is equivalent to the divergence operator.

1.3.3 Linearization

Using Newton's method to solve the nonlinear system of equilibrium equation (1.18) iteratively, the $(i + 1)^{th}$ update of the strain field $\boldsymbol{\varepsilon}_{(i+1)}$ in the iterative scheme can be calculated from the previous approximation of the strain field $\boldsymbol{\varepsilon}_{(i)}$ incremented by a strain increment (finite increment) $\delta \boldsymbol{\varepsilon}_{(i+1)}$,

$$\boldsymbol{\varepsilon}_{(i+1)} = \boldsymbol{\varepsilon}_{(i)} + \delta \boldsymbol{\varepsilon}_{(i+1)}. \quad (1.19)$$

starting from an initial strain approximation $\boldsymbol{\varepsilon}_0$, the strain increment at each step is given by solution of the linear system:

$$\mathbf{G}^T \mathbf{C}_{(i)}^{\mathbf{W}} \mathbf{G} \delta \tilde{\boldsymbol{\varepsilon}}_{(i+1)} = -\mathbf{G}^T \mathbf{W} \boldsymbol{\sigma}(\mathbf{E} + \mathbf{G} \tilde{\boldsymbol{\varepsilon}}_{(i)}, \mathbf{h}_{(i)}). \quad (1.20)$$

Here weighed constitutive tangent matrix $\mathbf{C}_{(i)}^{\mathbf{W}} = \mathbf{W} \mathbf{C}_{(i)}$ absorbs quadrature weights \mathbf{W} . Based on the findings of Zeman et al. (2010); Vondřejc et al. (2014) and according to the fact that using the \mathbf{G} ensures the compatibility of the solution steps (the solution steps belong to a compatible strain field \mathcal{E}), right projection in the left hand side of (1.20) can be dropped and the linearized version of the equilibrium equation casts to:

$$\mathbf{G}^T \mathbf{C}_{(i)}^{\mathbf{W}} \delta \tilde{\boldsymbol{\varepsilon}}^{(i+1)} = -\mathbf{G}^T \mathbf{W} \boldsymbol{\sigma}(\mathbf{E} + \mathbf{G} \tilde{\boldsymbol{\varepsilon}}_{(i)}, \mathbf{h}_{(i)}). \quad (1.21)$$

1.3 Strain-based (projection-based FFT-accelerated) scheme

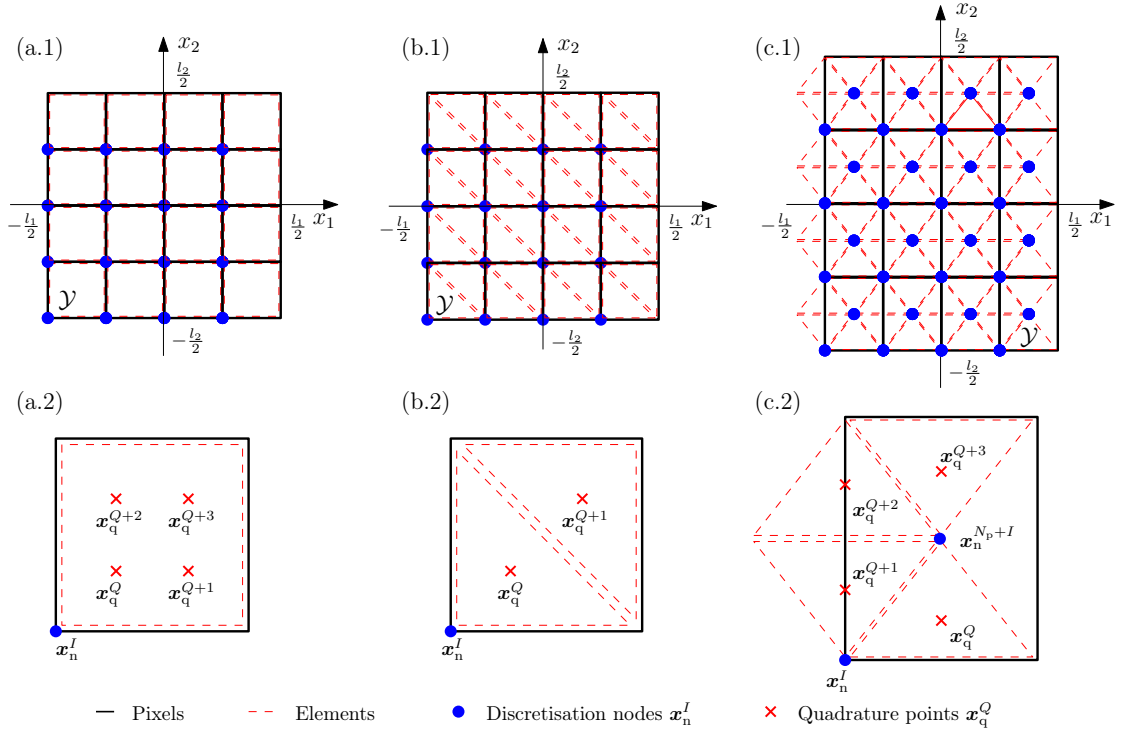


Figure 1.6: Example of regular periodic FE grids with associated discretization stencils for a two-dimensional cell Ω . All grids consist of 16 pixels ($N_p = 16$). Row (1) shows: (a.1) a grid with 16 discretization nodes ($N_I = 16$) and quadrature points ($N_Q = 64$), (b.1) a grid with 16 discretization nodes ($N_I = 16$) and 32 quadrature points ($N_Q = 32$), (c.1) a grid with 32 discretization nodes ($N_I = 32$) and 64 quadrature points ($N_Q = 64$). Row (2) shows: (a.2) a one-node stencil ($N_n = 1$) with one bilinear rectangular element and four quadrature points with quadrature weights $w^Q = \frac{1}{4}V_p$, (b.2) a one-node stencil ($N_n = 1$) with two linear triangular elements and two quadrature points with quadrature weights $w^Q = \frac{1}{2}V_p$, (c.2) a two-node stencil ($N_n = 2$) with four linear triangular elements and four quadrature points with quadrature weights $w^Q = \frac{1}{4}V_p$. Here, V_p denotes pixel volume, such that $V_p N_p = |\Omega|$. This figure is obtained from Ladecký et al. (2022b).

1.4 Displacement-based (preconditioned FFT-accelerated FEM) scheme

In this scheme, after applying the divergence theorem on the weak form noted in (1.6), instead of taking $\partial\tilde{v}$ as $\tilde{\zeta}$, the Galerkin discretization scheme is followed for the displacement test function of \tilde{v} similar to standard FEM framework which yields:

$$\int_{\Omega} \partial\tilde{v}(\mathbf{x})^T \boldsymbol{\sigma}(\mathbf{x}, \mathbf{E} + \partial\tilde{\mathbf{u}}(\mathbf{x}), \mathbf{h}(\mathbf{x})) \, d\mathbf{x} = 0 \quad \forall \tilde{v} \in V, \quad (1.22)$$

1.4.1 Discretization

The weak form (1.22) can be discretized following a process similar to what is explained in Subsection 1.3.2. Strain and stress fields are evaluated at quadrature points \mathbf{x}_q^Q , $Q \in \{1, 2, \dots, N_Q\}$, and the displacement fields are sampled at nodal points \mathbf{x}_n^I , $I \in \{1, 2, \dots, N_I\}$, cf. Figure 1.6. The count of nodal points is the product of the number of pixels N_p and the number of nodal points per pixel N_n . Here, we follow standard FE theory and approximate \tilde{v} and $\tilde{\mathbf{u}}$ by continuous element-wise polynomial of degree k and, therefore, their gradients are also expressable with polynomials with degree up to k . This enables us to proceed with discretizing the weak form equilibrium equation (1.22) with a suitable Gaussian quadrature rule:

$$\begin{aligned} & \int_{\Omega} \partial\tilde{v}(\mathbf{x})^T \boldsymbol{\sigma}(\mathbf{x}, \mathbf{E} + \partial\tilde{\mathbf{u}}(\mathbf{x}), \mathbf{h}(\mathbf{x})) \, d\mathbf{x} \\ & \approx \sum_{Q=1}^{N_Q} \partial\tilde{v}(\mathbf{x}_q^Q)^T \boldsymbol{\sigma}(\mathbf{x}_q^Q, \mathbf{E} + \partial\tilde{\mathbf{u}}(\mathbf{x}_q^Q), \mathbf{h}(\mathbf{x}_q^Q)) w^Q, \end{aligned} \quad (1.23)$$

where the choice of the quadrature rule determines the position of the quadrature points \mathbf{x}_q^Q and the quadrature weights w^Q . Components of $\tilde{\mathbf{u}}_{\alpha}$ are approximated with a linear combination of the basis functions ϕ^I (shape function corresponding to N_I) as:

$$\tilde{u}_{\alpha}(\mathbf{x}) \approx \tilde{u}_{\alpha}^N(\mathbf{x}) = \sum_{I=1}^{N_I} \tilde{u}_{\alpha}^N(\mathbf{x}_n^I) \phi^I(\mathbf{x}) \quad \forall \mathbf{x} \in \Omega, \quad (1.24)$$

1.4 Displacement-based (preconditioned FFT-accelerated FEM) scheme

where $\tilde{u}_\alpha^N(\mathbf{x}_n^I)$ are the nodal values for all \tilde{u}_α^N at nodal points \mathbf{x}_n^I . Taking partial derivative of (1.24) and evaluating at quadrature points yields:

$$\frac{\partial \tilde{u}_\alpha^N(\mathbf{x}_q^Q)}{\partial x_\beta} = \sum_{I=1}^{N_I} \tilde{u}_\alpha^N(\mathbf{x}_n^I) \frac{\partial \phi^I(\mathbf{x}_q^Q)}{\partial x_\beta} \quad \text{for } Q = 1, \dots, N_Q. \quad (1.25)$$

Using (1.25) one can evaluate the symmetrized gradients at quadrature points based on the nodal values. According to (1.25) one can define the partial derivative operator $\frac{\partial}{\partial x_\beta}$ in the matrix format as:

$$\mathbf{D}_\beta[Q, I] = \frac{\partial \phi^I(\mathbf{x}_q^Q)}{\partial x_\beta} \quad \text{for } Q = 1, \dots, N_Q \text{ and } I = 1, \dots, N_I. \quad (1.26)$$

Accordingly (1.25) can be written as:

$$\frac{\partial \tilde{u}_\alpha^N(\mathbf{x}_q^Q)}{\partial x_\beta} = \sum_{I=1}^{N_I} \tilde{u}_\alpha^N(\mathbf{x}_n^I) \mathbf{D}_\beta[Q, I] \quad \text{for } Q = 1, \dots, N_Q. \quad (1.27)$$

Substitution of (1.27) in (1.2) yields:

$$\partial \tilde{\mathbf{u}} = \mathbf{D} \tilde{\mathbf{u}} = \begin{bmatrix} \mathbf{D}_1 & \mathbf{0} \\ \mathbf{0} & \mathbf{D}_2 \\ \frac{\sqrt{2}}{2} \mathbf{D}_2 & \frac{\sqrt{2}}{2} \mathbf{D}_1 \end{bmatrix} \begin{bmatrix} \tilde{\mathbf{u}}_1 \\ \tilde{\mathbf{u}}_2 \end{bmatrix}, \quad (1.28)$$

as the approximation of the symmetrized gradient of displacement fluctuation (strain fluctuation) evaluated at quadrature points based on $\tilde{\mathbf{u}}_\alpha$ (the placement fluctuation evaluated at nodal points in the direction α). The matrices \mathbf{D}_1 are sparse due to the local support of the FE basis function and block circulant due to periodicity of the domain. Using regular FE discretization enables expressing the discretized gradient with the same gradient stencil for all of the pixels in the RVE. Therefore, the gradient of displacement field $\tilde{\mathbf{u}}$ can be obtained by a convolution of $\tilde{\mathbf{u}}$ with a short kernel, namely the gradient stencil.

According to (1.28), one can write the weak form (1.23) in a discretized format which

becomes:

$$\tilde{\mathbf{v}}^T \mathbf{D}^T \mathbf{W} \boldsymbol{\sigma}(\mathbf{E} + \mathbf{D} \tilde{\mathbf{u}}, \mathbf{h}) = 0 \quad \forall \tilde{\mathbf{v}} \in \mathbb{R}^{dN_I}, \quad (1.29)$$

with $\mathbf{W} \in \mathbb{R}^{d_m N_Q \times d_m N_Q}$, defined in (1.17). Since the test vector $\tilde{\mathbf{v}}$ is an arbitrary field, the discrete nonlinear equilibrium equation takes the form of:

$$\mathbf{D}^T \mathbf{W} \boldsymbol{\sigma}(\mathbf{e} + \mathbf{D} \tilde{\mathbf{u}}, \mathbf{h}) = \mathbf{0}. \quad (1.30)$$

1.4.2 Linearization

In order to solve (1.30) iteratively we use Newton's method to linearize it. Suppose the $(i+1)^{\text{th}}$ approximation of the nodal values $\tilde{\mathbf{u}}_{(i+1)} \in \mathbb{R}^{N_I}$ is given as the previous approximation $\tilde{\mathbf{u}}_{(i)} \in \mathbb{R}^{N_I}$ incremented by a finite displacement increment $\delta \tilde{\mathbf{u}}_{(i+1)} \in \mathbb{R}^{N_I}$:

$$\tilde{\mathbf{u}}_{(i+1)} = \tilde{\mathbf{u}}_{(i)} + \delta \tilde{\mathbf{u}}_{(i+1)}, \quad (1.31)$$

with an initial approximation $\tilde{\mathbf{u}}_{(0)} \in \mathbb{R}^{N_I}$. The displacement increment $\delta \tilde{\mathbf{u}}_{(i+1)}$ follows from the solution of the linear system

$$\underbrace{\mathbf{D}^T \mathbf{W} \mathbf{C}_{(i)} \mathbf{D}}_{\mathbf{K}_{(i)}} \delta \tilde{\mathbf{u}}_{(i+1)} = \underbrace{-\mathbf{D}^T \mathbf{W} \boldsymbol{\sigma}(\mathbf{E} + \mathbf{D} \tilde{\mathbf{u}}_{(i)}, \mathbf{h}_{(i)})}_{\mathbf{b}_{(i)}}, \quad (1.32)$$

where the discrete constitutive tangent matrix $\mathbf{C}_{(i)} = \frac{\partial \boldsymbol{\sigma}}{\partial \boldsymbol{\varepsilon}}(\mathbf{e} + \mathbf{D} \tilde{\mathbf{u}}_{(i)}, \mathbf{h}_{(i)}) \in \mathbb{R}^{d_m N_Q \times d_m N_Q}$,

$$\mathbf{C}_{(i)} = \begin{bmatrix} \mathbf{C}_{(i)11} & \mathbf{C}_{(i)12} & \mathbf{C}_{(i)13} \\ \mathbf{C}_{(i)21} & \mathbf{C}_{(i)22} & \mathbf{C}_{(i)23} \\ \mathbf{C}_{(i)31} & \mathbf{C}_{(i)32} & \mathbf{C}_{(i)33} \end{bmatrix}, \quad (1.33)$$

is obtained from the constitutive tangent $\mathbf{C}_{(i)}(\mathbf{x}) = \frac{\partial \boldsymbol{\sigma}}{\partial \boldsymbol{\varepsilon}}(\mathbf{x}, \mathbf{E} + \partial \tilde{\mathbf{u}}_{(i)}(\mathbf{x}), \mathbf{h}_{(i)}(\mathbf{x}))$, evaluated at quadrature points given the $\tilde{\mathbf{u}}_{(i)}$ the displacements at nodal points and the material internal variables $\mathbf{h}_{(i)}$. $\mathbf{K}_{(i)} \in \mathbb{R}^{dN_I \times dN_I}$ denotes the matrix of the linear system (1.32), and $\mathbf{b}_{(i)} \in \mathbb{R}^{dN_I}$ stands for its right-hand side. So far, we have worked out the

1.4 Displacement-based (preconditioned FFT-accelerated FEM) scheme

standard FE discretized equilibrium equation.

Equation (1.32) is the linearized FE equilibrium equation for a regular, space-filling, and periodic discretized RVE resulting in a symmetric system matrix $\mathbf{K}_{(i)}$ that is also positive definite for a wide range of homogenization problems. This makes the CG method the method of choice for solving (1.32), when combined with a proper preconditioner optimizing spectral characteristics of the system matrix. The preconditioner, presented in the following, is most conveniently applied in Fourier space according to its mathematical characteristics.

1.4.3 Preconditioning

The linearized equilibrium equation (1.32) is spectrally badly conditioned, i.e. the distribution of the eigenvalues of the system matrix do not make clusters and are distributed sparsely. The spectral characteristics of the system matrix are a crucial factor to the solution of linear systems with iterative solvers such as CG (Ganesh and Morgenstern (2020)). Undesired spectral properties (distribution of eigenvalues) of the linearized system makes use of iterative solver such as CG inefficient for solving equation (1.32) and also their solution complexity does not scale well with problem size (Bercovier and Rosenthal (1986)). The preconditioning is meant to improve the performance of iterative solvers solving a modified linear system of equation by clustering the distribution of its eigenvalues:

$$\mathbf{M}_{(i)}^{-1} \mathbf{K}_{(i)} \delta \tilde{\mathbf{u}}_{(i+1)} = \mathbf{M}_{(i)}^{-1} \mathbf{b}_{(i)}, \quad (1.34)$$

The preconditioned system of equation (1.34) should have more favorable spectral properties compared to (1.32) (Saad (2003); Golub and Van Loan (2013)).

In addition, another important characteristic of a proper preconditioner is having a computationally inexpensive inversion, since the inversion is basically an overhead to the solution process. It is notable that the matrix $\mathbf{M}_{(i)}^{-1} \mathbf{K}_{(i)}$ is not symmetric which makes CG inapplicable; however, given that both $\mathbf{M}_{(i)}^{-1}$ and $\mathbf{K}_{(i)}$ are symmetric, the system (1.34) solved with preconditioned conjugate gradient (PCG) becomes equivalent

to the symmetric form:

$$\mathbf{M}_{(i)}^{-1/2} \mathbf{K}_{(i)} \mathbf{M}_{(i)}^{-1/2} \delta \mathbf{z}_{(i+1)} = \mathbf{M}_{(i)}^{-1/2} \mathbf{b}_{(i)} \quad (1.35)$$

where, $\delta \mathbf{z}_{(i+1)} = \mathbf{M}_{(i)}^{1/2} \delta \tilde{\mathbf{u}}_{(i+1)}$, Therefore, (1.34) is solvable with PCG (Saad (2003)).

The preconditioner $\mathbf{M}_{(i)}$ proposed by Ladecký et al. (2021) has the format of the original system matrix of (1.32) though the material tangent stiffness in $\mathbf{K}_{(i)}$ is replaced by a spatially uniform material data (tangent) of a reference material ($\mathbf{C}^{\text{ref}} \in \mathbb{R}^{d_m \times d_m}$).

$$\mathbf{M}_{(i)} = \mathbf{K}_{(i)}^{\text{ref}} = \mathbf{D}^T \mathbf{W} \mathbf{C}_{(i)}^{\text{ref}} \mathbf{D} \in \mathbb{R}^{dN_I \times dN_I}. \quad (1.36)$$

Based on the results recently obtained by Gergelits et al. (2019); Pultarová and Ladecký (2021); Ladecký et al. (2021) that eigenvalues of the preconditioned system matrix $\mathbf{M}_{(i)}^{-1} \mathbf{K}_{(i)}$ reside in the following bounds independent of the system size:

$$\lambda_I^L = \min_{\mathbf{x}_q^Q \in \text{supp } \phi^I} \lambda_{\min} \left(\left(\mathbf{C}_{(i)}^{\text{ref}} \right)^{-1} \mathbf{C}_{(i)}(\mathbf{x}_q^Q) \right), \quad I = 1, \dots, N_I, \quad (1.37)$$

$$\lambda_I^U = \max_{\mathbf{x}_q^Q \in \text{supp } \phi^I} \lambda_{\max} \left(\left(\mathbf{C}_{(i)}^{\text{ref}} \right)^{-1} \mathbf{C}_{(i)}(\mathbf{x}_q^Q) \right), \quad I = 1, \dots, N_I, \quad (1.38)$$

where $\text{supp } \phi^I$ denotes the support of shape function ϕ^I , and $\lambda_{\min}, \lambda_{\max}$ are the minimal and maximal generalized eigenvalues, respectively. Based on (1.37) and (1.38), the conditioning number of the preconditioned system is independent of the discretization size (characteristic element length) and does not grow with mesh refinement. The preconditioner $\left(\mathbf{K}_{(i)}^{\text{ref}} \right)^{-1}$ clusters the eigenvalues of the system matrix and the number of the resulting clusters is independent of the discretization size of the solution domain. This is shown in Ladecký et al. (2022b) by showing that the number of required CG steps (representing the number of eigen value clusters) does not growing with mesh refinement. The proposed preconditioner is similar to the preconditioner proposed by Lucarini and Segurado (2019b).

1.4.4 Preconditioner inversion

Regular FE discretization yields spatially invariant \mathbf{D} since the stencil of all the pixels are identical. Therefore, for a spatially uniform $\mathbf{C}_{(i)}^{\text{ref}}$ the preconditioning matrix $\mathbf{K}_{(i)}^{\text{ref}} \in \mathbb{R}^{dN_n N_p \times dN_n N_p}$ consists of $(dN_n)^2$ block-circulant blocks of $\mathbf{K}_{(i)\bar{\alpha}\bar{\beta}}^{\text{ref}} \in \mathbb{R}^{N_p \times N_p}$:

$$\mathbf{K}_{(i)}^{\text{ref}} = \begin{bmatrix} \mathbf{K}_{(i)11}^{\text{ref}} & \mathbf{K}_{(i)12}^{\text{ref}} \\ \mathbf{K}_{(i)21}^{\text{ref}} & \mathbf{K}_{(i)22}^{\text{ref}} \end{bmatrix} \in \mathbb{R}^{2N_p \times 2N_p}, \quad (\text{for } dN_n = 2). \quad (1.39)$$

The block circulant structure of $\mathbf{K}_{(i)\bar{\alpha}\bar{\beta}}^{\text{ref}}$ makes its Fourier counterpart:

$$\hat{\mathbf{K}}_{(i)\bar{\alpha}\bar{\beta}}^{\text{ref}} = \mathbf{F} \mathbf{K}_{(i)\bar{\alpha}\bar{\beta}}^{\text{ref}} \mathbf{F}^H \quad (1.40)$$

The details are elaborated on by Ladecký et al. (2022b). The expanded version of the linearized equilibrium equation reads as:

$$\underbrace{(\mathbf{D}^T \mathbf{W} \mathbf{C}_{(i)}^{\text{ref}} \mathbf{D})^{-1}}_{(\mathbf{K}_{(i)}^{\text{ref}})^{-1}} \underbrace{\mathbf{D}^T \mathbf{W} \mathbf{C}_{(i)} \mathbf{D}}_{\mathbf{K}_{(i)}} \delta \tilde{\mathbf{u}}_{(i+1)} = - \underbrace{(\mathbf{D}^T \mathbf{W} \mathbf{C}_{(i)}^{\text{ref}} \mathbf{D})^{-1}}_{(\mathbf{K}_{(i)}^{\text{ref}})^{-1}} \underbrace{\mathbf{D}^T \mathbf{W} \sigma(\mathbf{e} + \mathbf{D} \tilde{\mathbf{u}}_{(i)}, \mathbf{h}_{(i)})}_{-\mathbf{b}_{(i)}}. \quad (1.41)$$

According to the findings of Ladecký et al. (2022b) the spectral characteristics of preconditioned FFT-accelerated scheme are as favorable as the projection-based FFT-accelerated scheme and given same discretization (e.g. identical FE discretization) the two methods are equivalent.

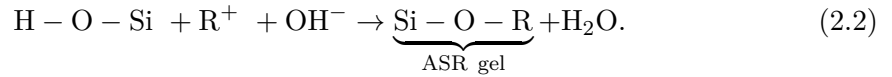
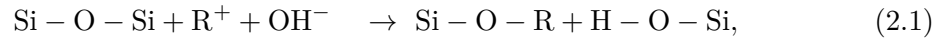
Optimal spectral characteristics of the system matrix in (1.21) and (1.41) makes linear iterative solvers and specifically CG solver ideal for solving the linearized equilibrium equation (1.21) (Pultarová and Ladecký (2021)). However, solving (1.21) with CG solver needs Hessian matrix \mathbf{C} to be symmetric positive semi definite (SPSD) which is not the case in several mechanical homogenization problems such as meta-materials (Li. (2017)) or continuum damage (Bažant (1976); Marvi-Mashhadi et al. (2020)). This issue is discussed and resolved in Chapter 5 by choosing a different iterative solver capable of handling non-convexity. After enabling the non-convex optimization in the strain-based scheme it will be used in Chapter 7 for modeling ASR damage.

2 State of the art ASR simulation

ASR is one of the most prevalent causes of concrete deterioration Hobbs (1988); Swamy (1991). ASR, reported for the first time by Stanton (1942), has caused deterioration to many concrete structures, such as dams and bridges (Sellier et al. (2017)). The ASR outcomes, on a structural level, include concrete expansion, loss of stiffness and strength, and even failure. This chapter discusses the state of the art of ASR modeling, after briefly introducing the ASR process.

2.1 ASR process

The ASR process begins with the formation of "gels" that are the result of chemical reactions between silica (SiO_2) in the aggregates and alkali in the pore solution (Fernandes et al. (2004); Ramyar et al. (2004); Peterson et al. (2006); Glasser and Kataoka (1981, 1982)),



Due to its hydrophilicity, the formed gel absorbs a significant amount of moisture, causing it to expand significantly (Pan et al. (2012)). Gel pockets are contained within the pores of the aggregates, and as they grow, they subject concrete structures to highly localized stress. The induced stress in concrete may cause microcracks inside aggregates (Ponce

and Batic (2006); Garcia-Diaz et al. (2006)), which grow and propagate as the alkali silica reaction advances. The coalescence of these cracks can cause stiffness loss and even failure at structural scale.

Concrete structures such as concrete dams are meant to last for decades or even centuries. Therefore, it is important to study ASR damage consequences on their structure that might appear in time scale of several years or decades. Various experiments have been conducted to determine how ASR affects concrete structures (Swamy and Al-Asali (1988); Marzouk and Langdon (2003)). Based on their findings, the ASR process and its effects on the mechanical properties of concrete may be influenced by a variety of factors including the mineralogy of the rock, the size of the aggregate, the alkali content, the relative humidity, temperature, and the confining stress, etc. Therefore, it is necessary to model the structures affected by ASR to evaluate the ASR influence on them and make a better understanding of the effects of different parameters.

ASR outcome depends on different mechanisms going on at various spatial scales from micro-scale where the ASR gels form (micro-scale) to the meso-scale where microcracks inside concrete aggregate coalesce and propagate into the cement paste, and, finally, macro-scale, where the structural outcome appears as macroscopic expansion, stiffness loss and structural failure. The multi-scale, multi-physics nature of the ASR damage process has always been an obstacle in developing a comprehensive predictive and practical model. To the author's best knowledge, previous investigations of the effects of micro-cracking on the structural scales have not been successfully scaled due to their prohibitively high computational costs (Cuba Ramos (2017)). In other words, explicit modeling of the underlying phenomena at the micro-structure using conventional methods yield computationally unacceptable problem sizes. On the other hand, it is vital for a predictive engineering model to resolve and probe the ongoing phenomena with sufficient resolution and capture the structural behavior at the same time. This means that the ASR process needs to be studied in a multi-scale scheme.

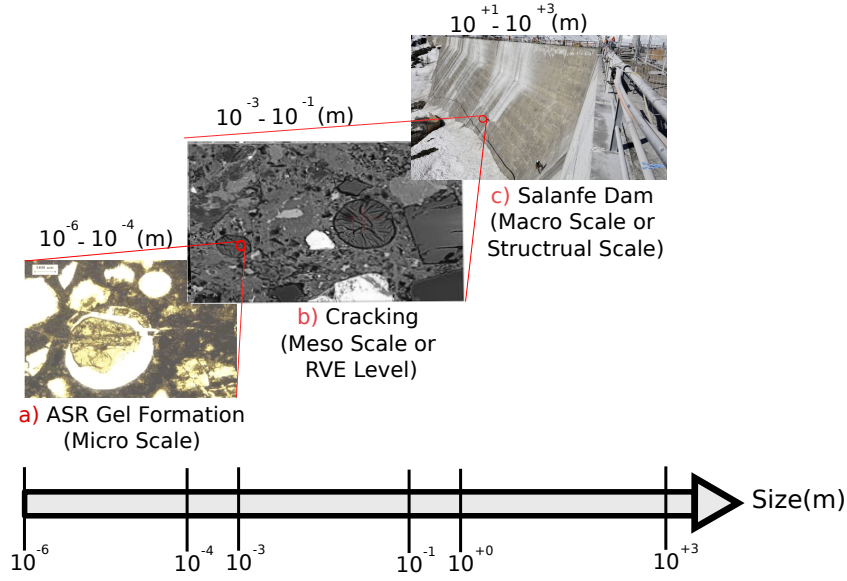


Figure 2.1: Different scales in modeling ASR (Figures adopted from Walker et al. (2006) and Papilloud (2019))

2.2 ASR simulation

There are two basic aspects involved in the the ASR damage process, namely chemical and mechanical aspects of ASR as depicted in Figure 2.2. Based on findings of Dunant (2009) and the review conducted by Pan et al. (2012), the interaction of the chemical and the mechanical aspect of ASR is unidirectional and the gel formation pace is independent of mechanical phase of the process. Accordingly, the chemical (left half of the process shown in Figure 2.2) and the mechanical aspect (right half of the process in Figure 2.2) of the ASR process are separable and can be studied independently of each other. As shown by Cuba Ramos (2017), the mechanical part of the process does not influence on its chemical part. Therefore, in a comprehensive ASR damage model we can detach these two phases and only focus on the mechanical part.

Explicit modeling of underlying phenomena in the concrete micro structure using conventional methods (such as conventional FEM) yields computationally prohibitive models. My research focuses on the mechanical aspect of the ASR damage process and more specifically on speeding up ASR modeling at the meso scale.

Modeling the mechanical aspects of ASR can be addressed at different spatial scales as

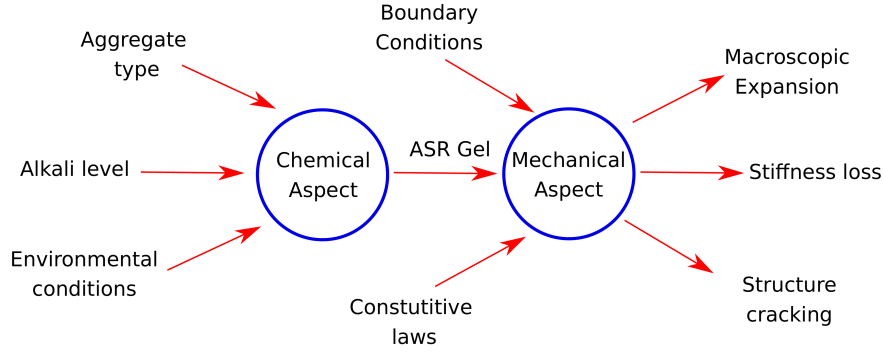


Figure 2.2: Separation of chemical and mechanical aspects of ASR

shown in Figure 2.1 and briefly described hereunder:

- **Micro scale:** The models at this scale are capable of capturing the smallest feature of ASR damage explicitly, i.e. the ASR gel pockets and their interaction with other phases (Zdenek et al. (2000); Schlangen and Çopuroglu (2007); Garcia-Diaz et al. (2006); Dunant and Scrivener (2010)). Accordingly, the resolution of micro scale models are in order of magnitude of $10^{-6} m$ (smallest scale shown in Figure 2.1a). This resolution allows to resolve crack initiation due to gel pocket expansion (Gallyamov et al. (2022)). The upper bound of the micro scale simulation setups is bounded by computational facilities. Models at this scale cannot currently involve multiple ASR product sites. The findings of micro scale models are valuable to study the influences of gel growth on localization and damage initiation mechanisms on ASR damage (Suwito et al. (2002)).
- **Meso scale:** The models at this scale should be big enough to be able to statistically represent concrete micro-structure with a random distribution of aggregate and cement paste phases; therefore, the size of the model setup should be in the order of the magnitude of $10^{-1} - 10^0 m$ where one can resolve concrete micro-structure, as shown in Figure 2.1b (Comby-Peyrot et al. (2009); Dunant and Scrivener (2012); Cuba Ramos (2017); Gallyamov et al. (2020)). Models at this spatial scale can be used RVEs for larger spatial scales. This is the scale that is mainly targeted to improve in my research.
- **Macro scale:** The models at this scale are used to predict the structural response of the structures experiencing ASR damage like the Salanfe dam shown in Figure 2.1c.

Most of existing models at this scale utilize phenomenological laws for modeling the ASR damage (Multon and Toutlemonde (2006)). The main characteristic of macro-scale ASR damage models is considering concrete as a homogeneous medium. One way of treating ASR expansion in these models is applying a local eigenstrain at the elements including the ASR product sites (Charlwood and Scrivener (2011); Charlwood et al. (1992)). The induced ASR expansion can also be taken a function of temperature, moisture and other environmental inputs to study the variation of ASR damage with respect to these parameters Léger et al. (1996).

Based on the findings of Cuba Ramos (2017), the load state imposed on the structure and the load scenarios do not influence the ASR expansion at the reactive ASR sites. Therefore, the phenomenon resolved in the micro-scale mechanical ASR damage modeling category (the first category presented above) can be separated from the other two categories dealing with larger spatial scales. Accordingly, in order to have a predictive ASR damage model in a structural scale, it is sufficient to resolve the problem discretized with the resolution of $10^{-3} - 10^{-2}$ m where the cement paste and the aggregates can be taken as explicit phases in the model. In other words, the resolution that is considered in the meso-scale models is necessary to model the ASR damage process accurately at the structural scale.

Accordingly, the required simulation setup sizes in a three dimensional setup results in $10^{12} - 10^{15}$ elements which is clearly beyond the computational power of the existing computational facilities and is computationally prohibitive. A possible solution is using a multi-scale model that breaks the problem into meso- and macro-scale models as depicted in Figure 1 in the introduction chapter. By adopting a multi-scale model, we can break the problem into a macro scale model with the element count in the order of 10^3 and a meso-scale model with element count of 10^7 (as depicted in Figure 1). The meso-scale part of the model is computationally expensive and the focus of this research is accelerating it in order to make comprehensive ASR modeling computationally affordable.

Cuba Ramos (2017) has developed one of the most promising multi scale models for simulating ASR damage. In their developed model, a FE^2 approach was adopted; however, it was not successful for simulating 3D ASR damage simulation and hampered by its high

computational costs. In FE^2 models, the underlying meso scale RVEs use FEM to solve the governing equations. FEM is designed to solve problems with complex geometries. The geometry of the RVEs (solution domain at meso-scale) are generally very simple and most of FEM machinery is actually wasted in solving such problems.

Cuba Ramos (2017) has adopted a continuum damage constitutive law, first introduced by Kachanov (1958), to model the ASR damage model at meso-scale. In this constitutive law, material is linear elastic before the damage threshold and switches to strain-softening after reaching a certain load state (Mazars (1984)). Strain softening is applied by a scalar damage variable D . The strain softening constitutive law, in their model, is isotropic and the Young modulus of the damaged material decays according to $E = E_0(1 - D)$ where E_0 is the intact Young modulus. The scalar damage variable D ranges between 0 for the virgin material to 1 for complete failure. The damage surface (f), proposed by Mazars and Pijaudier-Cabot (1989) has the form of:

$$f = \check{\epsilon} - \kappa(D) \quad (2.3)$$

where $\check{\epsilon}$ is a strain measure and κ is softening parameter which takes the largest value of the equivalent strain measure $\check{\epsilon}$ ever reached by the material. The most simple strain measure that results in the most simple strain-softening damage law is the norm of the strain tensor. One other possible strain measure appropriate for modeling concrete constitutive behavior used by Cuba Ramos (2017) has the form of:

$$\check{\epsilon} = \sum_i^d \mathcal{H}(\epsilon_i) \quad (2.4)$$

where, d is the number of the dimensions of the problems, ϵ_i is the i^{th} eigenvalue of the strain tensor, and \mathcal{H} is the Heaviside function. As a result of this strain measure, the material is only damaged in tensile conditions.

The strain softening part of the constitutive law introduces a non-convex potential energy which makes non-linear FEM solvers susceptible to instabilities (Pijaudier-Cabot and Bažant (1987)). Cuba Ramos (2017) adopted the sequential linear algorithm (SLA) (explained in details in Rots (2001); Rots and Invernizzi (2004); Rots et al. (2008);

DeJong et al. (2008)) to circumvent non-convexity of the problems. SLA is based on breaking the non-linear non-convex problem to a sequence of linear convex problems. In SLA, in each solution step, only one integration point is allowed to soften by certain reduction of its stiffness due to damage (Pari et al. (2022)). SLA is an event-driven algorithm and therefore it does not scale with problem size since by increasing problem size damage sites (possible event sites) increases rapidly; therefore, SLA becomes inefficient. This is a major drawback of a cell problem in the multi-scale model of Cuba Ramos (2017).

The combined complexity of meso- and macro-scale in the multi-scale model (as developed by Cuba Ramos (2017)) is proven to be prohibitively high and significant further speed up is necessary to have a comprehensive ASR damage modeling. In the multi-scale ASR model depicted in Figure 1, I have deliberately divided the problem in an unbalanced fashion (the meso-scale model is larger in sense of number of elements). This is because, in the meso-scale model, due to the regular geometry of the solution domain, one can use solution schemes faster than conventional FEM. In this research, I use FFT-accelerated solution schemes to speed up the solution in the meso scale model (at least 2 orders of magnitude). My modifications enabling effectively use of FFT-accelerated methods for ASR damage modeling are elaborated on in the following chapters of this thesis.

Spectral methods introduced first by Moulinec and Suquet (1994, 1998) can be significantly faster than FEM in solving periodic problems. Therefore, they look to be an efficient choice for modeling RVEs in a multi scale model. Replacing the numerical solver of the inner problem of FE^2 with a spectral method implementation results in drastic acceleration in simulations. In this research, a specific spectral method implementation introduced by Vondřejc et al. (2014) will be adopted, modified and extended to be able to model ASR damage at meso-scale.

3 Voigt and laminate homogenized pixels

As discussed in Chapter 1, numerical artifacts in the form of spurious ringing is one of the major issues of FFT-accelerated methods with Fourier basis in solving numerical homogenization of multi-phase elastic problems. It has been shown in the literature (Ma et al. (2021)) that the regular discretization of the interface causes staired interface of phases. This staired interphase is shown to be contributing to spurious oscillations near the phase change in FFT-accelerated schemes. Contrary to conventional FEM, spectral methods require a regular mesh (see Figure 1.1). As a result, general geometries cannot be discretized in spectral methods in a boundary-conforming manner. Thus, assigning material to the elements at the interface of different phases is challenging in spectral methods. In Figure 1.1, it is unclear what material property should be assigned to the shaded pixels in Figure 1.1.c that lie at the interface between two phases, while in conventional FEM, one can discretize the solution domain with an arbitrary interface profile using a boundary-conforming FE mesh. Such numerical artifacts are not of great importance in a wide range of problems; however, in problems with highly localized phenomena such as non-linear plasticity or continuum damage (targeted in this research), these artifacts are of high significance, since they can hugely affect the outcome of the simulation.

One of the approaches adopted in the literature for mitigating the ringing artifacts is to smooth the interphase (phases at the interface) by applying a homogenization scheme in pixels located at the interphase. In other words, a combination of materials involved in

a boundary pixel is considered for stress evaluation. As mentioned in Chapter 1, this approach is a ringing mitigation (and not an elimination) approach. In this chapter, I have examined the effectiveness of two strategies based on smoothing the sharp interfaces of the touching phases in suppressing the ringing artifacts.

I present two consistent methods for fabricating interface voxels with effective properties through the use of Voigt and laminate homogenization. These ideas are inspired by the work of Kabel et al. (2015); Lahellec et al. (2003); Brisard and Dormieux (2012). In both Voigt and laminate approaches, an effective interphase pixel is derived from a mixture of the underlying phases of the materials inside the pixel, i.e. the phase transition is smoothed by a local homogenization of tangent of the pixels at the interface. Therefore pixels consisting of more than one material in the full-scale resolution will be internally homogenized. Unlike most of the literature that is primarily focusing on extending the original spectral scheme proposed by Moulinec and Suquet (1994), I focus on the projection-based FFT-accelerated scheme as introduced by Zeman et al. (2017); de Geus et al. (2017) explained in Chapter 1.

3.1 Derivation

In this chapter, I present two homogenization schemes adopted at pixel level in the finite strain formulation. The derivation is identical for small strain in Voigt homogenization as it merely involves taking weighted average of the stress and tangent at the interface voxels. Here, I have conducted all the derivation in finite-strain formulation and the small strain derivation is straightforward. The implementation exists for both small- and finite-strain formulations in μ Spectre.

In the case of the laminate homogenization, the small strain derivation is simpler than finite-strain and rather straightforward, since, in small strain formulation, it is not necessary to consider the rotation of the interface inside a voxel due to deformation as the assumption of small strain does not allow such deformations. As a result, it is not necessary to consider different stress types, such as \mathbf{P} and \mathbf{S} (respectively first and second Piola-Kirchhoff stresses) while solving for RVE equilibrium and internal voxel equilibrium.

3.1.1 Voigt homogenization

This approach applies the simplest homogenization which is basically the weighted averaging of the stress and tangent of the underlying phases (Milton and Sawicki (2003)). The internal voxel homogenization merely involves weighted arithmetic averaging of the tangent of the constituent phases. This approximation gives the upper bound of the effective tangent of pixels. Given that the volume fraction of the phases L, and R in an interfacial pixel are respectively α and $(1 - \alpha)$, the effective stress and tangent of the pixel are:

$$\mathbf{P}^{\text{eff}} = \alpha \mathbf{P}^{\text{L}} + (1 - \alpha) \mathbf{P}^{\text{R}} \quad (3.1)$$

$$\mathbb{K}^{\text{eff}} = \alpha \mathbb{K}^{\text{L}} + (1 - \alpha) \mathbb{K}^{\text{R}}. \quad (3.2)$$

Where \mathbf{P} is the first Piola-Kirchhoff stress tensor, \mathbf{F} is placement gradient and \mathbb{K} is the finite strain tangent defined as: $\mathbb{K} = \partial \mathbf{P} / \partial \mathbf{F}$. First Piola-Kirchhoff stress \mathbf{P} and placement gradient \mathbf{F} are energy conjugate pairs that I have used for solving the equilibrium of the RVE in finite-strain formulation. As a result, after the evaluation of the material stress and tangent according to their constitutive law (possibly in different stress or strain measures), the mixing rules (3.1) and (3.2) are applied after their conversion to \mathbf{P} and \mathbb{K} . It is notable, that this conversion is also necessary for simple pixels since the equilibrium of the RVE is also expressed in terms of first Piola-Kirchhoff stress \mathbf{P} as $\nabla \cdot \mathbf{P} = \mathbf{0}$ and all the evaluated stresses in finite strain formulation needs to be converted to first Piola-Kirchhoff stress.

The Voigt homogenization scheme can be generalized to pixels consisting of more than two underlying phases by taking the effective stress and tangent of the pixel as the weighted average of those phases. In the Voigt homogenization, only the volume fraction of the different phases is important in calculating the effective tangent, while other aspects such as structure morphology are not influential at all.

3.1.2 Laminate homogenization

In the laminated pixel approach, the orientation of the interface of the underlying phases is also taken into account when calculating the effective stress and tangent. In this approach, the interface of the phases in a single voxel is approximated by a line in 2D and a plane in 3-dimensional (3D). We compute the orientation of the interface of the underlying phases by taking a weighted average of the normal vectors of the actual interface of the interface of the phases bounded inside the voxel. For instance, in the case of the interface of a polygon inclusion in 2D, the normal vector of the sides of the polygons bounded inside the pixel, with the lengths of the bounded sides as the weights is considered as the effective normal of the interface. In the case of polyhedron inclusion in 3D, the weighted sum of the faces of the polyhedron bounded in the voxel with the area of the faces as the weights is taken as the effective normal vector \mathbf{n} .

The general procedure of internal homogenization of the laminated pixels, as implemented, includes the following steps:

- Rotating the coordinate axis to align the X -axis with the normal of the laminate surface
- Solving the compatibility conditions for the stress and strain components contributing to the traction at the interface plane
- Calculating the effective stress and tangent from the resolved stress and tangent of the sub-phases of the pixel (Milton and Sawicki, 2003, Section 9.2).
- Rotating back the effective stress and tangent of the pixel to the main coordinate axis.

The procedure of approximating the inter-pixel interface with a laminate with a straight interface and the rotation to align the X' -axis with interface normal vector is schematically shown in the Figure 3.1. The general procedure, described above and elaborated on below, is applicable to materials with generally nonlinear constitutive laws. The rotation needed to align the normal vector of the laminate interface with the X -axis is applied by

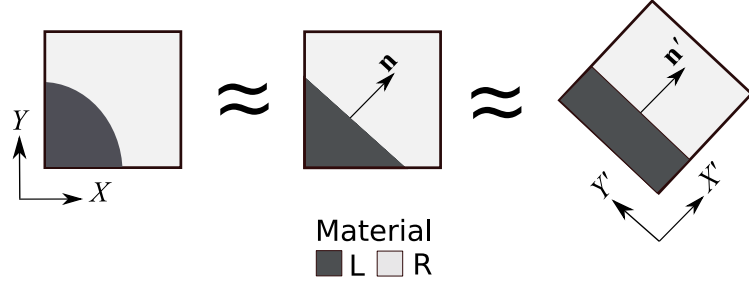


Figure 3.1: 2D schematic of the laminate homogenization approximation.

a rotation matrix with the form of:

$$\mathbf{R} = \mathbf{I} + \mathbf{V} + \mathbf{V}^2 \frac{1}{1+c} \quad (3.3)$$

where $c = \mathbf{n} \cdot \mathbf{e}_X$ is the cosine of the angle between the unit normal vector of the laminate interface (\mathbf{n}) plane and the unit vector in the \mathbf{e}_X direction. \mathbf{V} is the skew-symmetric cross product of \mathbf{n} and \mathbf{e}_X and is defined as:

$$\mathbf{V} = \begin{bmatrix} 0 & -v_3 & v_2 \\ v_3 & 0 & -v_1 \\ -v_2 & v_1 & 1 \end{bmatrix}, \quad (3.4)$$

with \mathbf{v} being the cross product of \mathbf{n} and \mathbf{e}_X ($\mathbf{v} = \mathbf{n} \times \mathbf{e}_X$). This rotation is schematically shown, in 2D, as the transformation of the middle shape to the right shape in the Figure 3.1.

In the rotated coordinate axis, the stress and strain elements can be easily categorized as intralaminar (in-plane, noted as \perp in the formula below) and interlaminar (across-plane, noted as \parallel in the formula below) components. The intralaminar components of a tensor \mathbf{T} with respect to a surface with normal vector \mathbf{n}' are:

$$\mathbf{T}^\perp = \mathbf{T} \cdot \mathbf{n}' \quad (3.5)$$

In case of the stress tensor, as a general rule, all the components contributing to the

traction force transmitted through the laminate interface are considered intralaminar \mathbf{P}^\perp and the remaining elements are interlaminar components \mathbf{P}^\parallel . In the rotated coordinate axis, where the laminate interface normal vector (\mathbf{N}') and X' -axis are aligned, the intralaminar and interlaminar components of a tensor \mathbf{T} are listed in Table 3.1. In the following, I explain the solution to the compatibility in the case of having two phases with arbitrary constitutive law inside a laminate pixel.

By imposing an average deformation \mathbf{F} to a pixel, I need to solve for the effective stress \mathbf{P}^{eff} and tangent \mathbb{K}^{eff} response of the equivalent laminate approximation of the voxel. To this end, we first solve for the deformation of the underlying materials L and R (respectively standing for left and right sub-pixel materials). \mathbf{F}^{R} and \mathbf{F}^{L} , In a general 3D case, are composed of 18 components (9 placement gradient \mathbf{F} components for each of the R and L phases) to be solved.

Table 3.1: Categorizing of a tensor \mathbf{T} into interlaminar and intralaminar stress/strain components with the interface of the phases normal being aligned to the X -axis

	intralaminar (\mathbf{T}^\perp)	interlaminar (\mathbf{T}^\parallel)
2D	$\mathbf{T}_{xx}, \mathbf{T}_{xy}$	$\mathbf{T}_{yy}, \mathbf{T}_{yx}$
3D	$\mathbf{T}_{xx}, \mathbf{T}_{xy}, \mathbf{T}_{xz},$	$\mathbf{T}_{yy}, \mathbf{T}_{zz}, \mathbf{T}_{yx}, \mathbf{T}_{zx}, \mathbf{T}_{yz}, \mathbf{T}_{zy}$

We divide stress tensors \mathbf{P}^{R} and \mathbf{P}^{L} and strain tensors \mathbf{F}^{R} and \mathbf{F}^{L} into interlaminar and intralaminar elements according to Table 3.1. For all of the interlaminar components (noted as \parallel), one can equate the deformation in both phases with that of the input strain ($\mathbf{F}^\parallel = \mathbf{F}^{\text{L}\parallel} = \mathbf{F}^{\text{R}\parallel}$). This yields 12 unknowns of 18 unknowns (6 \mathbf{F}^\parallel components of each of R and L phases), the interlaminar components of both L and R phases. The other 6 unknowns remained to be solved are the intralaminar components, $\mathbf{F}^{\text{R}\perp}$ and $\mathbf{F}^{\text{L}\perp}$. For solving them, we satisfy the internal pixel equilibrium at the interface of the laminate layers. Therefore we equate the traction \mathbf{t} at the interface of the underlying phases,

$$\mathbf{t}^{\text{L}} = \mathbf{t}^{\text{R}}. \quad (3.6)$$

In order to make sure the segregation of elements into interlaminar and intralaminar components remains valid, I express the vector of traction forces \mathbf{t} in the undeformed

configuration in terms of first Piola-Kirchhoff stress according to

$$\mathbf{t} = \mathbf{P} \cdot \mathbf{n}'. \quad (3.7)$$

Since the normal vector of the phases R and L at their interface, \mathbf{n}'^R and \mathbf{n}'^L , are collinear with opposing directions and according to (3.7), the equilibrium at the laminate interface expressed in terms of stress components has the form of:

$$\mathbf{P}^{L\perp}(F^L) = -\mathbf{P}^{R\perp}(F^R). \quad (3.8)$$

which is a system of equations composed of 3 nonlinear equations. The complementary equations for solving 6 remaining unknowns is based on that the weighted average of the intralaminar strain components of the underlying phases is equal to the intralaminar strain components of the imposed strain on the pixel.

$$\mathbf{F}^\perp = \alpha \mathbf{F}^{L\perp} + (1 - \alpha) \mathbf{F}^{R\perp}, \quad (3.9)$$

The 3 independent linear equations expressed in (3.9) can be easily solved for either of the phases. for instance, the intralaminar strain components of the phase R can be obtained as:

$$\mathbf{F}^{R\perp} = \frac{\mathbf{F}^\perp - \alpha \mathbf{F}^{L\perp}}{1 - \alpha}, \quad (3.10)$$

substituting (3.10) in (3.8) gives:

$$\mathbf{P}^{L\perp}(F^L) = -\mathbf{P}^{R\perp}\left(\frac{\mathbf{F}^\perp - \alpha \mathbf{F}^{L\perp}}{1 - \alpha}\right). \quad (3.11)$$

Which is now a set of 3 nonlinear equations with 3 unknowns $\mathbf{F}^{L\perp}$. By defining $\Delta P^\perp \equiv \mathbf{P}^{L\perp} + \mathbf{P}^{R\perp}$ the set of equations can be expressed as:

$$\Delta \mathbf{P}^\perp(\mathbf{F}^{L\perp}) = 0. \quad (3.12)$$

We have used iterative Newton-Raphson scheme for solving the set of nonlinear equations (3.12). Note that in case of small strain elasticity problem with linear elastic materials (3.12) becomes a linear system of equations. After solving for \mathbf{F}^\perp , I obtain

the intralaminar strain components of the other phase $\mathbf{F}^{\text{R}\perp}$ according to (3.10). Having the full \mathbf{F}^{R} and \mathbf{F}^{L} solved, I evaluate the stress and the tangent of the both phases L and R phases according to their constitutive laws. Now I have the stresses \mathbf{P}^{R} and \mathbf{P}^{L} and the tangents of both phases \mathbb{K}^{R} and \mathbb{K}^{L} . The mixture rule of the stresses are straightforward and can be generally taken as (3.1) similar to Voigt homogenization. However, for applying the mixture rule for the tangent I have taken the approach obtained from Milton and Sawicki (2003) and therefore I need to have the stress expressed as the second Piola-Kirchhoff stress \mathbf{S} that can be obtained for each sub-phase knowing the first Piola-Kirchhoff and the placement gradient according to:

$$\mathbf{S} = \mathbf{F}^{-1} \mathbf{P} \quad (3.13)$$

Using the second Piola-Kirchhoff stress allows for definition of symmetric tangent matrix $\mathbb{C} \equiv \partial \mathbf{S} / \partial \mathbf{E}$ where \mathbf{E} is the Cauchy strain tensor. the tangent \mathbb{C} can be obtained according to:

$$\mathbb{C} = [\mathbf{F} \otimes I]^{-1} [\mathbb{K} - [I \otimes \mathbf{S}]] [\mathbf{F} \otimes I]^{-T} \quad (3.14)$$

as derived by Curnier (1994). The operator \otimes denotes outer under product. $\mathbb{R} = \mathbf{A} \otimes \mathbf{B}$ can be expressed as $R_{\beta\gamma\lambda\theta} = A_{\beta\lambda} B_{\gamma\theta}$ in index notation. Having the symmetric tangents \mathbb{C}^{L} and \mathbb{C}^{R} I can proceed with the mixture rule derived in Milton and Sawicki (2003). The symmetric tangent \mathbb{C} correlates the strain and stress components. I already have categorized strain and stress components into interlaminar and intralaminar components. Following the same logic I divide the tangent \mathbb{C} into 4 blocks as expressed in Table 3.2.

Table 3.2: Blocks of the stiffness tangent based on the type of the components (interlaminar \parallel or intralaminar \perp) of the strain and stress tensors they correlate. Each row correspond to the components related to one category of the stress tensor and each column correspond to a category of the strain tensor.

	\mathbf{F}^{\parallel}	\mathbf{F}^{\perp}
\mathbf{P}^{\parallel}	$\mathbf{A}_{\parallel\parallel}$	$\mathbf{A}_{\parallel\perp}$
\mathbf{P}^{\perp}	$\mathbf{A}_{\perp\parallel}$	$\mathbf{A}_{\perp\perp}$

I construct these matrices (\mathbf{A} s) from components of the tangent matrix \mathbb{C} according to:

$$\mathbf{A}_{\perp\perp} = \begin{bmatrix} C_{1111} & \sqrt{2}C_{1113} & \sqrt{2}C_{1112} \\ \sqrt{2}C_{1113} & 2C_{1313} & 2C_{1312} \\ \sqrt{2}C_{1112} & 2C_{1312} & 2C_{1212} \end{bmatrix}, \quad (3.15)$$

$$\mathbf{A}_{\perp\parallel} = \begin{bmatrix} C_{1122} & \sqrt{2}C_{1133} & \sqrt{2}C_{1123} \\ \sqrt{2}C_{2213} & \sqrt{2}C_{3313} & 2C_{2313} \\ \sqrt{2}C_{2212} & \sqrt{2}C_{3312} & 2C_{2312} \end{bmatrix}, \quad (3.16)$$

$$\mathbf{A}_{\parallel\parallel} = \begin{bmatrix} C_{2222} & C_{2233} & \sqrt{2}C_{2223} \\ C_{2233} & C_{3333} & \sqrt{2}C_{3323} \\ \sqrt{2}C_{2223} & \sqrt{2}C_{3323} & 2C_{2323} \end{bmatrix}, \quad (3.17)$$

and $\mathbf{A}_{\parallel\perp} = \mathbf{A}_{\perp\parallel}$. Using these matrices we obtain the effective tangent blocks according to:

$$\mathbf{A}_{\perp\perp}^{\text{eff}} = \langle \mathbf{A}_{\perp\perp}^{-1} \rangle^{-1} \quad (3.18)$$

$$\mathbf{A}_{\perp\parallel}^{\text{eff}} = \langle \mathbf{A}_{\perp\perp}^{-1} \rangle^{-1} \langle \mathbf{A}_{\perp\perp}^{-1} \mathbf{A}_{\perp\parallel} \rangle \quad (3.19)$$

$$\mathbf{A}_{\parallel\parallel}^{\text{eff}} = \langle \mathbf{A}_{\parallel\parallel} - \mathbf{A}_{\parallel\perp} \mathbf{A}_{\perp\perp}^{-1} \mathbf{A}_{\perp\parallel} \rangle + \langle \mathbf{A}_{\parallel\perp} \mathbf{A}_{\perp\perp}^{-1} \rangle \langle \mathbf{A}_{\perp\perp}^{-1} \rangle^{-1} \langle \mathbf{A}_{\perp\perp}^{-1} \mathbf{A}_{\perp\parallel} \rangle \quad (3.20)$$

where $\langle \rangle$ denotes weighted arithmetic average. We obtain the effective symmetric tangent \mathbb{C}^{eff} by reconstructing it from \mathbf{A} blocks based on the blocks given in (3.18), (3.19), and (3.20). Then we compute the effective tangent \mathbb{K}^{eff} by applying the inversion of (3.14) as:

$$\mathbb{K}^{\text{eff}} = I \otimes \underline{\mathbf{S}}^{\text{eff}} + [\mathbf{F} \otimes I] \mathbb{C}^{\text{eff}} [I \otimes \mathbf{F}]^T. \quad (3.21)$$

The effective stress and the effective tangent of a laminate pixel can be obtained according to (3.1) and (3.21). Following the procedure explained above, I can compute the stress and effective tangent of the pixel under an imposed placement gradient \mathbf{F} and can take

that as the evaluated stress and stiffness of the pixel for the RVE homogenization.

The internal homogenization overhead of laminate pixels can cause massive impact on speed of solution of the whole RVE domain, because some pixels (interphase pixels) need internal homogenization that involves an iterative solution process (Newton’s method). In addition, by using laminate pixels we cannot anymore benefit from all the speed-up that we could achieve by optimizing the material evaluation (implementing the stress and tangent evaluation statically) because making laminate pixels hard-coded for material pairs results in combinatory growing laminate material count which is not feasible (combination of the underlying phases as template parameters).

Some possible solutions that might enable effective use of laminate homogenized pixels feasible are: the followings. *i* Hard coded laminate materials made from two predetermined materials defined as a new material. This needs definition of a new material whenever a new pair of materials need to be used as a laminate pixel. *ii* Another approach might be smart distribution of resources such as scheduling for stress and tangent evaluation. These approaches seem to be non-trivial to implement and are actually harmful for general performance. Having a scheduler for material stress and tangent evaluation at quadrature point as a general strategy is extremely harmful to performance when the evaluation expense of majority of material points is in the same range such as cases where laminate pixels do not exist.

3.2 Examples and results

Even though ringing artifacts are not unique to stair-shaped discretization, it is necessary to use a stair-shaped discretization to observe effectiveness of Voigt or laminate sub-pixel homogenization strategies suppressing ringing artifacts. Two examples using such discretization are presented here in order to demonstrate how much these approaches can mitigate ringing artifacts.

3.2.1 Inclined square inclusion example

In the first example, we take a 2D RVE containing an inclined rectangular inclusion located at the center of the RVE. The RVE experiences a spherical mean strain with amplitude of 1×10^{-4} . In addition, in each corner of the RVE, a triangular inclusion is inserted (depicted in Figure 3.2a). These triangular inclusions make the RVE geometrically equivalent to a RVE containing a straight square at its center. The problem is solved by using a spectral solver with Fourier-basis functions (as developed by de Geus et al. (2017)) with simple, split (Voigt homogenized), and laminate homogenized interphase pixels. The material assigned to the pixels at the interphase pixels (hatched pixels in 3.2b)

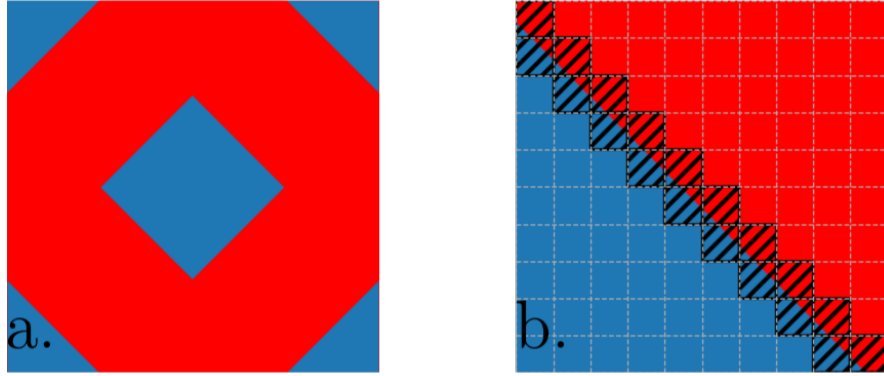


Figure 3.2: The phases in inclined square example, blue represents the inclusions and red represents matrix, a. Whole solution domain, b. zoomed over the boundary of a inclusion. Pixels located at the boundary of phases are hatched.

is determined by the location of the center of the voxel in the simple pixel approach. In Voigt homogenized pixels, however, the intersection of the boundary phase (modeled as a polygon in 2D) is intersected with the pixels edges and the contribution of each material at each pixel is determined by the surface ratio associated with each phase in that pixel. In the laminate pixel approach, in addition to the surface ratio, the normal vector of the intersection between the phase boundary and the pixel (the part of the interface bounded inside a pixel) is calculated and stored for each pixel.

This computational geometry process of intersecting two polygons in 2D and polyhedra in 3D is not straightforward. I have adopted and slightly modified an open source library named *Cork* (Bernstein (2007)) is to automate the task in μ Spectre. The RVE is subjected to a spherical mean strain with an amplitude of 1.0×10^{-4} . The domain is

discretized with 283 pixels in each direction. The Poisson ratio of both phases is 0.3 and their Young moduli are respectively $7.0 \times 10^1 \text{GPa}$ for the matrix and $7.0 \times 10^4 \text{GPa}$ for the inclusion that make a contrast of 10^3 between their Young moduli.

Figure 3.3 and Figure 3.4, respectively, illustrate the shear strain and the Von-Mises stress of the RVE at equilibrium. In each of these figures, the first row depicts the entire solution domain while the second row zooms in on the subdomain near the inclusion at the center of the RVE, where ringing artifacts are more evident. In both of the figures, the left column corresponds to the solution obtained using simple pixels, the middle column represents the response of the RVE obtained by split pixel approach, and the right column shows the response of the RVE obtained using laminate pixels.

Figure 3.3 and Figure 3.4 show that the Voigt homogenization approach can reduce the amplitude of the ringing artifact, but neither of them can eliminate it. In comparison to the solution of the simple cell, the highest shear strain value shown in Figure 3.3 and the highest von Mises stress in Figure 3.4 are lower in the split pixel solution. Additionally, the laminate pixel approach appeared to be more effective than Voigt homogenization in mitigating the ringing, and they can suppress the ringing in some areas of the solution domain; however, they are unable to completely eliminate the artifacts.

3.2.2 Circular square inclusion example

A circular inclusion is inserted at the center of the periodic RVE in the second example. This example generates stairs as well when discretized in a regular voxel grid. The geometry of the example is shown Figure 3.5a, the shaded pixels in Figure 3.5b correspond to the pixels residing on the boundary of the phases. In this example, both phases are taken as linear elastic materials with Poisson ratio of 0.3 and the Young moduli of inclusion and the matrix are respectively are 7.0 GPa for the matrix and 70.0 GPa which makes a hard inclusion problem with contrast ratio of 10.

The shear strain and the von Mises stress of the solution of the RVE under a spherical mean strain with amplitude of 1×10^{-3} are respectively shown in Figure 3.6 and Figure 3.7. The first row in each of these figures represents the solution for the entire RVE. The same

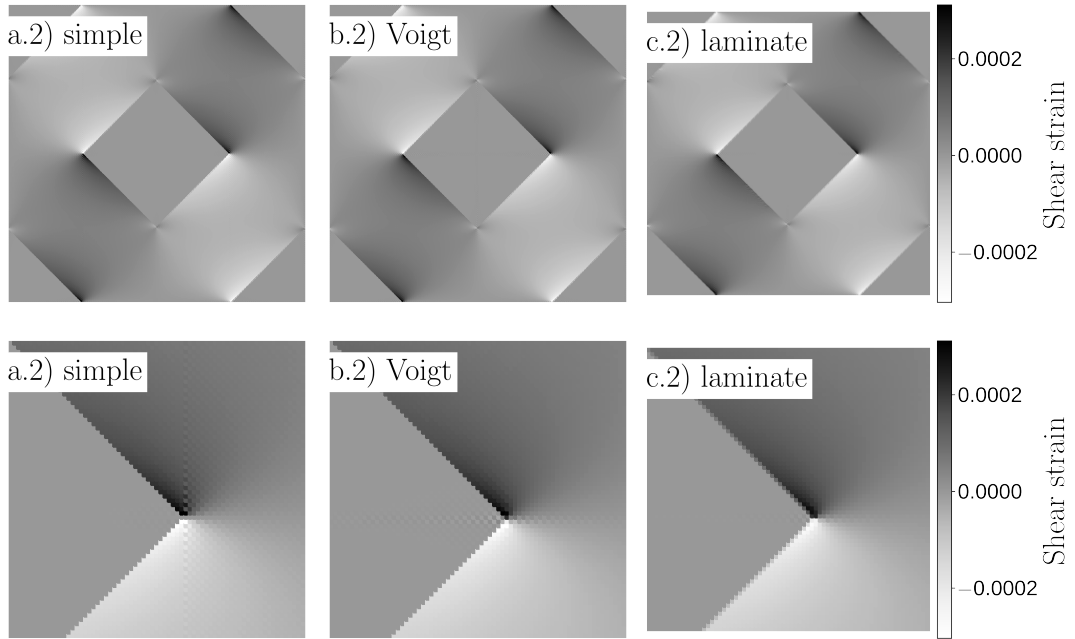


Figure 3.3: Shear strain inclined square example, a. Over whole solution domain, b. zoom over the right corner of the inclusion at the center of the RVE

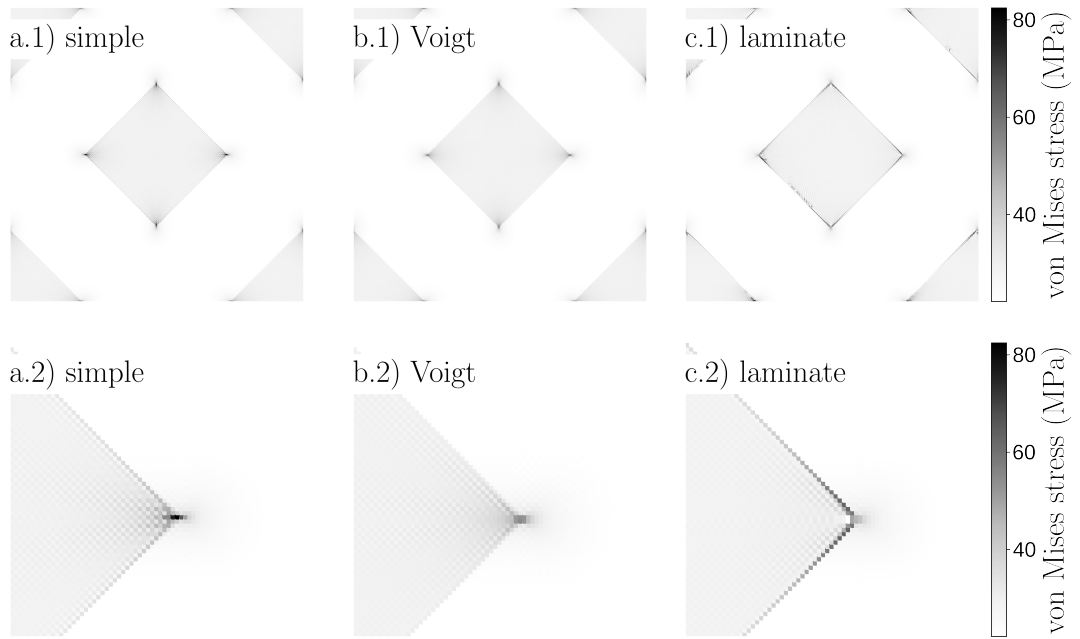


Figure 3.4: Von-Mises stress strain inclined square example, a. Over whole solution domain, b. zoom over the right corner of the inclusion at the center of the RVE

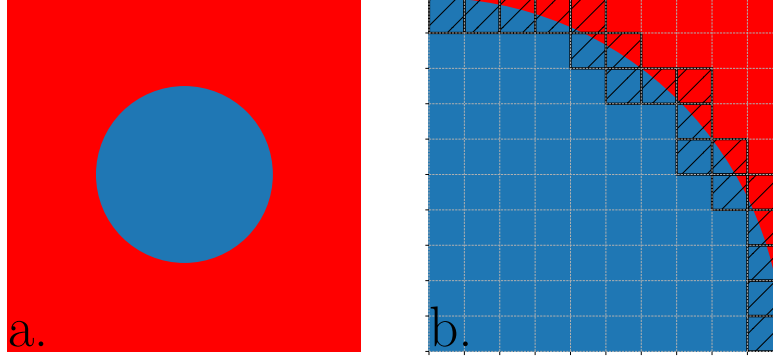


Figure 3.5: The phases in circular inclusion example, blue represents the inclusions and red represents matrix, a. Over whole solution domain, b. zoom over the boundary of a inclusion. Pixels located at the boundary of phases are hatched.

variable is shown zoomed over a region of the RVE including the phase boundaries (where the laminate and split pixels are located). The box at the top of the first row shows the area over which the zoom is placed in the second row of the same figure. In these figures, and specifically in the Von-Mises stress plots shown in Figure 3.7, it is evident that the Voigt pixel homogenization approach can suppress very high overshoots (pure black) stress values in the domain even though the ringing (checker-board) oscillations persist. It is also depicted that laminate sub-pixel homogenization approach is actually more effective than Voigt homogenization in mitigating ringing artifacts; however, it also cannot eliminate the ringing artifact.

3.2.3 Simple square example

Two previous examples are helpful to express the effectiveness of split and laminate pixel approaches visually and qualitatively. The third example is arranged to make a quantitative evaluation of the Voigt homogenization and laminate inter-pixel homogenization. In this example, a RVE containing a square inclusion occupying $\frac{5}{9}$ of RVE length in both directions is considered. The RVE is once discretized in a 9×9 structured grid and solved for equilibrium experiencing a spherical mean strain of 10^{-3} which will be used as a reference solution. Afterwards, the same RVE discretized in 3×3 grid is solved with both Voigt and laminate homogenized interphase pixels. The schematic of the RVE is

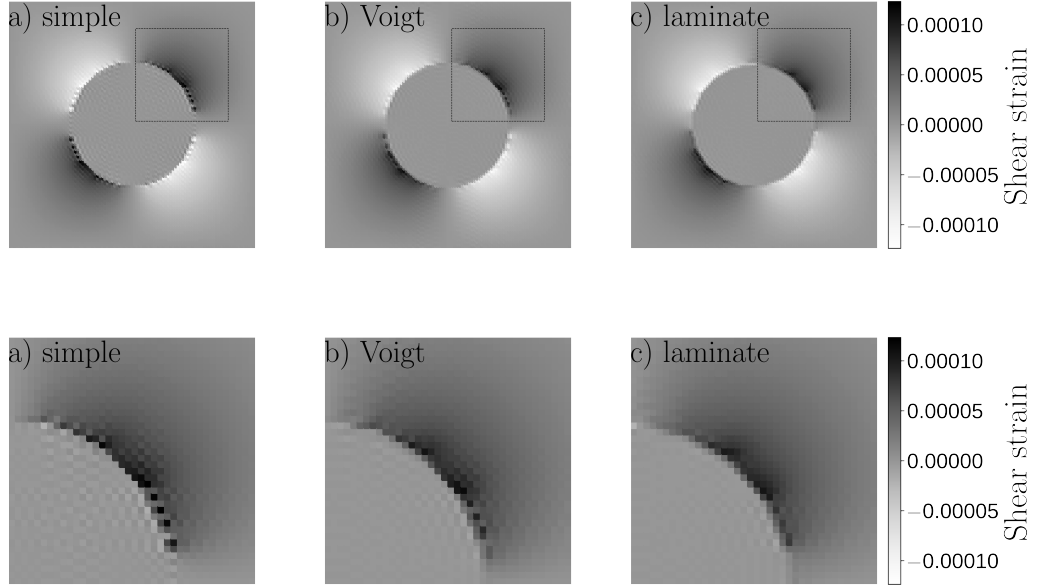


Figure 3.6: Shear strain strain of the circular inclusion example, a. Over whole solution domain, b. zoom over the region in the box depicted in the first row to show the oscillations at the boundary of the phases.

depicted in Figure 3.8a.

Both materials phases used in this test case are linear elastic materials. In the laminate homogenization scheme, the direction of the interface is taken as the weighted average of the normal vectors of the interfacial faces at each pixel. The direction of these normal vectors are shown as arrows in each interphase pixel in Figure 3.8a.

The test case is solved for interface pixels using either Voigt homogenization or laminate homogenization. The resultant elastic energy of the RVE solved with these two inter-pixel homogenization schemes is then compared with the reference value of the energy from the reference solution (6×6 cell solved with simple pixels). This comparison is repeated for different phase contrasts between the inclusion and the matrix phases of the RVE (shown respectively as white and gray in Figure 3.8a). Figure 3.8b illustrates the relative error of both approaches approximating the elastic potential energy of the RVE using laminate sub-pixel homogenization approach going under a spherical strain with amplitude of 10^{-4} for different phase contrast ratios. Figure 3.8b depicts that the range of the error in estimation of the strain energy of the RVE is roughly one order of magnitude less

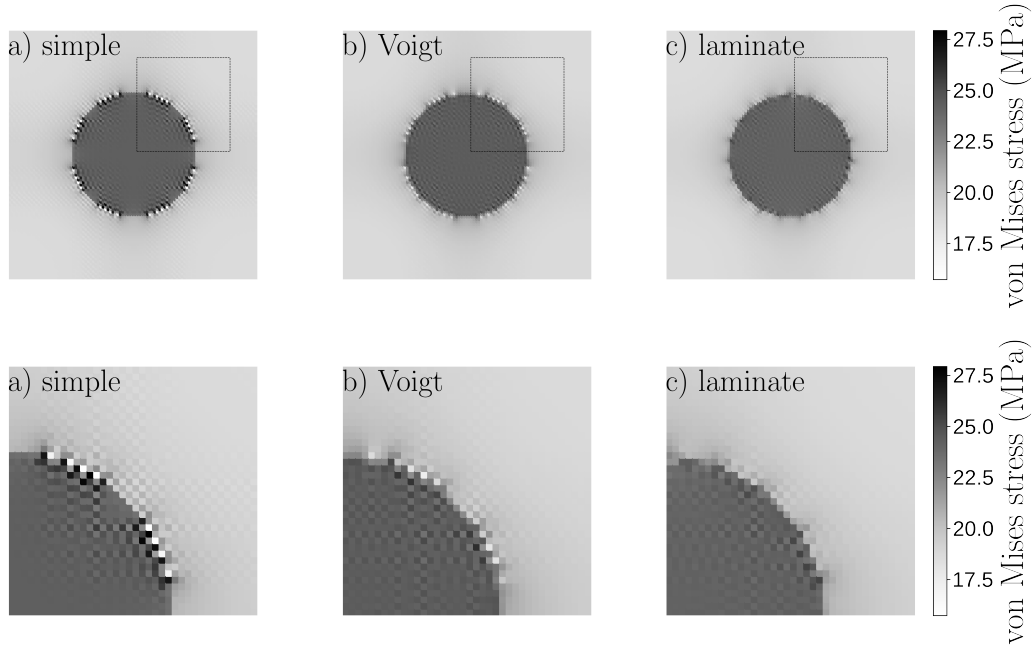


Figure 3.7: Von-Mises stress of the circular inclusion example, a. Over whole solution domain, b. zoom over the region in the box depicted in the first row to show the oscillations at the boundary of the phases.

compared to Voigt homogenization approach.

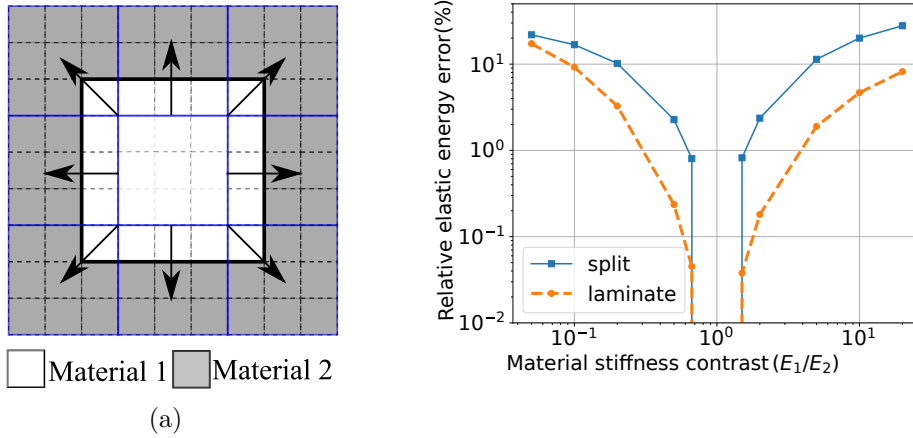


Figure 3.8: Test case for comparing the Voigt homogenization and the laminate homogenization, a. The configuration utilized for the test. b. The relative error of calculated elastic energy for different phase contrasts (E_1 and E_2 respectively correspond to the Young modulus of materials 1 and 2 shown in Figure 3.8a)

3.3 Conclusion

I have derived and implemented two different sub-pixel homogenization schemes in this chapter namely, Voigt and laminate homogenization schemes. Two possible approaches to reduce (mitigate) the Gibbs ringing artifacts in spectral methods have been presented. Unlike other similar implementations we have applied these two schemes in the projection-based FFT-accelerated solution scheme of de Geus et al. (2017). I have used the computational geometry means provided by *Cork* in order to automate generation of split and laminate pixels as well.

The first two examples of this section depict that although the Voigt and laminate pixel homogenization approaches can mitigate the ringing artifact to some extent, they cannot eliminate it. It seems that the ringing artifact persists even in low phase contrasts (10) between phases in the circular inclusion example. I intentionally picked examples in which the phase boundaries form a stair-shaped discretization, in which the Voigt and laminate homogenizations are the most effective. In the cases where stair-shaped boundaries do not exist, both approaches (laminate and Voigt inter-pixel homogenization schemes) are actually not sufficiently effective for making continuum damage mechanics solution devoid of non-physical checker-board crack patterns.

In addition, it should be noted that the laminate homogenization process can result in high computational costs due to its internal iterative homogenization, which severely reduces the appeal of using spectral solvers (solution speed-up) in the first place. In conclusion, these observations indicate that Voigt and Laminate homogenization approaches are not sufficient to simulate damage mechanics problems and that other methods are required to resolve the ringing artifact.

Even though both sub-pixel homogenization schemes presented here can mitigate the ringing artifact, they cannot eliminate long-range oscillatory fluctuation in the solution fields of the homogenization problem and therefore they do not enable us to use FFT-accelerated solvers for modeling damage at meso-scale. The Gibbs ringing elimination approaches based on altering the discretization are suitable to resolve the Gibbs ringing issue. Two examples of such methods are presented in Chapter 1 and will be elaborated

on in Chapter 4. Different groups including our development group (μ Spectre team) have altered the basis functions to eliminate the ringing artifacts in the FFT-accelerated scheme. For instance, the FFT-accelerated solution scheme developed by Leute et al. (2021) and already presented in Chapter 1 using FE discretization seems really promising and will be used in Chapter 7 for ASR damage modeling, where it is crucial to have a ringing free

4 Equivalence of the strain-based and displacement-based schemes

As stated in Chapter 1, FFT-accelerated spectral solvers, implicitly, use the Fourier polynomials as basis functions to express the variables in the solution domain. This choice of basis functions is closely linked to the Gibbs-ringing artifacts that are ubiquitous in almost all of Fourier accelerated solvers in the literature (Schneider (2021); Leute et al. (2021)). Based on our findings explained in Leute et al. (2021) (μ Spectre development team), opting for FE basis functions for defining the gradient operator, from which the projection operator is constructed, can eliminate the Gibbs-ringing artifact. The FEM shape function gradients introduced by Leute et al. (2021) allows simulating RVEs even with infinite phase contrast at the interfaces, for instance RVEs containing free surfaces or completely degraded materials due to damage. Resolving these two shortcomings of FFT-accelerated solvers (ringing artifacts and incapability of handling infinite phase contrast) makes it possible to tackle homogenization of problems with highly localizing phenomena such as strain softening. This also enables one to use the efficient and well scaling iterative linear solvers such as CG for homogenization of sophisticated problems such as damage mechanics.

Achieving fast, efficient, and ringing-free FFT-accelerated solver using FE basis functions raises the question whether a pure FEM scheme can realize similarly efficient scaling solution (as efficient as FFT-accelerated schemes). Earlier, Schneider et al. (2016a) used linear hexahedral discretization in their FFT accelerated solution scheme. They also noted that the scheme can be expressed in a displacement-based scheme where the

Chapter 4. Equivalence of the strain-based and displacement-based schemes

unknowns of the problem are actually the displacement of the nodes similar to FEM. Leuschner and Fritzen (2018) have worked out a displacement-based FFT-accelerated solution scheme using the FE Galerkin discretization and also showed that using a preconditioned CG with the discretized periodic Green's operator of a uniform reference material as the preconditioner improves the efficiency of the solution.

Ladecký et al. (2022b) (μ Spectre development team) have developed a pure FE solution scheme that solves the linearized system with a geometrically optimal preconditioner based on the discretized periodic Green's function of a reference material. Their displacement-based formulation successfully extended the concepts introduced by Leuschner and Fritzen (2018) to arbitrary regular FE discretizations. For specific choice of the reference material (4th rank symmetrizing identity tensor $\mathbf{I}_s = \frac{1}{2}(\delta_{ik}\delta_{jl} + \delta_{il}\delta_{jk})$), Their solution scheme is already shown to realize the same distribution of eigenvalues (of the corresponding linearized system of equations) as the strain-based method introduced by Leute et al. (2021). This equivalence is achieved naturally using the same discretization. We have also shown the equivalence mathematically by showing that the solutions steps of the two schemes generates same series of iterates (Ladecký et al. (2022b)). By using the same iteration termination criteria, we have also shown the equivalence of the strain-based and the displacement-based schemes numerically. Ladecký et al. (2022b) presented the scheme on a small-strain elasticity micro-mechanical formulation discretized on a regular periodic grid. The extension of the scheme to finite-strain is also straightforward.

In this chapter, I show the equivalence of the displacement-based preconditioned FEM scheme (Ladecký et al. (2022b)) and an extended form of the strain based scheme (Leute et al. (2021)). This equivalence is already shown by Ladecký et al. (2022b) for a specific case of reference material (4th rank symmetrizing identity tensor \mathbf{I}_s). The projection operator we introduced in Leute et al. (2021), implicitly, uses the 4th rank symmetrizing identity tensor \mathbf{I}_s as a reference material in the equivalent displacement-based formulation. Therefore, their introduced projection operator is from now on denoted as $\mathbf{G}_{\mathbf{I}_s}$ (Projection with the 4th rank symmetrizing identity tensor \mathbf{I}_s as the corresponding reference material in the subscript).

Ladecký et al. (2022b) has empirically shown that using a reference material capable of

expressing the anisotropy of the system response (including the Poisson effect) accelerates the solution, at least, by roughly 50% in a nonlinear problem (as also indicated later here in Table 4.1). As an extension to $\mathbf{G}_{\mathbf{I}_s}$, here, I incorporate a reference material defined by elastic tangent tensor \mathbf{C}^{ref} into the definition of the projection operator explained in Chapter 1 and introduce a modified projection operator with an arbitrary admissible reference material with elastic tensor \mathbf{C}^{ref} . The subscript of the projection operator ($\mathbf{G}_{\mathbf{C}^{\text{ref}}}$) denotes the reference material of the projection operator. For instance, the standard projection operator introduced by Leute et al. (2021) is denoted here as $\mathbf{G}_{\mathbf{I}_s}$ and the projection operator with a generic \mathbf{C}^{ref} as the reference material is noted as $\mathbf{G}_{\mathbf{C}^{\text{ref}}}$. I also will show empirically that using $\mathbf{G}_{\mathbf{C}^{\text{ref}}}$ with a \mathbf{C}^{ref} better reflecting the anisotropy of the RVE can also speed up the solution of the strain-based solution compared to using $\mathbf{G}_{\mathbf{I}_s}$.

I, in this chapter, will show that solving the equilibrium equation (1.18) using the introduced projection operator $\mathbf{G}_{\mathbf{C}^{\text{ref}}}$ is equivalent to using the displacement-based scheme with a preconditioner defined with the discretized periodic Green's operator of a reference material \mathbf{C}^{ref} as the reference material. The equivalence of these two approaches is first shown in their formulation where the solution iterates are shown to be equivalent in both schemes.

It is also notable that the DoF these solution schemes differ and to be able to compare them same termination criterion for the iterative solvers is needed. This needs modification in the definition of the solution error (which is by default the quadratic norm of the solution step in the state space of the DoF of the scheme). This is the reason of the difference of the default termination criterion of these two schemes non-conforming as their solution DoF differ. The required modification in the termination criterion is also introduced in this chapter and solvers with modified termination criteria are used for solving the example presented here.

The content of this chapter is partly taken from a submitted paper from $\mu\text{Spectre}$ development team (Ladecký et al. (2022b)) and another manuscript (Ladecký et al. (2022a)) that is under preparation and is almost ready.

4.1 Derivation

To show the equivalence of the strain-based and displacement-based approaches we start from the final form of the linearized equation system of the discretized equilibrium equation (1.41). For sake of simplicity, the FFTs are omitted from the formulation and the quadrature weights w^Q of the quadrature points are assumed to be uniform; therefore, the weight matrices can be dropped for now. The equilibrium equation (1.41) yields:

$$\underbrace{\left(\mathbf{D}^T \mathbf{C}_{(i)}^{\text{ref}} \mathbf{D}\right)^{-1}}_{(\mathbf{\kappa}_{(i)}^{\text{ref}})^{-1}} \underbrace{\mathbf{D}^T \mathbf{C}_{(i)} \mathbf{D}}_{\mathbf{\kappa}_{(i)}} \delta \tilde{\mathbf{u}}_{(i+1)} = - \underbrace{\left(\mathbf{D}^T \mathbf{C}_{(i)}^{\text{ref}} \mathbf{D}\right)^{-1}}_{(\mathbf{\kappa}_{(i)}^{\text{ref}})^{-1}} \underbrace{\mathbf{D}^T \boldsymbol{\sigma} \left(\mathbf{E} + \mathbf{D} \tilde{\mathbf{u}}_{(i)}, \mathbf{h}_{(i)}\right)}_{-\mathbf{b}_{(i)}}. \quad (4.1)$$

The PCG algorithm for solving (4.1) is presented in Algorithm 1. Next, considering that $\partial \tilde{\mathbf{u}}_{(i)} = \mathbf{D} \tilde{\mathbf{u}}_{(i)}$, in the left hand side of (4.1), we substitute $\mathbf{D} \delta \tilde{\mathbf{u}}$, with $\delta \partial \tilde{\mathbf{u}}$ (i.e. re-interpreting the gradient of displacement increment as the increment of displacement gradient) and rewrite (4.1) as:

$$\left(\mathbf{D}^T \mathbf{C}_{(i)}^{\text{ref}} \mathbf{D}\right)^{-1} \mathbf{D}^T \mathbf{C}_{(i)} \delta \partial \tilde{\mathbf{u}}_{(i+1)} = - \left(\mathbf{D}^T \mathbf{C}_{(i)}^{\text{ref}} \mathbf{D}\right)^{-1} \mathbf{D}^T \boldsymbol{\sigma} \left(\mathbf{E} + \partial \tilde{\mathbf{u}}_{(i)}, \mathbf{h}_{(i)}\right), \quad (4.2)$$

with $\mathbf{\Gamma}_{(i)}^{\text{ref}}$ standing for the periodic discretized Green's operator of a reference medium with elastic tensor \mathbf{C}^{ref} . Considering that the $\tilde{\mathbf{u}}_{(i+1)}$ belongs to a gradient field with zero average, the mean of the right hand side of (4.2) is also zero. Generally speaking, if the gradient of two fields with zero mean are equal then the two fields are equal. Therefore, we can take discrete derivative of both sides of (4.2) which yields:

$$\underbrace{\mathbf{D} \left(\mathbf{D}^T \mathbf{C}_{(i)}^{\text{ref}} \mathbf{D}\right)^{-1} \mathbf{D}^T \mathbf{C}_{(i)}}_{\mathbf{\Gamma}_{(i)}^{\text{ref}}} \delta \partial \tilde{\mathbf{u}}_{(i+1)} = - \underbrace{\mathbf{D} \left(\mathbf{D}^T \mathbf{C}_{(i)}^{\text{ref}} \mathbf{D}\right)^{-1} \mathbf{D}^T \boldsymbol{\sigma} \left(\mathbf{E} + \partial \tilde{\mathbf{u}}_{(i)}, \mathbf{h}_{(i)}\right)}_{\mathbf{\Gamma}_{(i)}^{\text{ref}}}, \quad (4.3)$$

By taking the 4th rank symmetrizing identity tensor as the elastic tensor of the reference materials ($\mathbf{C}_{(i)}^{\text{ref}} = \mathbf{I}_s$), the operator $\mathbf{\Gamma}_{(i)}^{\text{ref}}$ boils down to the compatibility projection $\mathbf{G}_{\mathbf{I}_s} = \mathbf{D} \left(\mathbf{D}^T \mathbf{I}_s \mathbf{D}\right)^{-1} \mathbf{D}^T$ (equivalent to the definition of the projection operator presented in (1.10) in Chapter 1) projecting an arbitrary field to its closest compatible part in the least square sense considering the L^2 -norm of difference with a gradient field (shown

by Leute et al. (2021)). The linearized equation (4.3) becomes:

$$\underbrace{\mathbf{D} \left(\mathbf{D}^T \mathbf{I}_s \mathbf{D} \right)^{-1} \mathbf{D}^T}_{\mathbf{G}_{\mathbf{I}_s}^T} \mathbf{C}_{(i)} \delta \partial \tilde{\mathbf{u}}_{(i+1)} = - \underbrace{\mathbf{D} \left(\mathbf{D}^T \mathbf{I}_s \mathbf{D} \right)^{-1} \mathbf{D}^T}_{\mathbf{G}_{\mathbf{I}_s}^T} \boldsymbol{\sigma} \left(\mathbf{E} + \partial \tilde{\mathbf{u}}_{(i)}, \mathbf{h}_{(i)} \right) \quad (4.4)$$

$$\mathbf{G}_{\mathbf{I}_s}^T \mathbf{C}_{(i)} \delta \tilde{\boldsymbol{\varepsilon}}_{(i+1)} = - \mathbf{G}_{\mathbf{I}_s}^T \boldsymbol{\sigma} \left(\mathbf{E} + \tilde{\boldsymbol{\varepsilon}}_{(i)}, \mathbf{h}_{(i)} \right), \quad (4.5)$$

which is identical to (1.21) given that the solution iterates are compatible (periodic gradient) fields. As a result, we have actually shown that the strain-based and the displacement-based schemes are identical in case of $\mathbf{C}_{(i)}^{\text{ref}} = \mathbf{I}_s$.

4.1.1 Projection operator with a reference material

I extend the derivation of the projection operator introduced by Leute et al. (2021) and introduce a general projection operator that with an arbitrary admissible reference material \mathbf{C}^{ref} instead of \mathbf{I}_s . This allows proving the general equivalence with the displacement-based scheme with an arbitrary admissible reference material. To this end, I follow a similar approach to the derivation of the projection operator proposed by Leute et al. (2021).

Assume that $\boldsymbol{\zeta} : \Omega \rightarrow \mathbb{R}^{d \times d}$ is an arbitrary tensor field. The difference between $\boldsymbol{\zeta}$ and a compatible gradient field $\partial \tilde{\mathbf{v}} \in \mathcal{E}$ (gradient of arbitrary field $\tilde{\mathbf{v}}$ with zero mean) can be simply noted as $(\partial \tilde{\mathbf{v}} - \boldsymbol{\zeta})$ which needs to be minimized to make $\boldsymbol{\zeta}$ the compatible contribution of $\tilde{\mathbf{v}}$.

As an extension of the derivation of Leute et al. (2021), I take an energy norm of the residual (taking $\mathbf{C}^{\text{ref}} = \mathbf{I}_s$ yields the same projection as that of Leute et al. (2021)),

$$\|\mathbf{R}(\tilde{\mathbf{u}})\|_{\mathbf{C}^{\text{ref}}} = \int_{\Omega} (\partial \tilde{\mathbf{v}} - \boldsymbol{\zeta})^T \mathbf{C}^{\text{ref}} (\partial \tilde{\mathbf{v}} - \boldsymbol{\zeta}) \, d\mathbf{x}, \quad (4.6)$$

as we want to minimize the difference of $\boldsymbol{\zeta}$ and $\partial \tilde{\mathbf{v}}$ we can take $\|\mathbf{R}(\tilde{\mathbf{u}})\|_{\mathbf{C}^{\text{ref}}}$ as an objective

Chapter 4. Equivalence of the strain-based and displacement-based schemes

function, which using a quadrature rule, in discrete form reads as:

$$\mathcal{R} = ||\mathbf{R}(\tilde{\mathbf{u}})||_{\mathbf{C}_{\mathbf{W}(i)}^{\text{ref}}} = (\mathbf{D}\tilde{\mathbf{v}} - \boldsymbol{\zeta})^T \mathbf{C}_{\mathbf{W}(i)}^{\text{ref}} (\mathbf{D}\tilde{\mathbf{v}} - \boldsymbol{\zeta}), \quad (4.7)$$

where $\mathbf{C}_{\mathbf{W}(i)}^{\text{ref}}$ is the weighted discretized elastic tensor of the reference materials with the weights taken from the quadrature rule applied. $\mathbf{C}_{\mathbf{W}(i)}^{\text{ref}}$ can be obtained from the weight matrix \mathbf{W} and the elastic matrix of the reference material \mathbf{C}^{ref} according to $\mathbf{C}_{\mathbf{W}(i)}^{\text{ref}} \equiv \mathbf{W}\mathbf{C}^{\text{ref}}$

Now, by minimizing \mathcal{R} we can find a displacement field that minimizes the norm of the difference of the tensor field $\boldsymbol{\zeta}$ and the gradient of $\tilde{\mathbf{v}}$ in a space with the metric of $\mathbf{C}_{\mathbf{W}(i)}^{\text{ref}}$. For this end we need to differentiate \mathcal{R} with respect to $\tilde{\mathbf{v}}$:

$$\frac{\partial \mathcal{R}}{\partial \tilde{\mathbf{v}}} = 2\mathbf{D}^T \mathbf{C}_{\mathbf{W}(i)}^{\text{ref}} \mathbf{D}\tilde{\mathbf{v}} - \mathbf{D}^T \mathbf{C}_{\mathbf{W}(i)}^{\text{ref}} \boldsymbol{\zeta} - \boldsymbol{\zeta}^T \mathbf{C}_{\mathbf{W}(i)}^{\text{ref}} \mathbf{D} = \mathbf{0}. \quad (4.8)$$

Solving for $\tilde{\mathbf{v}}$ yields the linear system of equation:

$$\underbrace{\mathbf{D}^T \mathbf{C}_{\mathbf{W}(i)}^{\text{ref}} \mathbf{D}}_{\mathbf{K}_{\text{ref}}} \tilde{\mathbf{v}} = \mathbf{D}^T \mathbf{C}_{\mathbf{W}(i)}^{\text{ref}} \boldsymbol{\zeta}. \quad (4.9)$$

Solution of (4.9) gives $\tilde{\mathbf{v}}$ as

$$\tilde{\mathbf{v}} = \underbrace{\left(\mathbf{D}^T \mathbf{C}_{\mathbf{W}(i)}^{\text{ref}} \mathbf{D} \right)^{-1}}_{\mathbf{K}_{\text{ref}}^{-1}} \mathbf{D}^T \mathbf{C}_{\mathbf{W}(i)}^{\text{ref}} \boldsymbol{\zeta}. \quad (4.10)$$

The compatible contribution of the field $\boldsymbol{\zeta}$ is actually the gradient of $\tilde{\mathbf{v}}$; therefore, we can write compatible contribution of $\boldsymbol{\zeta}$ as:

$$\check{\boldsymbol{\zeta}} = \mathbf{D}\tilde{\mathbf{v}} = \underbrace{\mathbf{D} \left(\mathbf{D}^T \mathbf{C}_{\mathbf{W}(i)}^{\text{ref}} \mathbf{D} \right)^{-1} \mathbf{D}^T \mathbf{C}_{\mathbf{W}(i)}^{\text{ref}}}_{\mathbf{G}_{\mathbf{C}_{\mathbf{W}(i)}^{\text{ref}}}} \boldsymbol{\zeta} = \mathbf{G}_{\mathbf{C}_{\mathbf{W}(i)}^{\text{ref}}} \boldsymbol{\zeta}. \quad (4.11)$$

As a result, the general projection operator $\mathbf{G}_{\mathbf{C}_{\mathbf{W}(i)}^{\text{ref}}} = \mathbf{D} \left(\mathbf{K}^{\text{ref}} \right)^{-1} \mathbf{D}^T \mathbf{C}_{\mathbf{W}(i)}^{\text{ref}}$ with $\mathbf{K}_{\text{ref}} = \mathbf{D}^T \mathbf{C}_{\mathbf{W}(i)}^{\text{ref}} \mathbf{D}$ can be used instead of $\mathbf{G}_{\mathbf{I}_s}$ in the strain-based method. In general, the closer $\mathbf{C}_{\mathbf{W}(i)}^{\text{ref}}$ can reconstruct the anisotropy of the effective tangent of the RVE the more speed-up gain it gives for solving the linearized equilibrium equation (Ladecký et al.

(2022b)). It is notable that, in solid mechanics, the anisotropy includes both anisotropy in geometrical coordinate directions as well as anisotropy between different components of the stress and strain, for instance the Poisson effect. Ladecký et al. (2021) have shown that taking the \mathbf{C}^{ref} with a Poisson ratio roughly resembling that of the RVE accelerates the solution roughly by 50%.

A closer look to (4.11) and comparing it with the expression of $\mathbf{G}_{\mathbf{l}_s}$ reveals that, there is an extra $\mathbf{C}_{\mathbf{w}(i)}^{\text{ref}}$ appearing on the right side of the definition of the $\mathbf{G}_{\mathbf{C}_{\mathbf{w}(i)}^{\text{ref}}}$ that is missing in the linearized strain-based equilibrium equation (4.3). This causes two problems in solving the linearized equilibrium equation for the strain field. i. The solution field is in a stress field space \mathcal{S} mapped from the strain field \mathcal{E} with the transformation matrix $\mathbf{C}_{\mathbf{w}(i)}^{\text{ref}}$, ii. The coefficient matrix of the linearized equilibrium equation is not symmetric in case of using $\mathbf{G}_{\mathbf{C}^{\text{ref}}}$ which makes CG inapplicable to solve the equation iteratively. One possible solution to format the strain-based linearized equation equivalent to the displacement based equation resolving the aforementioned problems is pre-multiplying both sides of the equation with $\left(\mathbf{C}_{\mathbf{w}(i)}^{\text{ref}}\right)^{-1}$. Accordingly, we can rewrite (4.3) as:

$$\left(\mathbf{C}_{\mathbf{w}(i)}^{\text{ref}}\right)^{-1} \mathbf{G}_{\mathbf{C}_{\mathbf{w}(i)}^{\text{ref}}}^T \mathbf{C}_{(i)} \delta \tilde{\mathbf{e}}_{(i+1)} = - \left(\mathbf{C}_{\mathbf{w}(i)}^{\text{ref}}\right)^{-1} \mathbf{G}_{\mathbf{C}_{\mathbf{w}(i)}^{\text{ref}}}^T \boldsymbol{\sigma} \left(\mathbf{E} + \tilde{\mathbf{e}}_{(i)}, \mathbf{h}_{(i)}\right). \quad (4.12)$$

One efficient way of handling the pre-multiplied $\left(\mathbf{C}_{\mathbf{w}(i)}^{\text{ref}}\right)^{-1}$ is taking it as a preconditioner in the linear solver algorithm and solving the linearized equilibrium using a PCG solver. The PCG algorithm used to solve the preconditioned strain-based with arbitrary $\mathbf{C}_{\mathbf{w}(i)}^{\text{ref}}$ is presented in Algorithm 2. We have adopted this scheme for examining the equivalence of the displacement-based scheme and the generalized strain-based scheme in the presented example in the following of the chapter.

4.1.2 Termination criterion

As mentioned earlier, in order to compare the performance of the strain-based and displacement-based scheme, numerically, we need to adopt an identical termination criterion for the linear solvers (PCG) used to solve the linearized equations ((4.1) and (4.12)) and also for the nonlinear solver (Newton solver here).

Chapter 4. Equivalence of the strain-based and displacement-based schemes

The termination criterion of the linear solvers used in the strain-based and the displacement-based schemes is based on the L^2 -norm of the residual (stress in strain-based and force in displacement-based scheme). Clearly these are not identical and make the comparison of solution step count with equal tolerance infeasible. Therefore, here we define an energy norm as the measure used in the termination criterion of the linear solvers by contracting the energy conjugate pairs in both the methods; strain and stress in the strain-based method; and displacement and force in the displacement based method.

This choice of convergence measure aligns with the nature of conjugate gradient method which minimizes the energy norm of the error. As shown by Vondrejč and de Geus (2017) the quality of the homogenized properties of a RVE is actually proportional to the energy norm $\left\| \mathbf{e}_k^{(i)} \right\|_{\mathbf{K}}^2$ of the solution error defined as:

$$\left\| \mathbf{e}_k^{(i)} \right\|_{\mathbf{K}}^2 = \left\| \mathbf{x}^{(i)} - \mathbf{x}_k^{(i)} \right\|_{\mathbf{K}}^2 = (\mathbf{x}^{(i)} - \mathbf{x}_k^{(i)})^T \mathbf{K} (\mathbf{x}^{(i)} - \mathbf{x}_k^{(i)}). \quad (4.13)$$

with \mathbf{K} being the system matrix and $\mathbf{x}^{(i)}$ being the displacement field in the displacement-based method and \mathbf{K} being the tangent and $\mathbf{x}^{(i)}$ being the strain field in the strain-based scheme. $\mathbf{x}_k^{(i)}$ is basically the value of the DoF field at k^{th} iteration of the linear solver.

As explained earlier, the usual termination criterion is based on the L^2 -norm of the residual $\mathbf{r}_k^{(i)}$ which can be written as function of $\mathbf{e}_k^{(i)}$ as:

$$\left\| \mathbf{r}_k^{(i)} \right\|_2^2 = \mathbf{e}_k^{(i)T} \mathbf{K}^T \mathbf{K} \mathbf{e}_k^{(i)} = \left\| \mathbf{e}_k^{(i)} \right\|_{\mathbf{K}^T \mathbf{K}}^2, \quad (4.14)$$

because $\mathbf{r}_k^{(i)} = \mathbf{b} - \mathbf{K} \mathbf{x}_k^{(i)} = \mathbf{K} \mathbf{x}^{(i)} - \mathbf{K} \mathbf{x}_k^{(i)} = \mathbf{K} (\mathbf{x}^{(i)} - \mathbf{x}_k^{(i)}) = \mathbf{K} \mathbf{e}_k^{(i)}$. We propose to measure $\left\| \mathbf{r}_k^{(i)} \right\|_{\mathbf{M}^{-1}}^2$ instead of $\left\| \mathbf{r}_k^{(i)} \right\|_2^2$

$$\left\| \mathbf{r}_k^{(i)} \right\|_{\mathbf{M}^{-1}}^2 = \mathbf{e}_k^{(i)T} \mathbf{K}^T \mathbf{M}^{-1} \mathbf{K} \mathbf{e}_k^{(i)} = \left\| \mathbf{e}_k^{(i)} \right\|_{\mathbf{K}^T \mathbf{M}^{-1} \mathbf{K}}^2. \quad (4.15)$$

If \mathbf{M} is a good approximation of \mathbf{K} , then $\mathbf{M}^{-1} \mathbf{K} \approx \mathbf{I}$ and

$$\left\| \mathbf{e}_k^{(i)} \right\|_{\mathbf{K}^T \mathbf{M}^{-1} \mathbf{K}}^2 \approx \left\| \mathbf{e}_k^{(i)} \right\|_{\mathbf{K}}^2; \quad (4.16)$$

the approximation of the error in the energy norm.

In our case, \mathbf{M} is built in the same way as \mathbf{K} , but for constant reference material $\mathbf{C}_{\mathbf{W}(i)}^{\text{ref}}$ (see $(\mathbf{K}_{(i)}^{\text{ref}})^{-1}$ and $\mathbf{K}_{(i)}$ in (4.1)). \mathbf{M} always approximates \mathbf{K} better than \mathbf{I} and thus energy norm $\|\mathbf{r}_k^{(i)}\|_{\mathbf{M}^{-1}}^2$ is a better approximation of $\|\mathbf{e}_k^{(i)}\|_{\mathbf{K}}^2$ rather than $\|\mathbf{r}_k^{(i)}\|^2$. Therefore, it is a better measure to terminate the PCG algorithm. In addition, it can be easily computed by contracting 2 of the existing fields in the algorithm as explained in the following.

In order to normalize these measures, we normalize them to the initial residual $\|\mathbf{r}_0^{(i)}\|_{\mathbf{M}^{-1}}^2$. For initial guess $\tilde{\mathbf{u}}_0^{(i)} = \mathbf{0}$ we get

$$\|\mathbf{r}_0^{(i)}\|_{\mathbf{M}^{-1}}^2 = \|\mathbf{b}^{(i)}\|_{\mathbf{M}^{-1}}^2 = \|\mathbf{K}\tilde{\mathbf{u}}^{(i)}\|_{\mathbf{M}^{-1}}^2 = \|\tilde{\mathbf{u}}^{(i)}\|_{\mathbf{K}^T\mathbf{M}^{-1}\mathbf{K}}^2, \quad (4.17)$$

the approximation of the energy norm of the solution $\tilde{\mathbf{u}}^{(i)}$. From the computational viewpoint, the evaluation of the approximate energy norm is of nearly zero cost, as we need the product $(\mathbf{r}_0^{(i)})^T \mathbf{M}^{-1} \mathbf{r}_0^{(i)} = \|\mathbf{r}_0^{(i)}\|_{\mathbf{M}^{-1}}^2$ in every PCG iteration. Considering that $\mathbf{z}_k^{(i)} \equiv \mathbf{M}^{-1} \mathbf{r}_k^{(i)}$ is already defined and computed in the PCG algorithm the only calculation needed to compute $\|\mathbf{r}_k^{(i)}\|_{\mathbf{M}^{-1}}^2$ is contracting (computing inner product of) $\mathbf{r}_k^{(i)}$ and $\mathbf{z}_k^{(i)}$. These modifications are presented in lines 9 and 19 of Algorithm 1 and lines 9 and 17 of Algorithm 2.

In addition, we need to make the termination criterion of the nonlinear solvers also identical. The termination criterion of the Newton solver that we use as the nonlinear solver is based on the norm of the difference of the DoF field after and before the linear solver call (solution increment). It is basically the squared norm of the difference of the strain field in the strain-based scheme and the displacement in the displacement-based scheme, i.e. the size of the step caused by solution of the linear solver. Therefore, the termination criteria are clearly different in case of these two schemes.

We have chosen to modify the termination criterion of the displacement solver as the value of the strain field is basically available in the nonlinear solver as the strain value is calculated at the quadrature points since they are needed for material stress and stiffness evaluation. Accordingly, by changing the termination criterion of the displacement-based nonlinear solver we can make the termination criterion of the two schemes identical with, basically, no overhead. For the strain-based solver, on the other hand, doing the same trick and taking error with $\|\mathbf{r}_0^{(i)}\|_{\mathbf{C}^{-1}}^2$ yields similar energy norm of the reference material.

Having identical termination criteria (for both linear and nonlinear solvers) allows us to compare the number of linear and nonlinear solution steps of the two schemes by keeping the tolerances constant. The explained termination criteria were incorporated into the schemes and are used in the example presented in Section 4.2 to compare strain-based and displacement-based schemes in practice.

4.2 Examples and Result

In Section 4.1, we explained the equivalence of an extended form of strain-based FFT-accelerated scheme we developed (Leute et al. (2021)) and the geometrically optimal preconditioned displacement based FE scheme we developed (Ladecký et al. (2022b)). The necessary modifications needed for observing this equivalence in practice (such as solving the strain-based method using PCG in the general case of the projection defined with a reference material with elastic tensor \mathbf{C}^{ref} and the changes needed in the termination criterion) were elaborated in Section 4.1. Here, by using the concepts and the modifications explained in Section 4.1, we compare solving equilibrium of a RVE containing nonlinear materials with identical FE discretization and show that under equivalent circumstances (same discretization and same termination criterion). The number of solution steps of two solution schemes solving a nonlinear homogenization problem are the same.

4.2.1 Homogenization of a hyper-elasto-plastic micro-structure

The example is adopted from de Geus et al. (2017) where the micro-structure of the RVE consists of hyperelasto-plastic material. The constitutive law of such materials is explained in details in (Simo (1992); Geers (2004); Simo and Hughes (2006); de Souza Neto et al. (2008)). The yield criterion of the hyperelasto-plastic constitutive law which bounds the elastic domain of the material response has the form:

$$\tau_{eq} - \tau_y(\boldsymbol{\varepsilon}_p) \leq 0 \quad (4.18)$$

where $\boldsymbol{\varepsilon}_p$ is the accumulated plastic strain, τ_y is the yield stress which is a function of $\boldsymbol{\varepsilon}_p$, and τ_{eq} is a function of the elastic contribution of the strain at equilibrium. The yield stress $\tau_y(\boldsymbol{\varepsilon}_p)$ can be obtained as a linear function of $\boldsymbol{\varepsilon}_p$ as:

$$\tau_{y0}(\boldsymbol{\varepsilon}_p) = \tau_{y0} + H\boldsymbol{\varepsilon}_p \quad (4.19)$$

where τ_{y0} (initial yield stress) and H (hardening coefficient) are material parameters.

I discretized the solution domain of the example by 441×441 -pixel grid. It consists of two steel phases martensite and ferrite that are identical in their elastic regime (mechanically identical as far as they are both in their elastic regime); however, their initial yield stress and hardening coefficients are contrasted here by $\varphi = 2$ as the phase contrast between martensite and ferrite as:

$$\tau_{y0}^{\text{ferrite}} \times \varphi = \tau_{y0}^{\text{martensite}} \quad (4.20)$$

$$H^{\text{ferrite}} \times \varphi = H^{\text{martensite}} \quad (4.21)$$

Total macroscopic deformation gradient

$$\mathbf{F} = \frac{\sqrt{3}}{2} \begin{bmatrix} 0.995 & 0 \\ 0 & -0.995 \end{bmatrix} \quad (4.22)$$

is applied in 5 load increments.

I solved the problem with both strain-based and displacement-based schemes. The solution domain is discretized in both schemes with linear triangular elements. I set the Newton tolerance to $\eta^{\text{NW}} = 10^{-5}$ and (P)CG tolerance to $\eta^{\text{CG}} = 10^{-5}$. We solve three cases with identity $\mathbf{C}^{\text{ref}} = \mathbf{I}$, symmetrized identity $\mathbf{C}^{\text{ref}} = \mathbf{I}_s$, and mean value $\mathbf{C}^{\text{ref}} = \mathbf{C}_{\text{mean}}$ reference materials, where the preconditioner is made with a reference material with the stiffness matrix of weighted average RVE of the tangent of the underlying phases.

The distributions of global plastic strain ε_p obtained for two solution schemes are shown in the first row of Figure 4.1, which shows that the solution of the two schemes are identical. The regions of details of the ε_p (the second row) also approves the identity of the solution fields in further detail. In addition, the number of Newton's method steps and

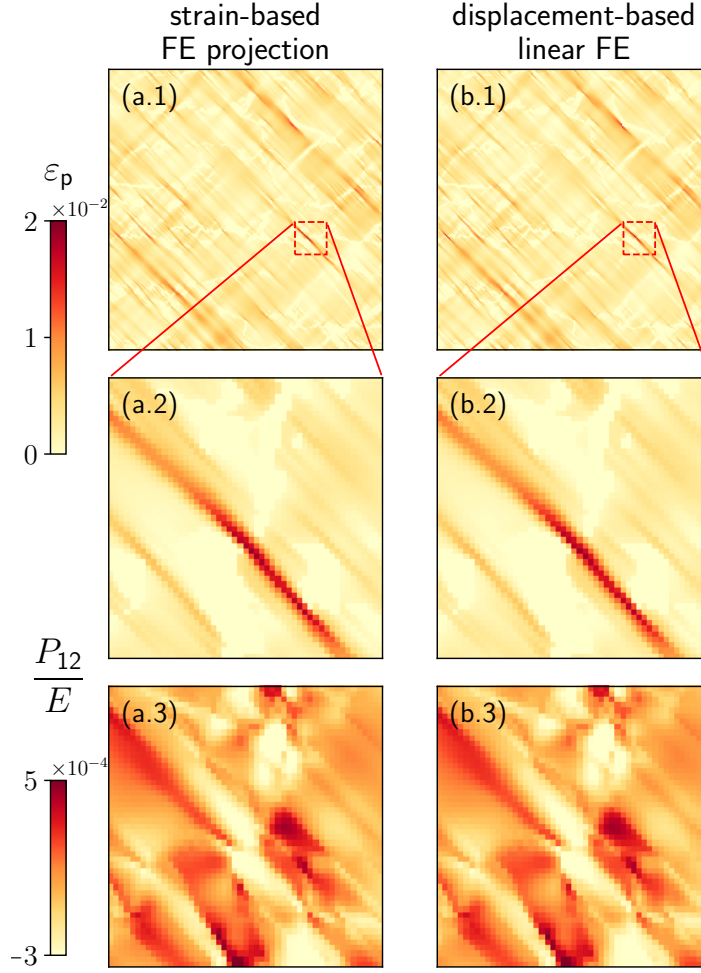


Figure 4.1: Global plastic strains ε_p in dual-phase steel with applied deformation gradient (4.22) in row **(1)** with local details in row **(2)**. Row **(3)** shows accompanying normalized shear stresses P_{12} in detailed area. Discretization schemes in columns: **(a)** the strain-based scheme with FE projection operator with two linear triangular elements and **(b)** the displacement-based FE scheme with two linear triangular elements. All quantities are averaged per pixel.

	\mathbf{C}^{ref}	strain-based(SB)	displacement-based (DB)
Newton steps		9	9
(P)CG steps	I	861	861
	I_s	609	609
	C_{mean}	457	457

Table 4.1: The number of Newton’s method steps and the total number of (P)CG steps required to solve the finite strain elasto-plastic problem of Section 4.2 for a three choices of reference material, with Newton tolerance $\eta^{\text{NW}} = 10^{-5}$ and (P)CG tolerance $\eta^{\text{CG}} = 10^{-5}$. solution schemes from left to right: the strain-based scheme with FE projection operator with two linear triangular elements, the displacement based FE scheme with two linear triangular elements. The count of solution steps exhibits the equivalence of displacement FE scheme presented by Ladecký et al. (2022b) and strain-based FE scheme presented by Leute et al. (2021).

the total number of (P)CG iterations needed to solve the problem with strain-based and displacement-based approaches are shown in Table 4.1 which highlights their equivalence.

4.3 Conclusion

In this chapter, we have shown the equivalence of the displacement-based scheme presented by Ladecký et al. (2021) and an extended version of the strain-based scheme presented by Leute et al. (2021). Their equivalence has been shown in terms of the linearized equilibrium equations of both of the schemes. It has been also tested and validated in practice in a nonlinear finite element problem presented in Section 4.2. As a result, displacement-based and strain-based formulations converge equally and the only decision-making consideration regarding the possibility of efficient implementation. However, we have opted to use the strain-based method for ASR damage homogenization problem due to some minor advantages, for instance, imposing macroscopic loads in form of stress is more straightforward in the strain-based formulation and has been already worked out by Lucarini and Segurado (2019a). Accordingly, the simulations in Chapter 7 are carried out using the strain-based formulation with FE discretization.

4.4 Algorithms

Algorithm 1 displacement-based preconditioned CG

$$\text{Num.} \quad \text{scheme:} \quad \underbrace{(\mathbf{D}^T \mathbf{C}_W^{\text{ref}} \mathbf{D})^{-1}}_{\mathbf{M}^{-1}} \underbrace{\mathbf{D}^T \mathbf{C}_W^{(i)} \mathbf{D}}_{\mathbf{K}} \delta \tilde{\mathbf{u}}^{(i+1)} =$$

$$- \underbrace{(\mathbf{D}^T \mathbf{C}_W^{\text{ref}} \mathbf{D})^{-1}}_{\mathbf{M}^{-1}} \underbrace{\mathbf{D}^T \mathbf{W} \sigma(\mathbf{E} + \mathbf{D} \tilde{\mathbf{u}}^{(i)}, \mathbf{h}^{(i)})}_{-\mathbf{b}} \quad (4.1)$$

```

1:  $\delta \tilde{\mathbf{u}}_0$  ▷ Initial displacement
2:  $\mathbf{E}$  ▷ Macroscopic gradient field

3:  $\mathbf{M} = \mathbf{D}^\top \mathbf{C}_W^{\text{ref}} \mathbf{D}$  ▷ Preconditioner
4:  $\mathbf{K} = \mathbf{D}^\top \mathbf{C}_W^{(i)} \mathbf{D}$  ▷ System (Stiffness) matrix
5:  $\mathbf{b} = -\mathbf{D}^\top \mathbf{W} \sigma(\mathbf{E} + \mathbf{D} \tilde{\mathbf{u}}^{(i)}, \mathbf{h}^{(i)})$  ▷ Right hand side

6: procedure DB PCG( $\delta \tilde{\mathbf{u}}_0, \mathbf{K}, \mathbf{b}, \mathbf{M}, \text{tol}, \text{it}_{\max}$ )
7:    $\mathbf{r}_0 := \mathbf{b} - \mathbf{K} \delta \tilde{\mathbf{u}}_0$ 
8:    $\mathbf{z}_0 := \mathbf{M}^{-1} \mathbf{r}_0$ 
9:    $nr_0 := \|\mathbf{r}_0\|_{\mathbf{M}^{-1}} \equiv \mathbf{r}_0^\top \mathbf{z}_0$  ▷ initial residual
10:   $\mathbf{p}_0 := \mathbf{z}_0$ 

11:   $k := 0$ 
12:  while  $k \leq \text{it}_{\max}$  do ▷  $k = 0, 1, \dots, \text{it}_{\max}$ 
13:     $\mathbf{K} \mathbf{p}_k = \mathbf{K} \mathbf{p}_k$ 
14:     $\alpha_k = \frac{\mathbf{r}_k^\top \mathbf{z}_k}{\mathbf{p}_k^\top \mathbf{K} \mathbf{p}_k}$ 

15:     $\delta \tilde{\mathbf{u}}_{k+1} = \delta \tilde{\mathbf{u}}_k + \alpha_k \mathbf{p}_k$ 
16:     $\mathbf{r}_{k+1} = \mathbf{r}_k - \alpha_k \mathbf{K} \mathbf{p}_k$ 
17:
18:     $\mathbf{z}_{k+1} = \mathbf{M}^{-1} \mathbf{r}_{k+1}$ 
19:     $nr_{k+1} = \|\mathbf{r}_{k+1}\|_{\mathbf{M}^{-1}} \equiv \mathbf{r}_{k+1}^\top \mathbf{z}_{k+1}$ 

20:    if  $\frac{nr_{k+1}}{nr_0} < \text{tol}$  then
21:      return  $\tilde{\mathbf{u}}_{k+1}$ 

22:     $\beta_k = \frac{\mathbf{r}_{k+1}^\top \mathbf{z}_{k+1}}{\mathbf{r}_k^\top \mathbf{z}_k}$ 
23:     $\mathbf{p}_{k+1} = \mathbf{z}_{k+1} + \beta_k \mathbf{p}_k$ 

24:     $k = k + 1$ 
25:  return  $\delta \tilde{\mathbf{u}}_k$  ▷ if  $\text{it}_{\max}$  reached

```

Algorithm 2 strain-based preconditioned CG with \mathbf{C}^{ref} as preconditioner

Num. scheme: $\underbrace{\left(\mathbf{C}^{\text{ref}}\right)^{-1}}_{\mathbf{M}^{-1}} \underbrace{\mathbf{G}_{\mathbf{C}^{\text{ref}}}^T \mathbf{C}_{(i)}}_{\mathbf{K}} \delta \tilde{\mathbf{e}}_{(i+1)} = - \underbrace{\left(\mathbf{C}^{\text{ref}}\right)^{-1}}_{\mathbf{M}^{-1}} \underbrace{\mathbf{G}_{\mathbf{C}^{\text{ref}}}^T \boldsymbol{\sigma} \left(\mathbf{E} + \tilde{\mathbf{e}}_{(i)}, \mathbf{h}_{(i)}\right)}_{-\mathbf{b}}, \quad (4.12)$

1: $\delta \tilde{\mathbf{e}}_0 \equiv \mathbf{D} \delta \tilde{\mathbf{u}}_0$ ▷ Initial displacement gradient
2: \mathbf{E} ▷ Macroscopic gradient field

3: $\mathbf{M}^* = \mathbf{C}^{\text{ref}}$ ▷ Preconditioner
4: $\mathbf{K}^* = \mathbf{G}_{\mathbf{C}^{\text{ref}}}^T \mathbf{C}_{(i)}$ ▷ System (Stiffness) matrix
5: $\mathbf{b}^* = \mathbf{G}_{\mathbf{C}^{\text{ref}}}^T \boldsymbol{\sigma} \left(\mathbf{E} + \tilde{\mathbf{e}}_{(i)}, \mathbf{h}_{(i)}\right) = \mathbf{G}_{\mathbf{C}^{\text{ref}}}^T \boldsymbol{\sigma} \left(\mathbf{E} + \mathbf{D} \tilde{\mathbf{u}}_{(i)}, \mathbf{h}_{(i)}\right)$ ▷ Right hand side

6: **procedure** SB PCG($\delta \tilde{\mathbf{e}}_0, \mathbf{M}^*, \mathbf{K}^*, \mathbf{b}^*, \text{tol}, \text{it}_{\max}$)

7: $\mathbf{r}_0^* := \mathbf{b}^* - \mathbf{K}^* \delta \tilde{\mathbf{e}}_0$
8: $\mathbf{z}_0^* := \mathbf{M}^{*-1} \mathbf{r}_0^*$
9: $nr_0^* = \|\mathbf{r}_0^*\|_{(\mathbf{M}^*)^{-1}} \text{ (or } \sqrt{\mathbf{r}_0^{*\top} \mathbf{z}_0^*} \text{)}$ ▷ initial residual
10: $\mathbf{p}_0^* := \mathbf{z}_0^*$

11: $k := 0$
12: **while** $k \leq \text{it}_{\max}$ **do** ▷ $k = 0, 1, \dots, \text{it}_{\max}$
13: $\alpha_k^* = \frac{\mathbf{r}_k^{*\top} \mathbf{z}_k^*}{\mathbf{p}_k^{*\top} \mathbf{K}^* \mathbf{p}_k^*}$
14: $\delta \tilde{\mathbf{e}}_k = \delta \tilde{\mathbf{e}}_k + \alpha_k^* \mathbf{p}_k^*$
15: $\mathbf{r}_{k+1}^* = \mathbf{r}_k^* - \alpha_k^* \mathbf{K}^* \mathbf{p}_k^*$

16: $\mathbf{z}_{k+1}^* := \mathbf{M}^{*-1} \mathbf{r}_{k+1}^*$
17: $nr_{k+1}^* = \|\mathbf{r}_{k+1}^*\| \text{ (or } \sqrt{\mathbf{r}_{k+1}^{*\top} \mathbf{z}_{k+1}^*} \text{)}$

18: **if** $\frac{nr_{k+1}^*}{nr_0^*} < \text{tol}$ **then** ▷ Convergence test
19: **return** $\delta \tilde{\mathbf{e}}_{k+1}$

20: $\beta_k^* = \frac{\mathbf{r}_{k+1}^{*\top} \mathbf{z}_{k+1}^*}{\mathbf{r}_k^{*\top} \mathbf{z}_k^*}$
21: $\mathbf{p}_{k+1}^* = +\mathbf{z}_{k+1}^* + \beta_k^* \mathbf{p}_k^*$

22: $k = k + 1$
23: **return** $\delta \tilde{\mathbf{e}}_k$ ▷ if it_{\max} reached

5 Non-Convexity

The projection-based spectral scheme (strain-based scheme) and the preconditioned FEM scheme (displacement-based scheme), explained in Chapter 1, due to their optimal spectral characteristics of their linearized system (Pultarová and Ladecký (2021)), enable us to benefit from the computational advantages of iterative solvers such as Newton-CG. Their favorable spectral characteristics result in great scaling for solving RVEs with large number of discretization points. However, solving (1.21) with CG solver needs the Hessian matrix of the linearized system to be SPSD which is not the case in several mechanical homogenization problems such as system containing meta-materials (Li. (2017)) or continuum damage (Bažant (1976); Marvi-Mashhadi et al. (2020)).

Therefore, in order to be able to benefit from the computational speed-up offered by these FFT-accelerated schemes for problems with symmetric non-positive semi definite (SNPSD) system matrices, we need to employ other iterative solvers. Some quasi-Newton solvers such as limited-memory Broyden–Fletcher–Goldfarb–Shanno (LBFGS), and trust-region (TR) Newton solver are among possible candidates capable of handling non-convex problems. In this chapter, a modified TR Newton solver for homogenization problems is introduced. The introduced solver is a robust and memory efficient solver capable of handling non-convexity in an iterative fashion.

The potential of the TR solvers (as well as quasi-Newton solvers) has not been exploited in computational homogenization, since, in a considerable part of the literature, conventional FEM direct solvers are the standard choice for computational homogenization.

As a result, the main challenge of using TR and quasi Newton solvers in computational homogenization, namely missing an explicit expression of the objective function in the equivalent energy minimization counterpart of the equilibrium solution, has not been addressed to the authors' best knowledge. I addressed this problem in the following of this chapter after a review over the standard TR Newton solver. In this chapter, we develop a modified TR Newton-CG algorithm based on an introduced first order approximation incremental energy functional (FAIEF). At the end, some examples are also presented to exhibit and examine the performance of the presented modified TR solver.

The content of this chapter is mainly taken from a submitted paper entitled Non-convex, ringing-free, FFT-accelerated solver using an incremental approximate energy functional (Falsafi et al. (2022)).

5.1 Method

5.1.1 Trust region solver

The trust-region method (TRM) is a numerical optimization method capable of solving nonlinear and non-convex optimization problems. Basically, it uses a model (sub-problem) approximating the original objective function within a trust region around the current solution iterate. The TRM performs minimization based on the approximation made by the model (typically quadratic) within the trust region. In contrast to line search methods, in TRM, the maximum permissible step size is pre-determined; however, the size of the trust-region at each iterate evolves based on how well the model represents the actual objective function. The model is expected to be a good representation of the original objective function inside the trust region.

Figure 5.1 depicts a visual representation of the TRM in a 2D schematic problem. The black iso-contours represent the non-convex function $E(\mathbf{x})$ we want to minimize, whose minimizer is indicated by the black $+$ sign. It is assumed that the iterative solution process starts with the initial guess of \mathbf{x}_0 noted by orange $+$ in the figure. The red iso-contours are the contours expressing the second order model $m(\mathbf{x})$ estimating the

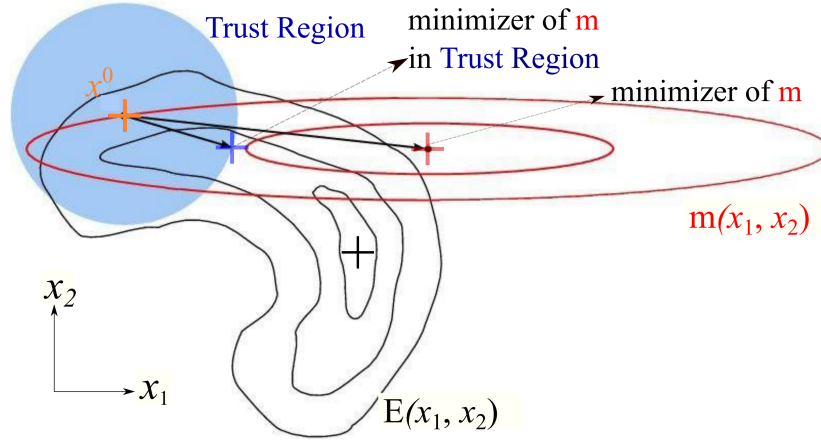


Figure 5.1: Schematic of TRM in 2D state space

objective function around \mathbf{x}^0 . The global minimizer of these quadratic iso-contours is depicted as red $+$ in the figure. The blue shaded area is the trust region area (the hyper-sphere in which we trust the estimation of the model $m(\mathbf{x})$).

In a single standard trust region solution iteration, the minimizer of the model function inside the trust region (shown as the blue $+$ sign) is found and taken as the next iteration if a desirable reduction of the original function $E(\mathbf{x})$ is realized in this step. In other words, in the trust region solution strategy, optimization is carried out by minimizing a model function $m(\mathbf{x})$ trusted up to a certain radius (shaded in blue in Figure 5.1) around the current iterate as a proxy problem (sub-problem). The approximate model is derived from the local information gathered from the objective function.

If in a trust region solution step the boundary of the trust region is crossed, the intersection point is taken as the new iterate and it gets accepted if the objective function has reduced compared to previous iterate. In addition, in case the Hessian becomes SNPSD during the solution process the intersection of the previous search direction and the boundary of the trust region is taken as new trial iterate and checked and accepted in case objective function decreases in the step. In any of these cases, if the new iterate does not realize objective function reduction, the trust region shrinks and the algorithm retries minimizing the model in the updated trust region.

There is no a-priori knowledge of the radius of the trust region in which the model can adequately approximate the objective function. In addition, the accuracy of the model degrades by moving away from the current iteration. Therefore, it is crucial to determine the proper trust region radius and to regulate it consistently during the solution process.

To this end, based on the model's match with the original objective function, the trust region is adjusted in each iteration. As a general rule, the trust region can be expanded if the approximate model fits the original problem well. In contrast, the trust region shrinks if the approximate model fails to estimate the original function adequately (Hsia et al. (2017)). It is therefore necessary to access the original objective function of the equivalent optimization problem if one needs to use a TR solver in its standard formulation.

Let us recall the basic equations that we tend to solve to obtain the equilibrium of the RVE. Let's again examine a periodic RVE in which we want to solve for equilibrium, for illustration purposes see Figure 1.5. We adopt a small strain formulation, in order to derive the equilibrium equation. The micro-structure is assumed to experience a displacement field of $\chi : \Omega_0 \rightarrow \Omega$ which maps the grid points from undeformed positions Ω_0 to their deformed configurations Ω . As the material response corresponding to the position \mathbf{x} , given the local strain $\boldsymbol{\varepsilon}(\mathbf{x})$, the stress and the tangent of the material can be computed using the constitutive law of the material at that point. The fields $\boldsymbol{\varepsilon}$ and $\boldsymbol{\sigma}$ are energy conjugates. Let us consider the total energy function (we do not need to have the explicit expression for that), equivalent to the original objective function of a homogenization problem, of the RVE as:

$$U = \sum_Q u(\boldsymbol{\varepsilon}^Q, \mathbf{h}(\mathbf{x}^Q))w^Q, \quad (5.1)$$

where u denotes energy at Q s, which are the discretization quadrature points, and $\mathbf{h}(\mathbf{x})$ represents the internal variables of the material.

The solution of the equilibrium equation (1.5), in particular, corresponds to the critical point of the total energy function (5.1). In the strain-based scheme, the equilibrium problem is solved in the strain space. According to the fact that the energy conjugate of strain is stress, the gradient of the energy with respect to strain is actually the stress

tensor. In addition, the Hessian of the objective function corresponds to the tangent stiffness of the material at the discretization points,

$$\nabla_{\varepsilon} U = \boldsymbol{\sigma}, \quad (5.2)$$

$$\nabla_{\varepsilon}^2 U = \mathbb{B}. \quad (5.3)$$

One possible sub-problem model (and probably the most common form) of the TR solver is a quadratic energy function approximation in form of:

$$m_i(\mathbf{p}_i) = U(\boldsymbol{\varepsilon}_i) + (\nabla_{\varepsilon} U)^T \mathbf{p}_i + \frac{1}{2} \mathbf{p}_i^T (\nabla_{\varepsilon}^2 U) \mathbf{p}_i, \quad s.t. \|\mathbf{p}_i\| < R_i, \quad (5.4)$$

where, in the Newton TR solver, \mathbb{B}_i is taken as the Hessian matrix of the energy evaluated at quadrature points at i^{th} load step and R_i is the radius of the trust region. \mathbf{p}_i is a solution step in the strain space. Here, the energy functional is taken as a direct function of strain at i^{th} solution step as in the projection based formulation the equations are solved in the strain space. Other TR solvers are also possible using different choices for the matrix \mathbb{B}_i . Accordingly, the model function in a trust-region Newton solver can be expressed as:

$$m_i(\mathbf{p}_i) = U(\boldsymbol{\varepsilon}_i) + \boldsymbol{\sigma}_i^T \mathbf{p}_i + \frac{1}{2} \mathbf{p}_i^T \mathbb{B}_i \mathbf{p}_i, \quad s.t. \|\mathbf{p}_i\| < R_i, \quad (5.5)$$

The agreement of the actual objective function ($U(\boldsymbol{\varepsilon}_i + \mathbf{p}_i)$) and the model ($m_i(\mathbf{p}_i)$) at the new iterate is evaluated by a scalar variable ρ_i at the i^{th} iterative step, defined as:

$$\rho_i \equiv \frac{U(\boldsymbol{\varepsilon}_i) - U(\boldsymbol{\varepsilon}_i + \mathbf{p}_i)}{m_i(\mathbf{0}) - m_i(\mathbf{p}_i)}. \quad (5.6)$$

In the trust region algorithm, the value of ρ_i , as set forth by Nocedal and Wright (2006), determines how the trust region size will be updated as well as whether or not the proposed step will be accepted.

It is relatively simple to calculate the denominator of the right hand side of (5.6) ($\Delta m_i = m_i(\mathbf{0}) - m_i(\mathbf{p}_i)$) according to the definition of $m_i(\mathbf{p}_i)$ given in (5.5). For calculation of the nominator, an explicit expression of the origin objective function

(equivalent to stored energy in mechanical engineering problems) is necessary in the standard TR solver. In mechanical homogenization problems, however, the objective function is often not calculable (at least easily), since the actual energy density function of most materials is very complex (or even impossible to compute). A FAIEF that allows us to use TR solvers to solve generic non-convex mechanical homogenization problems is presented here. In order to derive the incremental energy functional, first, the Taylor series of the actual energy function U is expanded at both $\boldsymbol{\varepsilon}_i$ and $\boldsymbol{\varepsilon}_i + \mathbf{p}_i$ points as:

$$U(\boldsymbol{\varepsilon}_i + \mathbf{p}_i) = U(\boldsymbol{\varepsilon}_i) + (\nabla_{\boldsymbol{\varepsilon}} U|_{\boldsymbol{\varepsilon}_i})^T \mathbf{p}_i + \frac{1}{2} \mathbf{p}_i^T (\nabla_{\boldsymbol{\varepsilon}}^2 U|_{\boldsymbol{\varepsilon}_i}) \mathbf{p}_i + \mathcal{O}(\|\mathbf{p}_i\|^3) \quad (5.7a)$$

$$\begin{aligned} U(\boldsymbol{\varepsilon}_i) &= U((\boldsymbol{\varepsilon}_i + \mathbf{p}_i) - \mathbf{p}_i) \\ &= U(\boldsymbol{\varepsilon}_i + \mathbf{p}_i) - (\nabla_{\boldsymbol{\varepsilon}} U|_{\boldsymbol{\varepsilon}_i + \mathbf{p}_i})^T \mathbf{p}_i + \frac{1}{2} \mathbf{p}_i^T (\nabla_{\boldsymbol{\varepsilon}}^2 U|_{\boldsymbol{\varepsilon}_i + \mathbf{p}_i}) \mathbf{p}_i + \mathcal{O}(\|\mathbf{p}_i\|^3) \end{aligned} \quad (5.7b)$$

Subtracting (5.7a) from (5.7b) and dropping higher order terms yields:

$$\begin{aligned} U(\boldsymbol{\varepsilon}_i + \mathbf{p}_i) - U(\boldsymbol{\varepsilon}_i) &\approx \\ &\frac{1}{2} \left((\nabla_{\boldsymbol{\varepsilon}} U|_{\boldsymbol{\varepsilon}_i})_i^T \mathbf{p}_i + (\nabla_{\boldsymbol{\varepsilon}} U|_{\boldsymbol{\varepsilon}_i + \mathbf{p}_i})_i^T \mathbf{p}_i \right) + \\ &\frac{1}{4} \left(\mathbf{p}_i^T (\nabla_{\boldsymbol{\varepsilon}}^2 U|_{\boldsymbol{\varepsilon}_i}) \mathbf{p}_i - \mathbf{p}_i^T (\nabla_{\boldsymbol{\varepsilon}}^2 U|_{\boldsymbol{\varepsilon}_i + \mathbf{p}_i}) \mathbf{p}_i \right) \end{aligned} \quad (5.8)$$

Truncating (5.8) up to first order gives:

$$\Delta U = U(\boldsymbol{\varepsilon}_i) - U(\boldsymbol{\varepsilon}_i + \mathbf{p}_i) \approx \overline{\Delta U} = \frac{\boldsymbol{\sigma}(\boldsymbol{\varepsilon}_i + \mathbf{p}_i) + \boldsymbol{\sigma}(\boldsymbol{\varepsilon}_i)}{2} : \mathbf{p}_i. \quad (5.9)$$

The right hand side of (5.9) consists of the stress tensors before and after incrementing strain field $\boldsymbol{\varepsilon}_i$ with the trial step \mathbf{p}_i , which are already evaluated at all of the quadrature points. To take $\overline{\Delta U}$ as a valid estimation of ΔU , it is necessary to keep the load increments small. This is usually not a concern since it can be controlled by the size of the applied load steps, which for nonlinear problems is already small to enable the nonlinear iterative solvers to converge to equilibrium even in case of nonlinear elliptic problems (problems with positive semi definite (PSD) matrix).

Furthermore, it is vital that the variation of the resulting displacement field remains

bounded. For instance, problems such as buckling under a prescribed growing force do not satisfy boundedness of the displacement field around the critical load; therefore, does not converge using the modified trust-region solver presented here. On the other hand, problems such as mechanics damage modeling are solvable despite their non-convex energy functional, using the modified TR solver presented here given that the applied load increments are controlled to be small.

The actual system energy reduction, ΔU , in the nominator of (5.6) can be replaced by $\overline{\Delta U}$ calculated according to the FAIEF noted in (5.8) which gives an estimation of ρ_i ; denoted by $\bar{\rho}_i$ according to:

$$\bar{\rho}_i = \frac{\overline{\Delta U}}{\Delta m_i}. \quad (5.10)$$

It is notable that the evaluation of $\bar{\rho}_i$ needs the stress of the previous solution step to be stored.

Introducing the FAIEF enables us to use the robust trust region algorithm in cases that the explicit expression of U function is missing. The pseudo-algorithm of the strain-based trust-region solver is presented in Algorithm 4, showing how the scalar value ρ_i (or its estimated counterpart $\bar{\rho}_i$) is used to make decisions of accepting or rejecting trial step ($\delta \epsilon$) as well as shrinking or expanding the trust region. As shown in Algorithm 4, the memory overhead of using Trust region Newton-CG is, merely, storing the flux (stress) field at the previous solution step which does not significantly impact the overall memory requirement of the solver algorithm compared to Newton-CG since the stress field is smaller than the most memory consuming fields in the algorithm. The stress field is actually 9 times in 3D and 4 times in 2D smaller than the biggest fields stored in the algorithm which are the projection and the tangent fields.

The predicted reduction of the model (m_i) will always be non-negative since the step \mathbf{p}_i is calculated by minimizing the model m_i over the region that includes $\mathbf{p} = \mathbf{0}$. Therefore, if $\bar{\rho}_i$ is negative, the first order approximation of the objective function at the new iterate ($U(\epsilon_i + \mathbf{p}_i)$) is greater than the current value of the objective function value ($U(\epsilon_i)$), thus the step must be rejected. On the other hand, if $\bar{\rho}_i$ is close to 1, it is safe to expand the trust region for the next step since the model m_i and the original objective function U are in good agreement over the solution step \mathbf{p}_i . When $\bar{\rho}_i$ is positive but smaller

than one, the trust region is not altered, however in the case when $\bar{\rho}_i$ is close to zero or negative, the trust region is shrunk by reducing R_i at the next iteration. How these decisions are made is detailed in Algorithm 4.

The solution of the subproblem (minimizer of m within the ball of radius R) is easy to find when \mathbb{B} is positive definite and the minimizer is located within the trust region (equivalent to finding an unconstrained minimizer of the quadratic function m). There is no such simple solution to the subproblem in other cases, in which the minimizer resides on the boundary of the trust region. The constrained linear solver used here as the sub-problem solver is based on the solver introduced by Steihaug (Nocedal and Wright (2006); Steihaug (1983)) which is used to generate the trial solution step \mathbf{p}_i .

In addition, in order to make the linear solver robust to numerical rounding error problems a reset algorithm based on the work of Powell (1977), and Dai et al. (2004) was added to the linear solver algorithm. The used reset mechanism replaces the conjugate gradient step with a restart step (for instance, the gradient descent step). Whenever two successive solution steps inside the linear solver (\mathbf{r}_j and \mathbf{r}_{j-1}) are not sufficiently orthogonal to each other. The measure expressing the orthogonality of the solution steps can be calculated via the inner product of consecutive solution steps:

$$r_{\triangleleft} = \frac{|\mathbf{r}_j \cdot \mathbf{r}_{j-1}|}{\|\mathbf{r}_j\|^2}. \quad (5.11)$$

Comparing the measure, r_{\triangleleft} , with a constant value in the range of (0.1, 0.9) has been proposed as the decision criterion for restarting CG, I chose 0.2 as suggested by Powell (1977), hence the restart procedure is invoked if the measure r_{\triangleleft} is greater than 0.2.

Several quasi-Newton solvers, e.g. LBFGS, also depend on the explicit expression of the objective function. For instance, in satisfying the first Wolfe condition in determining the step size in LBFGS, evaluation of reduction of the objective function is needed Nocedal and Wright (2006). Using the approximated strain energy reduction $\overline{\Delta U}$ instead of ΔU makes use of these quasi-Newton solvers possible as well. As derived here, the introduced incremental approximation of the objective function, specifically, enables us to use TR Newton-CG solver following the algorithm given in Algorithm 4 (as the Newton nonlinear solver) and the algorithm given in Algorithm 3 as the subproblem solver. The introduced

approximate energy functional can be generalized to solve any other problem in which the explicit objective function is not available or not easy to calculate while the gradient and Hessian of the objective function are available.

5.2 Examples and Results

In the following, two examples are presented to demonstrate the performance solver developed above. As a real world non-convex example using the developed Newton TR solver, in Chapter 7, I model ASR damage in a meso-scale model with rather complex constitutive law. In this chapter, I first compare the performance of the modified TR solver with that of the Newton-CG solver and the standard TR solver on a very simple example. This example deals with a 1-dimensional (1D) damage spring system where the potential energy functional of the system is known. The standard TR solver can therefore be used on this system. Second, I test the correctness of the solution of the solver considering a convex system. The Eshelby inhomogeneity, whose analytical solution is available, is selected as the second example. This example allows us to compare the generated solution of the modified TR solver with the analytical solution of the problem.

5.2.1 Minimal 1D non-convex example

As a simple mechanical system with non-convex energy functional, a periodic 1D spring system (schematic shown in Figure 5.2a) consisting of three nodes connected with springs (k_0 , k_1 , and k_2) is taken as the first example. The springs k_1 and k_2 are elastic springs with $k_1 = k_2 = k$, while k_0 is a bi-linear damage spring, i.e. after a certain deformation threshold γ_0 its mechanical behavior switches from elastic to strain-softening. The force-displacement response of the k_0 spring is depicted in Figure 5.2b, The tangent of the strain-softening phase of the constitutive behavior is αk . Therefore, the post-peak stiffness matrix of the system becomes:

$$\mathbf{K} = \begin{bmatrix} (1 + \alpha)k & -k & -\alpha k \\ -k & 2k & -k \\ -\alpha k & -k & (1 + \alpha)k \end{bmatrix}, \quad (5.12)$$

Table 5.1: Solvers used to solve the 1D spring example

Solver		Functions needed as input		
		Objective (Energy)	Gradient (Force)	Hessian (Stiffness)
i	Newton-CG SciPy	✗	✓	✓
ii	Trust Region Newton-CG Scipy	✓	✓	✓
iii	Modified Trust Region Newton-CG	✗	✓	✓

whose eigenvalues are $[\lambda_1 = 0, \lambda_2 = 3k, \lambda_3 = (2\alpha + 1)k]$. The third eigenvalue can be either positive or negative and for values $\alpha < -(\frac{1}{2})$, the system becomes SNPSD, since it has one negative eigenvalue.

The problem has been solved with $k = 1.0$, $\gamma_0 = 0.1$ and for different values of α . The boundary condition of mean stretch equal to $\bar{x} = 0.11$, large enough to invoke post peak behavior of the k_0 spring, is imposed. Three different solvers listed in Table 5.1 are employed to solve the equilibrium of the 1D spring system. The functions needed to be explicitly evaluated in the algorithm of these solvers are listed in Table 5.1. The main difference between the modified and the standard TR solver, as noted in Table 5.1, is that explicit evaluation of the objective function is not needed in the modified solver.

The strain energy functional of the system as a function of the independent variable x_0 (the stretch of 0^{th} spring) for the imposed boundary condition of $\bar{x} = 0.11$ is represented in Figure 5.3 for three different values of α , respectively from left to right, corresponding to convex, meta-stable, and concave energy surfaces. The variation of energy, and the final solution of the solvers listed in Table 5.1 are depicted in this figure. It is clear that in non-convex cases, Newton-CG solver is not capable of finding the energy functional minimum as it fails finding the minimizer, while both standard and modified trust-region Newton-CG solvers converged to the minimizer of the energy (equilibrium points). The hyper-parameters of the standard and the modified TR solvers (such as initial and maximum trust-region radius) are chosen to be identical. This causes the solution steps of the solvers to coincide solving the 1D spring system as depicted in Figure 5.3.

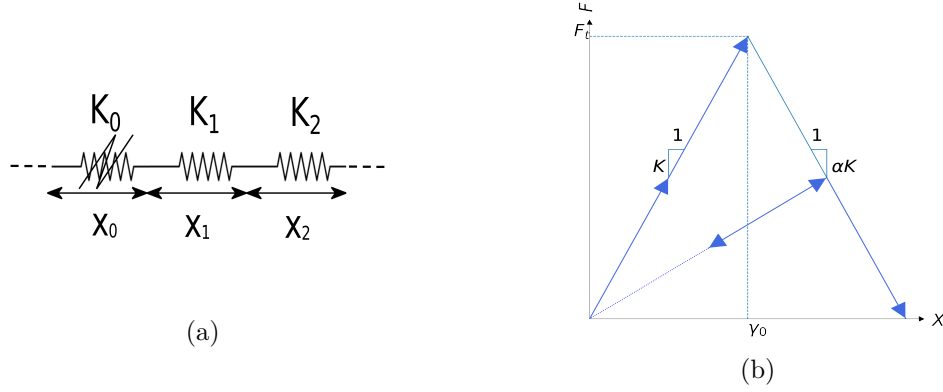


Figure 5.2: Periodic 1D spring example schematic and constitutive behavior of the damage spring 0^{th} spring, a. Schematic of 1-D damage spring example, b. Force-displacement response of the damage spring

The transition of the energy functional from convexity to non-convexity is depicted in Figure 5.3 for $\alpha < -0.5$. In Figure 5.3a, the energy functional is convex over all values of x_0 while in Figure 5.3b and Figure 5.3c, the energy functional around the transition point ($x_0 = 0.1$) of the spring k_0 is non-convex.

This simple example can clearly show the equivalence of the obtained results with that of the standard trust region algorithm. The availability of the energy functional of this example makes the standard trust-region solver applicable. However, in general non-convex homogenization problems, the energy functional is not always available; therefore, the standard trust-region solver is not an option and one can only use the modified version with the approximated energy functional.

5.2.2 Convex example

In order to examine the introduced modified trust-region solver for solving convex problems, a small-strain Eshelby inhomogeneity elasticity problem is chosen here as the second numerical example. The Eshelby inhomogeneity is an ellipsoidal body embedded in an infinite elastic medium, where the material properties of the inhomogeneity differ from those of the matrix. The analytical solution of the problem is known (Eshelby (1957, 1959); Mura (1982); Meng et al. (2012)). A 2D example identical to the Eshelby inhomogeneity example presented by Leute et al. (2021) is considered here as our second example. The linear FE discretization of Leute et al. (2021) is adopted and the problem

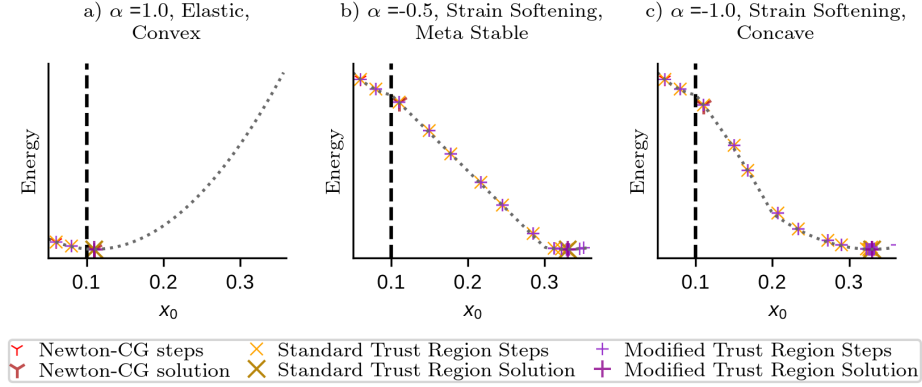


Figure 5.3: The energy of 1D spring system, schematically depicted in Figure 5.2a, over the solution trajectory of different solvers as a function of x_0 , for (a) Convex $\alpha = 1$ (b) Meta-stable $\alpha = -1/2$, (c) non-convex $\alpha = -1$ problems. In non-convex cases ((b), (c)), there is a concave point located at $x_0 = 0.1$ as the strain-softening behavior of the k_0 springs is activated from that point on. Dashed line is the energy functional of the system as a function of x_0

is solved by two solvers, namely the plain Newton-CG solver and our modified TR Newton-CG solver.

The schematic of the RVE geometry is presented in column (a) of Figure 5.4. Figure 5.4 illustrates the solution of both Newton-CG and modified trust-region Newton-CG (column (b)). Column (c) shows the difference of the solution of these two solvers. Figure 5.4 depicts that the solution of the two solvers are identical with a relative error tolerance in the order of magnitude of the tolerance of the solver algorithm (η_{NR} in Algorithm 4).

The number of CG solver and nonlinear solution steps needed to solve for equilibrium versus trust radius variation (maximum trust region radius) is plotted in Figure 5.5 showing that, in a convex problem, the number of nonlinear solution steps as well as the accumulative number of the CG solver steps needed to reach the solution decays to that of Newton-CG solver as the size of the trust region increases.

Figure 5.5 also shows that, in order to maintain the same number of nonlinear solution steps for solving a problem with twice as many grid points in each direction (4 times discretization points), the trust region should be roughly doubled. This correlation is rooted in the fact that the trust region radius is actually the radius of the hypersphere in the space of problem unknowns (strain in case of strain-based solver). Imagine

the discretization of a problem is refined by a factor of N in each spatial direction in a 2D problem. This results in N^2 scaling of the number of the discretization points. Accordingly, the size of an equivalent solution step scales by N , in other words, an equivalent step in the problem with refined discretization is N times larger. As a result, to maintain the ratio of the solution step length constant with respect to trust region radius, the trust region radius should be scaled by a factor of N . This finding suggests that in order to use the trust region solver effectively one should loosen the trust region for larger problem sizes. However, it should be noted that the trust region radius is actively corrected during the solution of non-convex problems according to the accuracy of the sub-problem model functional.

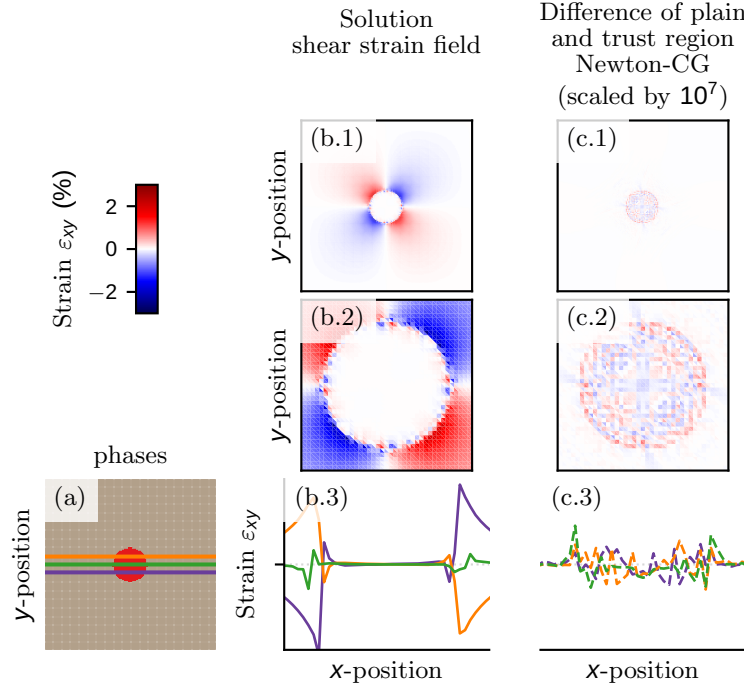


Figure 5.4: Solution of the cylindrical Eshelby inhomogeneity problem under mean spherical strain of 0.01 ($\varepsilon_{xx} = \varepsilon_{yy} = 0.01, \varepsilon_{xy} = 0$). Column a. shows the phase distribution of a soft inhomogeneity cylindrical Eshelby inhomogeneity problem (showing the inhomogeneity in red). Column b. shows solution of cylindrical Eshelby inhomogeneity with Newton-CG and TR Newton-CG as they look the same. The column (c) consists the difference of Newton-CG and TR Newton-CG solutions scaled by a factor of 10^7 . The slight difference shown in this column is below the solution tolerance meaning that the solutions are numerically equivalent. The first row shows the variation of the shear strain all over the solution domain. Second row shows the same variable zoomed around the inhomogeneity. The third row shows the variation of shear strain over the green, purple and orange cuts (located at the center-line, $r/2$ below and above of the center-line of the inhomogeneity) in subfigure a. The third row also corresponds to the zoomed area around the inhomogeneity.

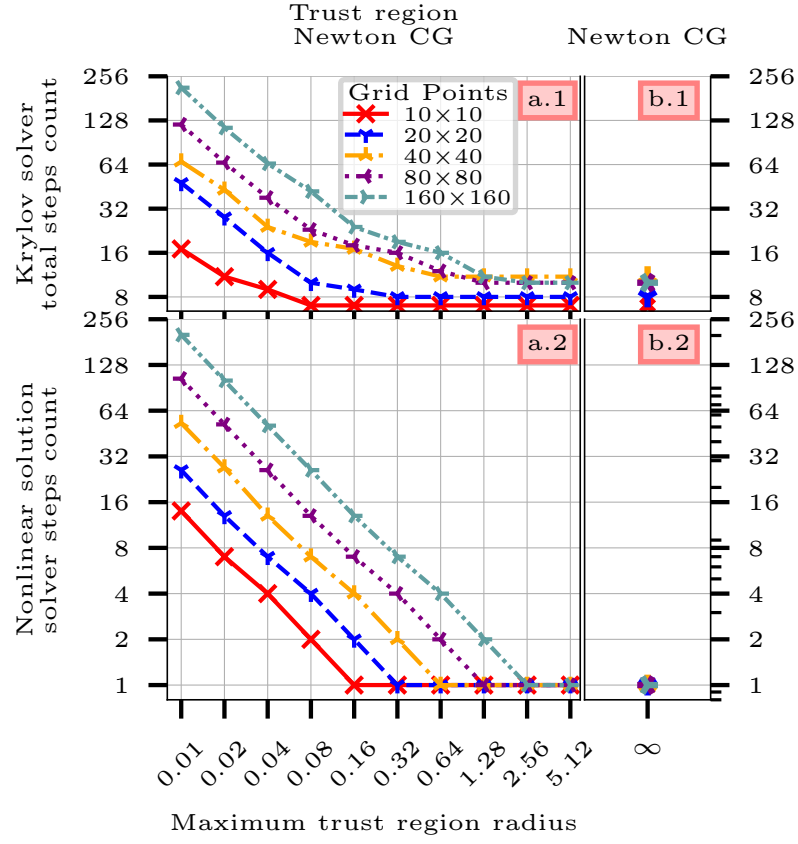


Figure 5.5: Number of CG steps (the first row) and number of nonlinear solution steps (the second row) needed for solving the Eshelby inhomogeneity problems for different number of grid points for the Newton-CG (column 2) and as a function of initial trust region radius of TR Newton-CG (column 1). Number of nonlinear steps includes Newton steps and failed trial or trust region steps during the equilibrium solution

5.3 Conclusion

In this section, I presented a incremental strain energy approximation functional (FAIEF), which facilitates the use of fast ringing-free spectral solvers for non-convex problems, such as damage mechanics. The approximated energy functional derived based on Taylor expansion of the energy functional of the system enables exploiting the computational benefits of quasi-Newton solvers as well as TR Newton-CG solvers in computational homogenization simulations. The modified TR solver presented here is capable of solving non-convex problems without requiring the explicit formula of the energy functional of the system. The introduced incremental strain energy functional also makes it possible to use quasi-Newton solvers such LBFGS in the computational homogenization problems as well.

The validity of the modified TR solver was tested against the standard TR solver using a simple non-convex problem. The performance of the modified solver was examined solving a convex problem and was also validated against a Newton-CG solver. Later, in Chapter 7 of this dissertation, I will simulate a real-world homogenization problem, meso-scale ASR damage, with the non-convex energy functional by means of the presented modified TR solver. The comparison of the outcome of the meso-scale ASR damage modeling with the literature shows a very good agreement. These validations assure the effectiveness of the introduced energy functional approximation and the modified TR solver in practice.

5.4 Algorithms

Algorithm 3 Pseudo-algorithm of CG-Steihaug solver with reset

```

1: Solve for  $\mathbf{r}$  with system Matrix  $\mathbb{B}$  and initial RHS  $\mathbf{b}_0$ 
2:  $\eta_{CG}$  ▷ CG tol.
3:  $j_{CG, \max}$  ▷ max iterations of CG
4: Set  $\mathbf{r}_0 \leftarrow \mathbf{0}, \mathbf{b}_0 \leftarrow \mathbf{b}, \mathbf{d}_0 \leftarrow -\mathbf{b}_0$  ▷ initialization

5: if  $\|\mathbf{b}\| \leq \eta_{cg}$  then
6:   Return  $\mathbf{p}_i = \mathbf{r}_0 = \mathbf{0}$  ▷ already at solution

7: for  $j = 0, 1, 2, \dots, j_{CG, \max}$  do
8:   if  $\mathbf{d}_j^T \mathbb{B}_i \mathbf{d}_j \leq 0$  then ▷ non-convex
9:     find  $\tau$  such that  $\mathbf{p}_i = \mathbf{r}_j + \tau \mathbf{d}_j$  minimizes  $m_i(\mathbf{p}_i)$ 
       and satisfies  $\|\mathbf{p}_i\| = R_i$ 
10:    Return  $\mathbf{p}_i$ 

11:    $\alpha_j \leftarrow \mathbf{r}_j^T \mathbf{r}_j / \mathbf{d}_j^T \mathbb{B}_i \mathbf{d}_j$ 
12:    $\mathbf{r}_{j+1} \leftarrow \mathbf{r}_j + \alpha_j \mathbf{d}_j$  ▷ update the iterate

13:   if  $\|\mathbf{r}_{j+1}\| \geq R_i$  then ▷ hit the boundary of trust region
14:     find  $\tau$  such that  $\mathbf{p}_i = \mathbf{r}_j + \tau \mathbf{d}_j$  minimizes  $m_i(\mathbf{p}_i)$ 
       and satisfies  $\|\mathbf{p}_i\| = R_i$ 
15:     Return  $\mathbf{p}_i$ 

16:   if  $\|\mathbf{r}_{j+1}\| \leq \eta_{cg}$  then ▷ convergence satisfied
17:     Return  $\mathbf{p}_i = \mathbf{r}_{j+1}$ 

18:   if  $\mathbf{r}_{j+1} \cdot \mathbf{r}_j / \mathbf{r}_{j+1} \cdot \mathbf{r}_{j+1} > 0.2$  then ▷ successive steps are not conjugate
19:      $\mathbf{r}_{j+1} = \mathbb{B} \mathbf{r}_j - \mathbf{b}_j$  ▷ reset CG
20:      $\beta_{j+1} \leftarrow 0$  ▷ reset CG
21:   else
22:      $\beta_{j+1} \leftarrow \mathbf{r}_{j+1}^T \cdot \mathbf{r}_{j+1} / \mathbf{r}_j^T \cdot \mathbf{r}_j$ 

23:    $\mathbf{d}_{j+1} \leftarrow -\mathbf{r}_{j+1} + \beta_{j+1} \mathbf{d}_j$  ▷ compute new update direction

```

Algorithm 4 Pseudo-algorithm of strain-based Newton-CG trust-region algorithm in small strain formulation

```

1: Initialize:
2:  $\eta_{eq}, \eta_{NR}, \eta_{CG}, \eta_{up}$  ▷ equilibrium-, Newton, CG and update tol.
3:  $i_{NR,max}, i_{CG,max}$  ▷ max iterations Newton-Raphson and CG
4:  $R, R_{max}, \eta_{up}$ . ▷ trust region radius, maximum radius
5:  $\varepsilon = \mathbf{0}$  ▷ small-strain initial guess

6: for  $\Delta\varepsilon = \Delta\varepsilon_1, \Delta\varepsilon_2, \dots$  do ▷ macroscopic strain increments
7:    $\varepsilon = \varepsilon + \Delta\varepsilon$  ▷ increment grad with load step
8:    $\varepsilon_{eval} = \varepsilon + \varepsilon_{eig}$  ▷ adding eigenstrain if needed
9:    $\sigma, \mathbb{B} = \sigma(\varepsilon_{eval}), \mathbb{B}(\varepsilon_{eval})$  ▷ evaluate stress and tangent
10:   $b = -\mathbb{G} : \sigma(\varepsilon_{eval})$  ▷ RHS calculation
11:  if  $\|b\| \leq \eta_{eq}$  then
12:    Newton-Raphson converged
13:    Go to line 6 ▷ linear problem, next load step
14:  for  $i = 0, 1, 2, \dots, i_{NR,max}$  do ▷ Newton-Raphson iteration
15:    Prepare coefficient matrix of the linearized equation  $\mathbb{G} : \mathbb{B} : \delta\varepsilon = b$ 
16:    Solve  $\mathbb{G} : \mathbb{B} : \delta\varepsilon = b$  for  $\delta\varepsilon$  with Steihaug CG Nocedal and Wright (2006):
17:      in  $i_{CG,max}$  steps to accuracy  $\eta_{CG}$ , Algorithm 3
18:     $\Delta m_i = \sigma : \delta\varepsilon + 1/2 \delta\varepsilon : \mathbb{B} : \delta\varepsilon$  ▷ energy model change
19:     $\sigma^{trial} = \sigma(\varepsilon + \delta\varepsilon)$  ▷ stress evaluation with trial strain
20:     $\overline{\Delta U} = 1/2 (\sigma : \delta\varepsilon + \sigma^{trial} : \delta\varepsilon)$  ▷ 1st order energy approx. change
21:     $\bar{\rho} = \overline{\Delta U} / \Delta m_i$ 
22:    if  $\bar{\rho} < 1/4$  then
23:       $R \leftarrow 1/4 R$  ▷ shrink trust region
24:    else
25:      if  $\bar{\rho} > 3/4$  and  $\|\delta\varepsilon\| = R$  then
26:         $R \leftarrow \min(2R, R_{max})$  ▷ expand trust region if possible
27:      if  $\bar{\rho} > \eta_{up}$  then
28:         $\varepsilon \leftarrow \varepsilon + \delta\varepsilon$  ▷ increment grad with accepted solution step
29:         $r_{NR} = \|\delta\varepsilon\| / \|\varepsilon\|$  ▷ calculating relative residual
30:         $\varepsilon_{eval} = \varepsilon + \varepsilon_{eig}$  ▷ adding eigen strain if needed
31:         $\sigma, \mathbb{B} = \sigma(\varepsilon_{eval}), \mathbb{B}(\varepsilon_{eval})$  ▷ evaluate stress and tangent
32:         $b = -\mathbb{G} : \sigma(\varepsilon_{eval})$  ▷ RHS calculation with updated grad
33:        if  $\|\delta\varepsilon\| < R$  then
34:          if  $\|b\| \leq \eta_{eq}$  or  $r_{NR} \leq \eta_{NR}$  then
35:            Newton-Raphson is converged
36:            Go to line 6 ▷ next load step
37:          else
38:            Go to line 14 ▷ next Newton loop iteration
39:        else
40:          Go to line 14 ▷ next Newton loop iteration
41:      else
42:        Trial step rejected
43:        Go to line 14 ▷ next Newton loop iteration

```

6 Algorithmically consistent tangent for the strain-based FFT-accelerated scheme

A large majority of natural and manufactured materials have a heterogeneous or composite microstructure. Biological tissues (Holzapfel et al. (2000)), concrete (Mehta and Monteiro (2014)), magno-electronic (Eerenstein et al. (2006)) composites, and shape memory alloys (Bhattacharya (2003)) are prominent examples of materials. The objective of homogenization is, essentially, prediction of the effective properties of a heterogeneous micro-structure of these materials. As a result, the homogenization process involves equilibrium solution of a RVE followed by effective properties calculation. In multi-scale models, specifically, the effective properties are passed to the macro-scale model as the response of the micro-structure of the RVE.

In the mechanical engineering context, the mean stress and effective tangent are the main effective responses of the micro-structure. Achieving quadratic convergence of a Newton-Raphson scheme at a macroscopic scale mandates evaluating effective tangent of the RVEs at the microscopic scale (Göküzüm and Keip (2017)). In addition, in the meso-scale ASR damage model, which interests me in this thesis, one of the most important measures to quantify the extent of ASR progress is the stiffness loss of the RVE. As a result, it is crucial to have a robust and efficient algorithm for calculating the effective tangent of the RVE.

For simple geometries, analytical homogenization schemes can compute the effective tangent, for example by using consistent method (Budiansky (1965); Hill (1965)), the Mori-Tanaka method (Mori and Tanaka (1973)) and the so called differential method (Norris

Chapter 6. Algorithmically consistent tangent for the strain-based FFT-accelerated scheme

(1985)). However, for rather complex micro-structures, analytical methods are no longer suitable and computational methods should replace them for determining the effective properties.

Among computational homogenization schemes, an explicit expression of the consistent tangent for FEM using the localization tensor is developed by Miehe (2003); Keip et al. (2014); Yvonnet (2019). For the original FFT-accelerated homogenization scheme as developed by Moulinec and Suquet (1994), a consistent tangent has been introduced by Göküzüm and Keip (2017). However, for the FG scheme (de Geus et al. (2017)) and the generalized projection-based FFT-accelerated homogenization scheme with arbitrary discretization developed by Leute et al. (2021) no closed form expression exists and to the best knowledge of the author, FD approximation is the most common method for computing the effective properties. FD approximation computes the effective properties by means of application of a set of suitable macroscopic perturbation strain fields. FD tangents are notoriously expensive to compute in terms of computational time, especially in case of nonlinear constitutive laws; therefore, working out a consistent tangent can contribute to homogenization speed-up.

In this chapter, I derive an algorithmically consistent macroscopic tangent, in the context of the strain-based (projection-based FFT accelerated) scheme, by means of minimizing the variation of strain energy of the micro-structure. The derived form of the consistent tangent complies with the expression introduced by Miehe et al. (1999) which gives a closed form expression for consistent tangent in a FEM context. However, the regularity of the discretization enables us to compute the effective tangent efficiently. The derived consistent tangent can compute the macroscopic tangent for the general case of geometrical and material non-linearity and is not limited to any specific application. It also is useful for this research since it helps fast and convenient quantifying of the ASR advancement.

6.1 Derivation

Let's assume that the equilibrium of a RVE with a certain micro-structure is solved under a certain load case, such as mean value of stress or strain as the boundary condition, and the values of the equilibrium elastic fields $\boldsymbol{\varepsilon}^{\text{eq}}(\boldsymbol{x})$ and $\boldsymbol{\sigma}^{\text{eq}}(\boldsymbol{x})$ is obtained. In addition, the

tangent stiffness field of the material points at equilibrium $\mathbb{C}(\mathbf{x})$ has been also evaluated in the equilibrium solution process.

In order to find the \mathbb{C}^{eff} of the RVE at its current state, let us perturb the system at equilibrium (strain field of $\boldsymbol{\varepsilon}^{\text{eq}}(\mathbf{x})$) with $\delta\bar{\boldsymbol{\varepsilon}}^{\text{pert}}$, which is applied as mean strain perturbation. In order to simplify the derivation, all the variables are assumed to be in Mandel (Voigt) Notation in small strain formulation. The potential energy variation increment along the path reads:

$$dU^{\text{pert}} = \int_V \overbrace{(d\boldsymbol{\varepsilon}(\mathbf{x}))^T \boldsymbol{\sigma}(x, \boldsymbol{\varepsilon}(\mathbf{x}), g(\mathbf{x}))}^{\text{equivalent to dot product}} dV, \quad (6.1)$$

where $\boldsymbol{\varepsilon}(\mathbf{x})$ and $g(\mathbf{x})$ are respectively the strain field and the state variables, while $d\boldsymbol{\varepsilon}(\mathbf{x})$ is the strain variation increment. The energy variation after accommodating the strain perturbation $\delta\bar{\boldsymbol{\varepsilon}}^{\text{pert}}$ is integral of (6.1) over the strain path ($\boldsymbol{\varepsilon}^{\text{eq}} \rightarrow \boldsymbol{\varepsilon}^{\text{eq}} + \delta\boldsymbol{\varepsilon}$) where $\delta\boldsymbol{\varepsilon}$ is the strain variation due to the perturbation. The energy variation can be formulated as:

$$\delta U^{\text{pert}} = \int_{\boldsymbol{\varepsilon}^{\text{eq}}}^{\boldsymbol{\varepsilon}^{\text{eq}} + \delta\boldsymbol{\varepsilon}} \int_V (d\boldsymbol{\varepsilon}(\mathbf{x}))^T \boldsymbol{\sigma}(x, \boldsymbol{\varepsilon}(\mathbf{x}), g(\mathbf{x})) dV, \quad (6.2)$$

where $\boldsymbol{\varepsilon}^{\text{eq}} + \delta\boldsymbol{\varepsilon}$ is the strain field of the perturbed cell after reaching the equilibrium. The strain field variation $\delta\boldsymbol{\varepsilon}$ can be divided into its mean value $\delta\bar{\boldsymbol{\varepsilon}}^{\text{pert}}$ and its periodic fluctuation contributions as:

$$\delta\boldsymbol{\varepsilon}(\mathbf{x}) = \delta\bar{\boldsymbol{\varepsilon}}^{\text{pert}} + \delta\tilde{\boldsymbol{\varepsilon}}(\mathbf{x}) \quad (6.3)$$

According to the linear assumption around the equilibrium point stress can be calculated by:

$$\boldsymbol{\sigma}(x, \boldsymbol{\varepsilon}(\mathbf{x}), g(\mathbf{x})) = \underbrace{\boldsymbol{\sigma}(x, \boldsymbol{\varepsilon}^{\text{eq}}(\mathbf{x}), g(\mathbf{x}))}_{\boldsymbol{\sigma}^{\text{eq}}} + \underbrace{\mathbb{C}(\mathbf{x})(\boldsymbol{\varepsilon}(\mathbf{x}) - \boldsymbol{\varepsilon}^{\text{eq}}(\mathbf{x}))}_{d\boldsymbol{\sigma}}. \quad (6.4)$$

Replacing (6.4) in (6.2) and reordering integrals gives:

$$\delta U^{\text{pert}} = \int_V \left[\int_{\boldsymbol{\varepsilon}^{\text{eq}}}^{\boldsymbol{\varepsilon}^{\text{eq}} + \delta\boldsymbol{\varepsilon}} (d\boldsymbol{\varepsilon}(\mathbf{x}))^T \boldsymbol{\sigma}^{\text{eq}} + (d\boldsymbol{\varepsilon}(\mathbf{x}))^T \mathbb{C}(\mathbf{x})(\boldsymbol{\varepsilon}(\mathbf{x}) - \boldsymbol{\varepsilon}^{\text{eq}}(\mathbf{x})) \right] dV. \quad (6.5)$$

Chapter 6. Algorithmically consistent tangent for the strain-based FFT-accelerated scheme

Taking integral considering that $\boldsymbol{\sigma}^{\text{eq}}$ is independent of $d\boldsymbol{\varepsilon}$ and applying its bounds yield:

$$\delta U^{\text{pert}} = \int_V \left[(\delta \boldsymbol{\varepsilon}(\mathbf{x}))^T \boldsymbol{\sigma}^{\text{eq}} + \frac{1}{2} (\delta \boldsymbol{\varepsilon}(\mathbf{x}))^T \mathbb{C} \delta \boldsymbol{\varepsilon}(\mathbf{x}) \right] dV. \quad (6.6)$$

We can replace $\delta \boldsymbol{\varepsilon}(\mathbf{x})$ in (6.6) according to (6.3) which gives:

$$\delta U^{\text{pert}} = \int_V \left[(\delta \bar{\boldsymbol{\varepsilon}}^{\text{pert}} + \delta \tilde{\boldsymbol{\varepsilon}}(\mathbf{x}))^T \left(\boldsymbol{\sigma}^{\text{eq}} + \frac{1}{2} \mathbb{C} (\delta \bar{\boldsymbol{\varepsilon}}^{\text{pert}} + \delta \tilde{\boldsymbol{\varepsilon}}(\mathbf{x})) \right) \right] dV. \quad (6.7)$$

With a suitable quadrature rule applied we can approximate this energy as:

$$\delta U^{\text{pert}} \approx \sum_Q \left(\delta \bar{\boldsymbol{\varepsilon}}^{\text{pert}} + \delta \tilde{\boldsymbol{\varepsilon}}(x^Q) \right)^T \left(\boldsymbol{\sigma}^{\text{eq}} + \frac{1}{2} \mathbb{C}(x^Q) (\delta \bar{\boldsymbol{\varepsilon}}^{\text{pert}} + \delta \tilde{\boldsymbol{\varepsilon}}(x^Q)) \right) w^Q \quad (6.8)$$

where w^Q represents the quadrature weights. Considering the fact that $\delta \tilde{\boldsymbol{\varepsilon}}$ is a compatible (periodic gradient) field and we can apply the projection operator \mathbf{G} on $\delta \tilde{\boldsymbol{\varepsilon}}$ in (6.8) which yields:

$$\delta U^{\text{pert}} = \left(\delta \bar{\boldsymbol{\varepsilon}}^{\text{pert}} + \mathbf{G} \delta \tilde{\boldsymbol{\varepsilon}} \right)^T \left(\mathbf{W} \boldsymbol{\sigma}^{\text{eq}} + \frac{1}{2} \mathbf{C}_w (\delta \bar{\boldsymbol{\varepsilon}}^{\text{pert}} + \mathbf{G} \delta \tilde{\boldsymbol{\varepsilon}}) \right) \quad (6.9)$$

In (6.9), \mathbf{W} is a diagonal matrix holding quadrature weights and $\mathbf{C}_w = \mathbf{W} \mathbf{C}$ is the weighted constitutive tangent matrix. expansion of (6.9) yields:

$$\begin{aligned} \delta U^{\text{pert}} &= \left(\delta \bar{\boldsymbol{\varepsilon}}^{\text{pert}} \right)^T \mathbf{W} \boldsymbol{\sigma}^{\text{eq}} + (\mathbf{G} \delta \tilde{\boldsymbol{\varepsilon}})^T \mathbf{W} \boldsymbol{\sigma}^{\text{eq}} \\ &\quad + \frac{1}{2} \left[\left(\delta \bar{\boldsymbol{\varepsilon}}^{\text{pert}} \right)^T \mathbf{C}_w \delta \bar{\boldsymbol{\varepsilon}}^{\text{pert}} + (\mathbf{G} \delta \tilde{\boldsymbol{\varepsilon}})^T \mathbf{C}_w \delta \bar{\boldsymbol{\varepsilon}}^{\text{pert}} \right] \\ &\quad + \frac{1}{2} \left[\left(\delta \bar{\boldsymbol{\varepsilon}}^{\text{pert}} \right)^T \mathbf{C}_w \mathbf{G} \delta \tilde{\boldsymbol{\varepsilon}} + (\mathbf{G} \delta \tilde{\boldsymbol{\varepsilon}})^T \mathbf{C}_w \mathbf{G} \delta \tilde{\boldsymbol{\varepsilon}} \right]. \end{aligned} \quad (6.10)$$

We need to minimize δU^{pert} with $\delta \tilde{\boldsymbol{\varepsilon}}(\mathbf{x})$ as the independent variable. As a result, we differentiate (6.10) with respect to $\delta \tilde{\boldsymbol{\varepsilon}}(\mathbf{x})$:

$$\frac{\partial (\delta U^{\text{pert}})}{\partial \delta \tilde{\boldsymbol{\varepsilon}}} = \mathbf{G}^T \mathbf{W} \boldsymbol{\sigma}^{\text{eq}} + \mathbf{G}^T \mathbf{C}_w \delta \bar{\boldsymbol{\varepsilon}}^{\text{pert}} + \mathbf{G}^T \mathbf{C}_w \mathbf{G} \delta \tilde{\boldsymbol{\varepsilon}}. \quad (6.11)$$

First, according to the self adjointness of the \mathbf{G} operator we can replace all \mathbf{G}^T s with \mathbf{G} and reorder the application of \mathbf{W} and \mathbf{G} because \mathbf{W} is diagonal. Likewise, we can

rewrite (6.11) as:

$$\frac{\partial (\delta U^{\text{pert}})}{\partial \delta \tilde{\boldsymbol{\varepsilon}}} = \mathbf{W}\mathbf{G}\boldsymbol{\sigma}^{\text{eq}} + \mathbf{G}\mathbf{C}_w\delta E^{\text{pert}} + \mathbf{G}\mathbf{C}_w\mathbf{G}\delta \tilde{\boldsymbol{\varepsilon}}. \quad (6.12)$$

According to the self adjointness of \mathbf{G} , the first term in the right hand side of (6.12) drops because $\boldsymbol{\sigma}^{\text{eq}}$ is actually obtained by equating $\mathbf{G}\boldsymbol{\sigma}$ to zero (the discretized equilibrium equation in the strain-based scheme). Therefore, (6.12) simplifies to:

$$\frac{\partial (\delta U^{\text{pert}})}{\partial \delta \tilde{\boldsymbol{\varepsilon}}} = \mathbf{G}\mathbf{C}_w\delta E^{\text{pert}} + \mathbf{G}\mathbf{C}_w\mathbf{G}\delta \tilde{\boldsymbol{\varepsilon}}. \quad (6.13)$$

Equating (6.13) to zero in order to obtain the minimum of δU^{pert} gives:

$$\mathbf{G}\mathbf{C}_w\delta \tilde{\boldsymbol{\varepsilon}} = -\mathbf{G}\mathbf{C}_w\delta \tilde{\boldsymbol{\varepsilon}}^{\text{pert}} \quad (6.14)$$

By solving (6.14) as a linear equation $\mathbf{A}\mathbf{x} = \mathbf{b}$ with:

$$\begin{aligned} \mathbf{A} &\equiv \mathbf{G}^T\mathbf{C}_w \\ \mathbf{b} &\equiv -\mathbf{G}^T\mathbf{C}_w\delta \tilde{\boldsymbol{\varepsilon}}^{\text{pert}}, \end{aligned}$$

(for instance using a CG solver) we can obtain values of the periodic fluctuation of the response to the perturbation around equilibrium $\delta \tilde{\boldsymbol{\varepsilon}}$, i.e. $\delta \tilde{\boldsymbol{\varepsilon}}$ becomes known. Afterwards, we can compute $\delta \boldsymbol{\varepsilon}$ according to (6.3). In a 2D RVE setup, the strain solution of (6.14) for the test macroscopic perturbation strains of:

$$\delta \tilde{\boldsymbol{\varepsilon}}^{\text{pert}}_{11} = \begin{bmatrix} 1 & 0 \\ 0 & 0 \end{bmatrix}, \quad \delta \tilde{\boldsymbol{\varepsilon}}^{\text{pert}}_{22} = \begin{bmatrix} 0 & 0 \\ 0 & 1 \end{bmatrix}, \quad \delta \tilde{\boldsymbol{\varepsilon}}^{\text{pert}}_{12} = \begin{bmatrix} 0 & \frac{1}{2} \\ \frac{1}{2} & 0 \end{bmatrix} \quad (6.15)$$

respectively yield $\delta \tilde{\boldsymbol{\varepsilon}}^{(11)}$, $\delta \tilde{\boldsymbol{\varepsilon}}^{(22)}$, and $\delta \tilde{\boldsymbol{\varepsilon}}^{(12)}$ which are second order tensor fields. collecting $\delta \tilde{\boldsymbol{\varepsilon}}^{(11)}$, $\delta \tilde{\boldsymbol{\varepsilon}}^{(22)}$, and $\delta \tilde{\boldsymbol{\varepsilon}}^{(12)}$ in a higher rank matrix yields a fourth rank tensor field called

Chapter 6. Algorithmically consistent tangent for the strain-based FFT-accelerated scheme

localization fourth order field \mathbb{A} defined as:

$$\mathbb{A}(\mathbf{x}) \equiv \begin{bmatrix} \delta\tilde{\boldsymbol{\varepsilon}}_{11}^{(11)}(\mathbf{x}) & \delta\tilde{\boldsymbol{\varepsilon}}_{11}^{(22)}(\mathbf{x}) & \delta\tilde{\boldsymbol{\varepsilon}}_{11}^{(12)}(\mathbf{x}) \\ \delta\tilde{\boldsymbol{\varepsilon}}_{22}^{(11)}(\mathbf{x}) & \delta\tilde{\boldsymbol{\varepsilon}}_{22}^{(22)}(\mathbf{x}) & \delta\tilde{\boldsymbol{\varepsilon}}_{22}^{(12)}(\mathbf{x}) \\ \delta\tilde{\boldsymbol{\varepsilon}}_{12}^{(11)}(\mathbf{x}) & \delta\tilde{\boldsymbol{\varepsilon}}_{12}^{(22)}(\mathbf{x}) & \delta\tilde{\boldsymbol{\varepsilon}}_{12}^{(12)}(\mathbf{x}) \end{bmatrix}. \quad (6.16)$$

Note that the fourth rank tensor \mathbb{A} can be directly constructed from the solution of (6.14) with perturbations defined in (6.15). According to the definition of the localization tensor \mathbb{A} , a fourth order compilation of the strain responses can be computed by a double contraction of \mathbb{A} and the fourth rank matrix $[\delta\tilde{\boldsymbol{\varepsilon}}]$:

$$[\delta\tilde{\boldsymbol{\varepsilon}}(\mathbf{x})] = \mathbb{A}(\mathbf{x}) : \underbrace{\begin{bmatrix} \delta\tilde{\boldsymbol{\varepsilon}}^{\text{pert}}_{11} \\ \delta\tilde{\boldsymbol{\varepsilon}}^{\text{pert}}_{22} \\ \delta\tilde{\boldsymbol{\varepsilon}}^{\text{pert}}_{12} \end{bmatrix}}_{[\delta\tilde{\boldsymbol{\varepsilon}}]}. \quad (6.17)$$

The matrix form of the linearized system then can be represented in form of:

$$[\delta\tilde{\boldsymbol{\sigma}}(\mathbf{x})] = \mathbb{C}(\mathbf{x}) [\delta\tilde{\boldsymbol{\varepsilon}}(\mathbf{x})] = \mathbb{C}(\mathbf{x})\mathbb{A}(\mathbf{x}) [\delta\tilde{\boldsymbol{\varepsilon}}] \quad (6.18)$$

The derivative of the stress fluctuation with respect to macroscopic strain averaged over the solution domain yields:

$$\left\langle \frac{\partial \tilde{\boldsymbol{\sigma}}}{\partial \tilde{\boldsymbol{\varepsilon}}} \right\rangle = \frac{1}{V} \int_{\Omega} \mathbb{C}(\mathbf{x})\mathbb{A}(\mathbf{x}) d\Omega. \quad (6.19)$$

According to the definition of the consistent effective tangent:

$$\mathbb{C}^{\text{eff}} \equiv \left\langle \frac{\partial \boldsymbol{\sigma}}{\partial \tilde{\boldsymbol{\varepsilon}}} \right\rangle = \frac{\partial \bar{\boldsymbol{\sigma}}}{\partial \tilde{\boldsymbol{\varepsilon}}} + \left\langle \frac{\partial \tilde{\boldsymbol{\sigma}}}{\partial \tilde{\boldsymbol{\varepsilon}}} \right\rangle. \quad (6.20)$$

The first term of the right hand side of (6.20) can be obtained according to (??) as:

$$\frac{\partial \bar{\boldsymbol{\sigma}}}{\partial \tilde{\boldsymbol{\varepsilon}}} = \frac{1}{V} \int_{\Omega} \mathbb{C}(\mathbf{x}) d\Omega. \quad (6.21)$$

As a result the effective consistent tangent can be obtained with the form of:

$$\mathbb{C}^{\text{eff}} = \frac{1}{V} \int_{\Omega} \mathbb{C}(\mathbf{x}) (\mathbb{A}(\mathbf{x}) + \mathbb{I}) d\Omega \quad (6.22)$$

By following the same quadrature rule used for solution of the problem one can obtain the effective tangent in the form of:

$$\mathbb{C}^{\text{eff}} = \frac{1}{N_P} \left(\sum_{N_P} \sum_{N_Q} \mathbb{C}_Q (\mathbb{A}_Q + \mathbb{I}) w_Q \right), \quad (6.23)$$

where \mathbb{I} is the fourth order Identity matrix, \mathbb{C}_Q is the elasticity matrix for the material associated with the quadrature point Q , and w_Q is the weight associated with the quadrature point. \mathbb{A}_Q is obtained from the local strain response of the system at quadrature point Q . N_P is the counter of the pixels at the RVE. It is also notable that it is not necessary to construct the \mathbb{A}_Q completely at once and it can be also calculated row by row by computing the response of (6.14) by applying each of the perturbation strains one at a time.

The developed algorithmically consistent tangent is preferable to FD approximation since the effective tangent calculated by this method depends on the solution of (6.14) which can be in principle solved up to machine accuracy in constant number of CG steps (solution complexity does not grow with system size). The FD test approach, on the other hand, depends both on the perturbation and the convergence of the Newton solver used to solve each test case. The appropriate perturbation size is actually problem-dependent and unknown. Furthermore, the linearity of (6.14) is advantageous specifically in nonlinear problems, where the FD method needs to iterate on nonlinear equations.

In comparison with the consistent tangent algorithm introduced by Göküzüm and Keip (2017), our derived consistent tangent is preferable, since directly solving for the strains and being able to apply the local tangent of the quadrature points on the calculated strain fluctuation makes it unnecessary to construct new intermediate variables and the rows of the effective stiffness tangent can be populated one at a time directly from the corresponding mean strain applied on the system. That makes our method memory efficient as well. In addition, our derivation, in contrast to the derivation presented

by Göküzüm and Keip (2017), is based on the potential energy minimization principle.

6.2 Examples and results

In order to examine the derived effective tangent calculated via the consistent tangent expression the following 4 examples are carried out. First, the algorithmically evaluated tangent is tested against the analytic tangent of a simple problem. In the second example, we compute the tangent of a RVE with periodic arrangement of cracks and compare it against semi-analytical stiffness loss calculations of Aboudi (1987). In the third and fourth examples, algorithmically obtained effective tangent is tested against FD approximation for two nonlinear problems. In the third example, the effect of variation of FD step size is studied and in the fourth example, the algorithmic tangent and the FD tangent approximation are compared in sense of the tangent evaluation error and the computational time needed for effective tangent computation.

6.2.1 Comparison with the analytical solution of Eshelby

The first example is the comparison of the obtained effective stiffness with the analytical solution of a micro-structure containing a dilute spherical stiff inclusion with inclusion volume ratio of $\rho^{\text{incl}} = 1.0\%$. This example is similar to one of the examples of Göküzüm and Keip (2017). Choosing a RVE with such a dilute inclusion volume ratio enables us to compare the algorithmically consistent effective tangent calculated by our developed method to the analytical value of the tangent that can be computed according to Eshelby inclusion solution Eshelby (1957) because the periodic duplicates of the inclusion that are far enough to not interact with each other. Therefore, we can assume that our periodic homogenization RVE can be taken equivalent to Eshelby inclusion problem in an infinite medium.

The closed form of the tangent for an Eshelby inclusion problem is briefly explained here for the sake of completeness. Two variables a and b as functions of the Poisson ratio of

the matrix material ν_{matr} are defined as:

$$a = \frac{1}{3} \frac{1 + \nu_{matr}}{1 - \nu_{matr}} \quad \text{and} \quad b = \frac{2}{15} \frac{4 - 5\nu_{matr}}{1 - \nu_{matr}}. \quad (6.24)$$

Variables a and b can be used in the definition of another pair of variables A and B which are respectively function of bulk modulus κ and the shear modulus μ of both phases:

$$A = \frac{\kappa^{incl} + \kappa^{matr}}{(\kappa^{matr} + \kappa^{incl}a - \kappa^{matr})} \quad \text{and} \quad B = \frac{\mu^{incl} + \mu^{matr}}{(\mu^{matr} + \mu^{incl}b - \mu^{matr})} \quad (6.25)$$

Based on (6.24) the effective bulk modulus and shear modulus renders as:

$$\kappa^{anal} = \frac{\kappa^{matr}}{1 + A\rho^{incl}} \quad \text{and} \quad \mu^{anal} = \frac{\mu^{matr}}{1 + B\rho^{incl}} \quad (6.26)$$

Accordingly, the analytical effective bulk modulus and shear modulus given the Lamé parameters of the matrix and inclusion phases as $\kappa^{incl} = 10\text{GPa}$, $\mu^{incl} = 5\text{GPa}$, and $\kappa^{matr} = 2\text{GPa}$, $\mu^{matr} = 1\text{GPa}$ are:

$$\mathbb{C}_{1111}^{anal} = 4.044\text{GPa} \quad \text{and} \quad \mathbb{C}_{1212}^{anal} = 1.017\text{GPa} \quad (6.27)$$

For the numerical computations of the stiffness (the algorithmic tangent), several RVEs with different number of pixels have been considered (from 31^3 to 259^3). The corresponding stiffness components \mathbb{C}_{1111}^{algo} and \mathbb{C}_{1212}^{algo} for considered discretization points are respectively depicted in Figure 6.1a, and b. The figure shows that the computed stiffness coefficients converge to the values:

$$\mathbb{C}_{1111}^{algo} = 4.037\text{GPa} \quad \text{and} \quad \mathbb{C}_{1212}^{algo} = 1.015\text{GPa} \quad (6.28)$$

with refining the discretization. The error of stiffness reduction is in order of 0.1% already for the RVE with 69^3 pixels and the value for the finest grid sizes that are slightly softer compared to analytically calculated stiffness (from Eshelby solution) is in agreement with findings of Göküzüm and Keip (2017) and Schneider et al. (2016b).

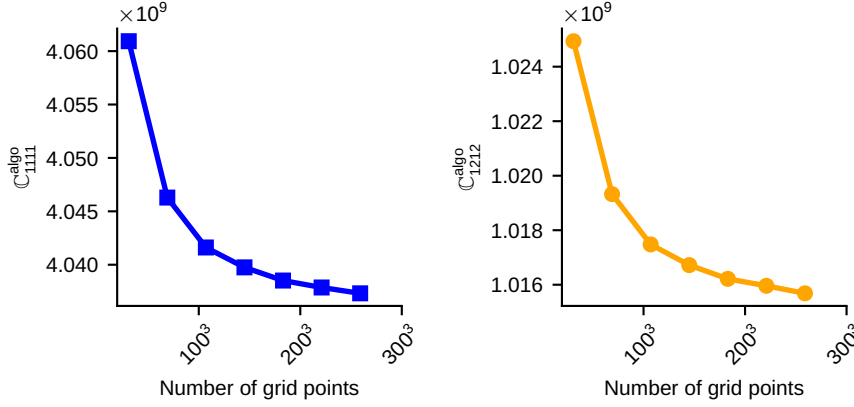


Figure 6.1: The algorithmic bulk and shear modulus of a RVE constaining a spherical inclusion with volume ratio of 1.0%

6.2.2 Stiffness reduction of cracked solids

Since we intend to use the developed tangent evaluation for computing the stiffness of an ASR damage model that contains cracks, it is crucial to examine stiffness computation with the developed method in presence of cracks. Accordingly, the second example for this chapter is the computation of the effective stiffness of a 2D linear elastic domain containing a doubly periodic rectangular array of cracks. The geometry of the considered RVE is depicted in Figure 6.2. The RVE considered is depicted in this figure by dark gray while the light gray shows the periodic replica of the solution domain. The crack located along the x-axis and at the center of the RVE with length of d_1 is colored as red. The distance of crack arrays in the direction of the cracks and perpendicular to crack axis are noted in the figure respectively as d_2 and $2L$.

The semi-analytical calculation of the stiffness reductions experiencing load cases of different fracture modes (Mode I, II, III) is carried out by Aboudi (1987), where the equilibrium equations in conjunction with the continuity conditions for the tractions and displacements are solved to obtain elastic field variables. Aboudi (1987) approximated the displacement fields with Legendre polynomials in terms of distance from the center line. The stiffness loss of the RVE for C_{2222}^{algo} and C_{1212}^{algo} can respectively be corresponded to the semi-analytical stiffness loss calculations of Aboudi (1987) under Mode I and Mode II load application.

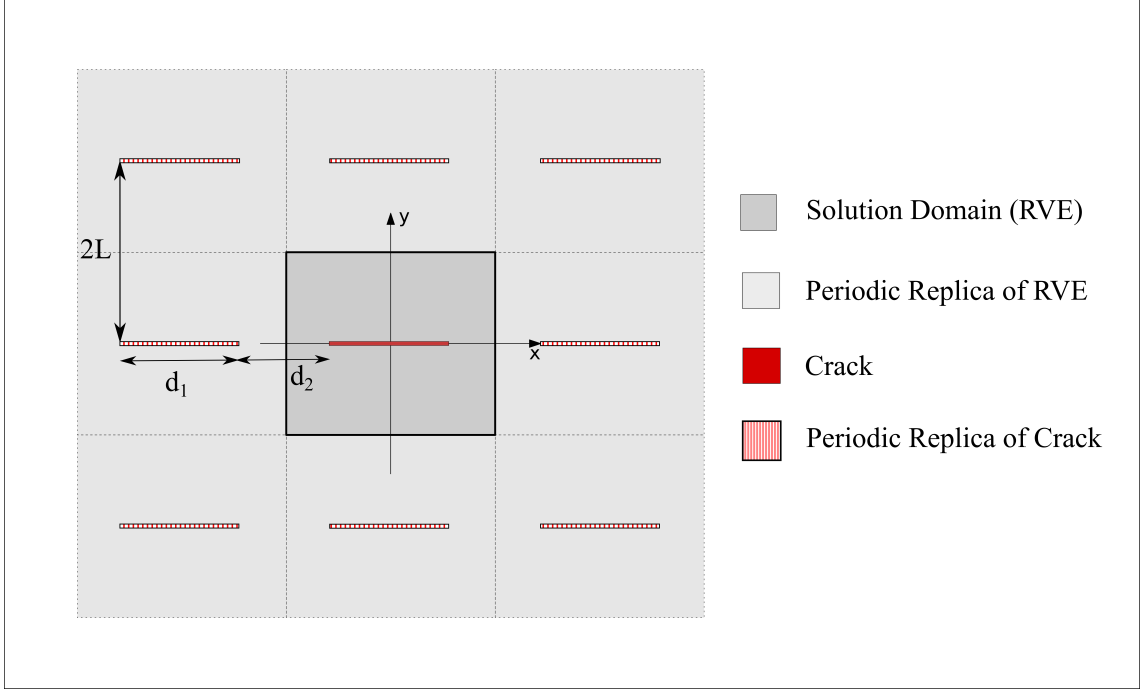


Figure 6.2: Geometry of the periodic 2D linear elastic material problem with horizontal crack and its neighboring periodic replica

The obtained relative stiffness reduction of the RVE schematically depicted in Figure 6.2 is shown in Figure 6.3. The x -axis of both plots is the ratio of the crack length (d_1) divided by the width of the RVE orthogonal to crack axis ($2L$). Each curve corresponds to a certain ratio of crack length divided by the length of the RVE in the direction of the cracks ($d_1 + d_2$).

Subfigure a shows the normalized stiffness of \mathbb{C}_{2222} (the normal stiffness in the direction orthogonal to the crack axis) normalized by \mathbb{C}_{2222}^0 which notes the normal stiffness in y direction with no crack. The solid curve in the figure corresponds to the semi-analytical relative stiffness loss (Aboudi (1987)) for Mode I. The algorithmic stiffness matches well with the semi-analytical calculation specifically for RVEs with low crack density, i.e. in cases with far-apart cracks (from their periodic replica) relative to their length. The normal stiffness results (loss of \mathbb{C}_{2222}) also have better match when their distance in x direction is higher (blue curves have better match compared to purple ones).

The subfigure b shows the normalized shear stiffness $\mathbb{C}_{1212}/\mathbb{C}_{1212}^0$. The algorithmic tangents and the semi-analytical effective tangent show good agreement also in case

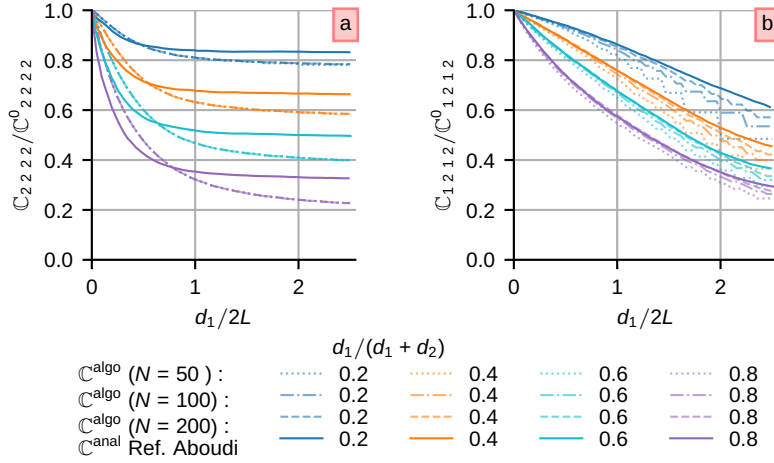


Figure 6.3: Stiffness reduction of the periodic 2D linear elastic material problem with horizontal crack

of shear stiffness. The values of algorithmic tangent and semi-analytical tangent show better match for lower crack density perpendicular to the cracks ($d_1/2L$) here as well. Generally speaking the algorithmic consistent tangent exhibits good performance for calculating the effective tangent of a RVE containing cracks.

6.2.3 Homogenization of a Hyper-elasto-plastic micro-structure

In order to study the performance of the algorithmic tangent calculation for RVEs containing nonlinear phases a RVE containing elasto-plastic material is taken as the next example. The example is adopted from de Geus et al. (2017) where the micro-structure of the RVE consists of hyperelasto-plastic material. The constitutive law and the configuration of the this example is identical to the example presented in Subsection 4.2.1.

The solution domain of the examples, discretized as 441×441 pixels with two quadrature points per pixel (domain is discretized with a regular periodic grid presented in column b of Figure 1.6), consists of two steel phases martensite and ferrite that are identical in their elastic regime; however, their initial yield stress and hardening coefficients differ

here by $\varphi = 2$ as the phase contrast between martensite and ferrite as:

$$\tau_{y0}^{\text{ferrite}} \times \varphi = \tau_{y0}^{\text{martensite}}, \quad (6.29)$$

$$H^{\text{ferrite}} \times \varphi = H^{\text{martensite}}, \quad (6.30)$$

The relative error of tangent obtained by the developed algorithm (\mathbb{C}^{algo}) with respect to the tangent obtained by FD (\mathbb{C}^{fd}):

$$\epsilon^{\mathbb{C}} = \frac{\|\mathbb{C}^{\text{fd}} - \mathbb{C}^{\text{algo}}\|}{\|\mathbb{C}^{\text{fd}}\|}, \quad (6.31)$$

is taken as the measure to quantify the comparison of the tangents.

The value of the tangent calculation error $\epsilon^{\mathbb{C}}$ is plotted for different values of the perturbation amplitude of the FD method in Figure 6.4. The tolerance of the CG solver is taken as $\eta^{\text{CG}} = 1 \times 10^{-12}$ and the tolerance of the newton solver is taken as $\eta^{\text{Newton}} = 1 \times 10^{-7}$. The relative difference of \mathbb{C}^{algo} and \mathbb{C}^{fd} are less than 0.1% for all the tested finite strain step sizes. The error reduces down to 10^{-7} as the step size is decreasing from large values but for very small step sizes the numerical error increases and the error rises with further decrease of the step size.

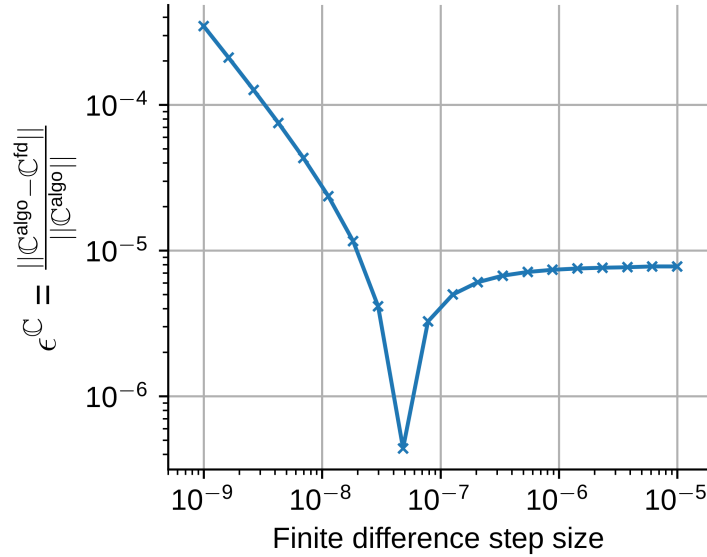


Figure 6.4: Relative error $\epsilon^{\mathbb{C}}$ of algorithmic tangent \mathbb{C}^{algo} with respect to the finite difference tangent \mathbb{C}^{fd}

6.2.4 Homogenization of an Neo-Hookean elastic RVE

One of the most important advantages of the developed closed form tangent in comparison to the conventional FD method is tangent evaluation speed gain. In order to quantify the tangent evaluation acceleration that the developed algorithm offers compared to FD last example of this chapter is homogenization of an RVE containing material with Neo-Hookean free-energy function in finite-strain formulation. Due to the non-linearity of the material and finite-strain formulation, FD tangent evaluation involves d^2 times nonlinear problem solution while the algorithmic tangent calculation just solves linear problems to obtain the effective tangent. The first Piola-Kirchhoff stress of the Neo-Hookean material is computed by:

$$\mathbf{P} = \mu \mathbf{F} - \mu (\det \mathbf{F})^{-\beta} \mathbf{F}^{-T} \quad (6.32)$$

where μ and β are material parameters.

The geometry of this example is so simple and contains a circular hard inclusion at the center of the RVE that has a Neo-Hookean constitutive laws and a soft matrix with linear elastic material. I solve the problem for different phase contrast between the matrix and the inclusion ($\frac{\mu_{matr}}{\mu_{incl}}$). I discretize the solution domain on 101×101 pixels and with a regular discretization presented in column b of Figure 1.6. The equilibrium is solved with $\eta^{\text{Newton}} = 1 \times 10^{-7}$ and $\eta^{\text{CG}} = 1 \times 10^{-12}$ as tolerances. The test step size for FD approximation is set as 1×10^{-6} .

The error of the tangent estimation is also quantified in this example with the same error as the previous example as noted in (6.31). The result of the tangent evaluation is presented in Figure 6.5. Subfigure 6.5a shows the relative tangent error ϵ^C which shows very good agreement of the algorithmic and the finite difference tangent for different phase contrasts. Having relative error in range of the solution tolerance approves that both tangent evaluation methods are successful in evaluating the tangent.

Figure 6.5b shows the time consumed for FD and algorithmic tangent evaluation. It depicts that for all of the phase contrast values the algorithmic tangent evaluation is faster. In addition, the FD tangent evaluation computation time grows more rapidly with phase contrast increase up to the point that for phase contrast of 64, the algorithmic

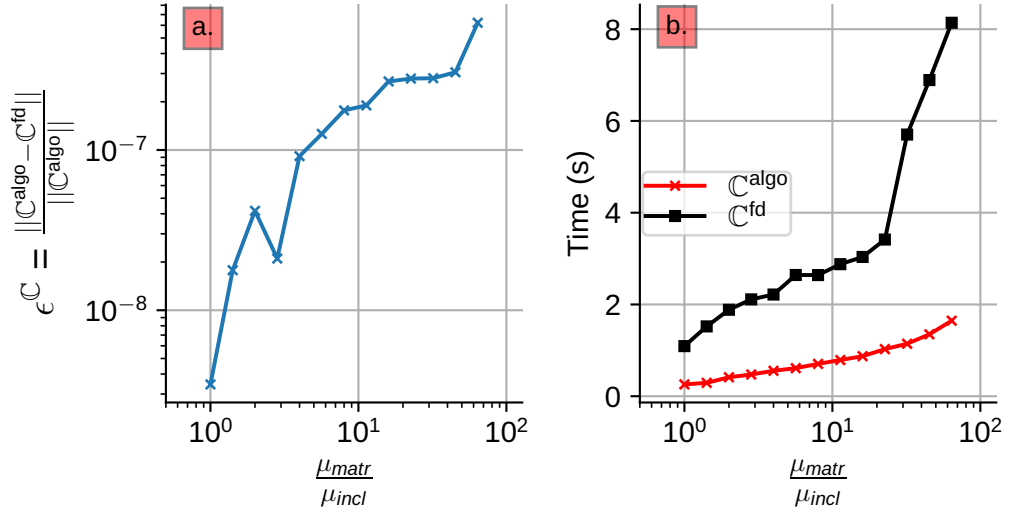


Figure 6.5: Relative error ϵ^C of algorithmic tangent \mathbb{C}^{algo} with respect to the finite difference tangent \mathbb{C}^{fd}

tangent evaluation is roughly 5 times faster. Tangent evaluation is slower with FD when phase contrast rises since the nonlinear solution of the perturbed RVE becomes computationally more expensive.

6.3 Conclusion

In this chapter, I have developed an algorithmically consistent tangent for the projection-based FFT-accelerated scheme based on the minimization of the incremental strain energy of the system. The developed consistent tangent algorithm involves solving a set of linear equations to achieve the mean stress of the perturbed RVE. Due to the linearity of the equations, they can be combined to make a single higher order linear equation. Whether to solve linear equations for a column of the effective tangent at a time, or for all of the components at once is a time and memory consumption matter. The former approach is less memory intensive but more time consuming, while the latter approach is more memory demanding and faster. I have opted for the first approach, since I wanted to use the same memory reserved for the equilibrium solution.

Evaluating the effective tangent using the developed method does not need any further material stress or tangent evaluation and merely uses those results obtained in solving

Chapter 6. Algorithmically consistent tangent for the strain-based FFT-accelerated scheme

for the equilibrium. This combined with the fact that the tangent evaluation in the developed method involves only linear equations makes the developed tangent evaluation method faster compared to FD tangent evaluation. This is empirically shown in the last example presented in this chapter. We will use the developed consistent tangent, later in Chapter 7 for evaluation of effective stiffness loss of a concrete micro-structure undergoing ASR damage.

7 Meso-scale Alkali-Silica reaction damage simulation

As set forth in Chapter 2, simulating ASR in a comprehensive damage model needs a fast, robust and reliable meso-scale model. The meso-scale and multi-scale models presented by Dunant and Scrivener (2012); Cuba Ramos (2017) could reproduce the crack pattern and the stiffness loss of ASR damage; however, the high computational costs of using a FE^2 and the constitutive laws employed in their work make their solution prohibitively expensive. The machinery we have prepared in this research can realize the speed-up needed and offers a fast and reliable meso-scale ASR damage model.

The specific geometrical characteristics (regular structure) of the RVEs simulated in meso-scale and multi-scale mechanical problems (cell problems) make the FFT-accelerated schemes a suitable candidate. The main drawback of the FFT-accelerated methods in the main part of the literature is the spurious oscillations introduced in the solution field that are catastrophic in case of damage mechanics. Both strain-based FFT-accelerated method with FE discretization (Leute et al. (2021)) and the displacement based preconditioned formulation (Ladecký et al. (2022b)) developed by the μ Spectre development team resolve ringing artifacts. I have actually showed the equivalence of these two schemes in Chapter 4 of this dissertation. Among these two formulations, we have opted for the strain-based scheme since in order to be able to compare results to literature it is necessary to have the possibility of imposing mean stress on the RVE (Lucarini and Segurado (2019a)).

Another challenge in the meso-scale ASR damage model is the non-convexity of the mechanics damage constitutive laws. The non-convex modified trust region solver introduced

in Chapter 5 can effectively and robustly handle this issue without need to explicitly assess the strain energy of the system. The modified trust region solver combined with the strain-based ringing-free FFT-accelerated scheme discussed in Chapter 1 and Chapter 4 of this dissertation make it possible to conduct the meso-scale ASR damage simulation significantly faster than convectional FEM solutions. In addition, by using the algorithmically consistent tangent presented in Chapter 6 we can also accelerate the evaluation of the effective tangent of the RVE compared to the FD tangent approximation, for the RVE containing material with nonlinear damage constitutive law.

In this chapter, first, I explain the micro-structure of the RVE and the method adopted to construct RVEs with high aggregate density. Next, I will discuss the asymmetric damage constitutive law used to model concrete phases (aggregate and cement paste). Afterwards, I explain the method used to apply different boundary conditions is briefly explained. Finally, the I present results of the meso-scale ASR damage problem.

7.1 RVE preparation

I, explicitly, resolve the cement paste and aggregate phases in the concrete micro-structure at the meso-scale ASR damage model. In addition, I induce the expansion of ASR products as expansion of randomly chosen elements that differ from the aforementioned phases (cement paste and aggregates). The expansion of these elements mimics the expansion of the ASR gel pockets residing inside them. The expansion of very small ASR gel pockets is assumed to be smeared inside the gel elements. This approach for modeling meso-scale ASR damage is successfully used by Cuba Ramos (2017) and Gallyamov et al. (2022).

One important step of computational homogenization is generating RVEs matching with available experimental data and RVE characteristics such as volume fraction of the phases, shape of the inclusions, and the size distribution of the inclusions inside the RVE, The RVE construction method should be capable of generateing RVE representative of real micro-structure and respecting the most important characteristics of the micro-structure. In case of the concrete micro-structure, the most important characteristics are:

1. High volume fraction: The RVE generation method should be able to insert non-intersecting inclusions with high compactness (up to 70%).
2. Inclusion size distribution: The method should also be capable of inserting inclusions with respect to the concrete aggregate size distribution.
3. Aggregate shapes: The RVE generation method needs to be able to insert arbitrary shaped inclusions (representing aggregates) inside a matrix (representing mortar). Polygons and polyhedra, respectively in 2D and 3D, are appropriate inclusion shapes to construct concrete RVEs since they can represent aggregates with sharp edges and corners.

The simplest possible method for generating RVEs composed of arbitrary arrangement of inclusions inside a matrix (concrete RVE) is random sequential addition (RSA). However, the time complexity of RVE construction grows exponentially with the targeted inclusion volume fraction (Widom (1966); He (2010)). Sonon et al. (2012) introduced, in their work, a modification of RSA in which by using level set (LS) approach, they could reduce the scaling of RVE construction complexity to linear with respect to the inclusion density. LS functions were originally introduced in computational methods to model propagation of wave fronts and later used for free surface flows (Carrica et al. (2006); Mean et al. (2020)).

The LS functions, in the RVE construction methods, are the distance of each point inside the RVE from the nearest inclusion. Sonon et al. (2012) has used these LS functions to determine the feasible set of points inside the RVE to insert a new inclusion with a certain size. This results in a significant reduction in the number of failed insertion trials compared to plain RSA. As a result, the time complexity of placing new aggregate becomes constant in time, as it merely involves random selection among feasible points to insert aggregate with a certain size).

Sonon et al. (2012) have used a pure geometrical approach for updating the LS functions. Updating LS functions in their approach is based on the fact that the distance of a point and a polyhedron (convex or not) is the minimum of distances from this point to all of the vertices, edges and faces of the polyhedron. Therefore, they ought to evaluate

the distance of each point from all of the vertices, edges, and faces of a newly inserted polyhedron to update the LS functions.

In contrast, in this research, I adopted a more efficient approach to calculate the LS function. The method used for calculating LS functions is inspired by the original purpose of defining the level set functions (wave propagation front solution). The method is based on the so-called fast marching method for solving an equivalent Eikonal equation (Sethian (1996); Chacon and Vladimirovsky (2012)). Using the fast marching method combined with the LS-RSA RVE generation scheme, enables us to make RVEs with packing densities up to 70% reasonably fast. In addition, the arbitrary shape of the inclusions enables us to construct a geometrically realistic representation of the concrete micro-structure. As an example, a 2D bi-phase of a RVE made by LS-RSA is presented in Figure 7.1.

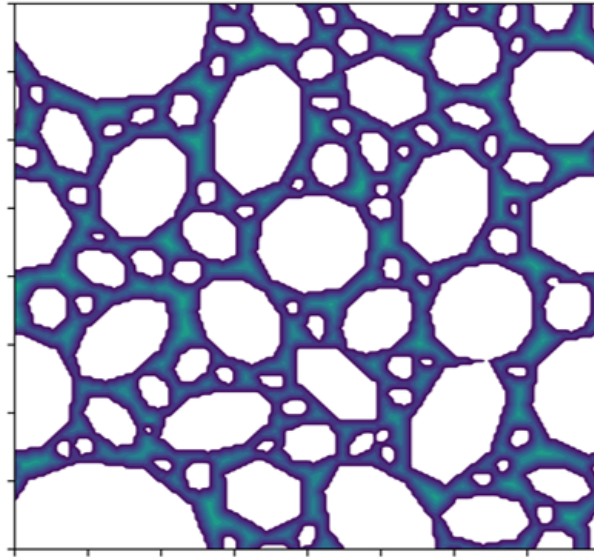


Figure 7.1: periodic concrete RVE constructed in 2D with packing density of 60% with polygon inclusions

7.2 Constitutive laws

Wide range of materials including geomaterials, wood, and concrete and their underlying phases fail due to the propagation and coalescing of micro-cracks. In structural analysis and computational homogenization, this phenomenon (called brittle damage) can be considered as strain softening behavior in constitutive laws. Kachanov (1958), in his

application of a continuum damage model, introduced the concept of strain softening through the definition of damage variable \mathbf{D} . Various continuum damage models, using damage variables with differences in the rank of the damage variable; scalar, vector (Krajcinovic and Fonseka (1981)), or a higher order tensor (Vakulenko and Kachanov (1971)); and even varying in other aspects (e.g. isotropic/directional, or tensile-compressive symmetric/asymmetric), have evolved since then.

The general form of the constitutive law of a linear elastic damage material has the form of:

$$\boldsymbol{\sigma} = \boldsymbol{\Lambda}(\mathbf{D}, \boldsymbol{\varepsilon}) : \boldsymbol{\varepsilon}. \quad (7.1)$$

In order to yield a positive definite damage release rate, in other words due to the irreversibility of the damage process, in continuum damage models, the evolution of \mathbf{D} needs to be non-negative ($\dot{\mathbf{D}} \geq \mathbf{0}$). Damage variable growth is governed by a yield surface of equation $f(\boldsymbol{\varepsilon}, \mathbf{D}, \kappa_0)$, in which κ_0 is the initial damage threshold (expressing the strength of the material). The damage variable evolves according to:

$$\dot{\mathbf{D}} = \begin{cases} 0 & \text{if } f < 0, \text{ or } f = 0, \dot{f} < 0 \text{ (i),} \\ \boldsymbol{\Phi}(\boldsymbol{\varepsilon}, \mathbf{D}) & \text{if } f = 0, \text{ and } \dot{f} = 0 \text{ (ii)} \end{cases} \quad (7.2)$$

where $\boldsymbol{\Phi}(\boldsymbol{\varepsilon}, \mathbf{D})$, called the damage evolution function, is a positive function of strain $\boldsymbol{\varepsilon}$, and the damage variable, \mathbf{D} . The equality $f = 0$ corresponds to the damage threshold surface of the material.

For $f < 0$, the strain state is within the damage surface, thus, there will be no damage and the damage variable does not grow. However, if $f \geq 0$ the damage increases. In the special case, where $\boldsymbol{\Phi}$ can be expressed as an explicit expression of a strain measure $\check{\boldsymbol{\varepsilon}} = \check{\boldsymbol{\varepsilon}}(\boldsymbol{\varepsilon})$, the damage variable \mathbf{D} can be also written explicitly as a function of $\check{\boldsymbol{\varepsilon}}$ and the stiffness reduction of the strain softening part of the constitutive law (7.1) also yields an explicit function of $\check{\boldsymbol{\varepsilon}}$ ($\boldsymbol{\Lambda} = \boldsymbol{\Lambda}(\check{\boldsymbol{\varepsilon}})$). Thus, stress can be evaluated according to

$$\boldsymbol{\sigma}(\boldsymbol{\varepsilon}) = \boldsymbol{\Lambda}(\check{\boldsymbol{\varepsilon}})\boldsymbol{\sigma}_0(\boldsymbol{\varepsilon}), \quad (7.3)$$

where $\boldsymbol{\sigma}_0$ is the pure elastic stress of the material. $\boldsymbol{\Phi}$ and $\boldsymbol{\Lambda}$ can be correlated according

to: $\Phi = \partial \Lambda / \partial \varepsilon$. Various expressions of f and Λ functions results in different damage models.

The damage model used in this research as the constitutive model of the aggregate and mortar phases of the concrete micro-structure is inspired by the damage material introduced by Mazars (1984). In the adopted damage model, a bilinear strain-stress behavior with a scalar damage variable D similar to Cuba Ramos (2017) was taken as the constitutive model. The damage surface f , proposed by Mazars and Pijaudier-Cabot (1989) with the form of:

$$f = \check{\varepsilon} - \kappa \quad (7.4)$$

has been used. In (7.4), $\check{\varepsilon}$ is a strain measure and κ is the softening parameter which takes the largest value of the equivalent strain measure $\check{\varepsilon}$ ever reached by the material and therefore is also a function of the strain.

The scalar damage variable D of the constitutive model can be expressed as:

$$D = \frac{\kappa_0 - \kappa}{\kappa}, \quad (7.5)$$

where κ_0 is the initial strain damage threshold (intact material). The function Λ from (7.3) can therefore be simply taken as:

$$\Lambda(\check{\varepsilon}) = 1 - D(\check{\varepsilon}). \quad (7.6)$$

We need to have a traction-compression asymmetric material behavior for the concrete phases in the ASR damage model since both aggregate and cement paste are brittle material and their tensile strength is relatively lower. In order to realize a tension-compression asymmetric material we need to break the strain into its tensile and compressive contributions and define $\check{\varepsilon}$ based on those components. To do so, we can isolate compressive and tensile parts of the strain after calculating the eigenvalues of the strain tensor (spectral decomposition). After breaking the strain into its tensile $(\varepsilon^{(t)})$ and compressive $(\varepsilon^{(c)})$ contributions according to:

$$\varepsilon_i^{(t)} = \mathcal{H}(\epsilon_i) \epsilon_i \mathbf{q}_i \otimes \mathbf{q}_i, \quad \varepsilon^{(c)} = \varepsilon - \varepsilon^{(t)}, \quad (7.7)$$

where ϵ_i is the i^{th} eigenvalue of the strain tensor, \mathbf{q}_i is its corresponding eigenvector, and \mathcal{H} is the Heaviside function. The operator \otimes denotes outer product. We take a strain measure $\check{\epsilon}$ formulated as the weighted sum of compressive and tensile strain components with the form of:

$$\check{\epsilon} = v^{(t)} \left\| \boldsymbol{\epsilon}^{(t)} \right\| + v^{(c)} \left\| \boldsymbol{\epsilon}^{(c)} \right\|, \quad (7.8)$$

where $v^{(t)}$ and $v^{(c)}$ are respectively weights of tensile and compressive contributions. Different values of $v^{(t)}$ and $v^{(c)}$ (material constants) introduce compression-tension asymmetry in the material damage behavior. For instance taking $v^{(c)}$ smaller than $v^{(t)}$ stretches the damage surface in the compression part and make it stronger (more resistant against getting damaged under compression) in case of compressive load scenarios and taking $v^{(c)} = 0$ suppresses compressive damage completely.

In our solution schemes (the strain-based and displacement-based FFT-accelerated schemes introduced in previous chapters), it is necessary to evaluate tangent stiffness of the material at discretization points. Therefore, in order to make them efficient, we need to derive the closed form of the tangent for the damage material. We, need to differentiate (7.3) with respect to $\boldsymbol{\epsilon}$ by taking $\mathbb{C}_0 \doteq \partial \boldsymbol{\sigma}_0 / \partial \boldsymbol{\epsilon}$ and replacing (7.5) in (7.3) before differentiation, the material tangent \mathbb{C} can be written as:

$$\mathbb{C} = (1 - D) \mathbb{C}_0 + \boldsymbol{\sigma}_0 \otimes \left(\frac{\partial D}{\partial \kappa} \frac{\partial \kappa}{\partial \boldsymbol{\epsilon}} \right). \quad (7.9)$$

In this equation, all of the terms are straight forward to calculate except $\partial \kappa / \partial \boldsymbol{\epsilon}$. This term is a tensor full of zeros for non damage steps (case (i) of (7.2)). However, in case of damage steps (case (ii) of (7.2)) it becomes:

$$\frac{\partial \kappa}{\partial \boldsymbol{\epsilon}} = \frac{\partial \check{\epsilon}}{\partial \boldsymbol{\epsilon}}, \quad (7.10)$$

which can be rewritten as:

$$\frac{\partial \kappa}{\partial \boldsymbol{\epsilon}} = v^{(t)} \frac{\partial \boldsymbol{\epsilon}^{(t)}}{\partial \boldsymbol{\epsilon}} + v^{(c)} \frac{\partial \boldsymbol{\epsilon}^{(c)}}{\partial \boldsymbol{\epsilon}}, \quad (7.11)$$

considering (7.8). According to the definition of $\boldsymbol{\epsilon}^{(t)}$ and $\boldsymbol{\epsilon}^{(c)}$ (7.7), evaluating $\partial \kappa / \partial \boldsymbol{\epsilon}$ needs differentiating eigenvalues and eigenvectors of the strain tensor with respect to the strain

tensor itself. The derivative of eigenvectors of a tensor with respect to the tensor itself has the closed form of

$$\frac{\partial q_{i,\gamma}}{\partial \epsilon_{\alpha\beta}} = \sum_{i \neq j} \frac{q_{i,\beta} q_{j,\alpha}}{\epsilon_i - \epsilon_j} q_{j,\gamma} \quad (7.12)$$

as given by Petersen et al. (2008). In (7.12), the Greek indices are expressing the index of the strain tensor and English ones are corresponding to the index of eigenvalues and their corresponding eigenvectors. For instance $q_{i,\gamma}$ denote the γ^{th} component of the i^{th} eigenvector.

The closed form of the eigenvector derivative given by (7.12) is prone to numerical instability due to the singularity. The singularity problem is evident in (7.12) and occurs when eigenvalues of the strain tensor tends to become equal. This situation arises often for the strain tensor and the most obvious situation is having a spherical strain state where the eigenvalues are equal to each other and makes the derivative of eigenvectors tend to infinity.

In order to resolve this problem, we have introduced a new tensile-compressive separation method that avoids singularity in differentiating the eigenvectors. To have a mathematically equivalent expression of the tensile and compressive strain contributions, we introduce the so-called tensile and compressive masking matrices defined as (inspired by work of Contrafatto and Cuomo (2007)):

$$\mathbf{M}^{(t)} = \sum_{i=1}^d \mathcal{H}(\epsilon_i) \mathbf{q}_i \otimes \mathbf{q}_i, \text{ and} \quad (7.13)$$

$$\mathbf{M}^{(c)} = \mathbf{I} - \mathbf{M}^{(t)}. \quad (7.14)$$

Using $\mathbf{M}^{(t)}$ and $\mathbf{M}^{(c)}$, the tensile and compressive contributions of the strain tensor can be defined as:

$$\boldsymbol{\epsilon}^{(t)} = \mathbf{M}^{(t)} \boldsymbol{\epsilon} \mathbf{M}^{(t)} \quad (7.15)$$

$$\boldsymbol{\epsilon}^{(c)} = \mathbf{M}^{(c)} \boldsymbol{\epsilon} \mathbf{M}^{(c)}. \quad (7.16)$$

Accordingly, their differentiation with respect to the strain tensor itself can be written as:

$$\frac{\partial \boldsymbol{\varepsilon}^{(t)}}{\partial \boldsymbol{\varepsilon}} = \frac{\partial \left(\mathbf{M}^{(t)} \boldsymbol{\varepsilon} \mathbf{M}^{(t)} \right)}{\partial \boldsymbol{\varepsilon}} = \frac{\partial \mathbf{M}^{(t)}}{\partial \boldsymbol{\varepsilon}} \boldsymbol{\varepsilon} \mathbf{M}^{(t)} + \mathbf{M}^{(t)} \frac{\partial \boldsymbol{\varepsilon}}{\partial \boldsymbol{\varepsilon}} \mathbf{M}^{(t)} + \mathbf{M}^{(t)} \boldsymbol{\varepsilon} \frac{\partial \mathbf{M}^{(t)}}{\partial \boldsymbol{\varepsilon}}, \text{ and} \quad (7.17)$$

$$\frac{\partial \boldsymbol{\varepsilon}^{(c)}}{\partial \boldsymbol{\varepsilon}} = \frac{\partial \left(\mathbf{M}^{(c)} \boldsymbol{\varepsilon} \mathbf{M}^{(c)} \right)}{\partial \boldsymbol{\varepsilon}} = \frac{\partial \mathbf{M}^{(c)}}{\partial \boldsymbol{\varepsilon}} \boldsymbol{\varepsilon} \mathbf{M}^{(c)} + \mathbf{M}^{(c)} \frac{\partial \boldsymbol{\varepsilon}}{\partial \boldsymbol{\varepsilon}} \mathbf{M}^{(c)} + \mathbf{M}^{(c)} \boldsymbol{\varepsilon} \frac{\partial \mathbf{M}^{(c)}}{\partial \boldsymbol{\varepsilon}}. \quad (7.18)$$

For carrying out the differentiation of $\partial \boldsymbol{\varepsilon}^{(t)} / \partial \boldsymbol{\varepsilon}$ and $\partial \boldsymbol{\varepsilon}^{(c)} / \partial \boldsymbol{\varepsilon}$ according to (7.17) we need to work out the differentiation of the masking matrices with respect to the strain tensor $\partial \mathbf{M}^{(t)} / \partial \boldsymbol{\varepsilon}$. According to (7.14), we can obtain $\partial \mathbf{M}^{(c)} / \partial \boldsymbol{\varepsilon}$ by:

$$\frac{\partial \mathbf{M}^{(c)}}{\partial \boldsymbol{\varepsilon}} = - \frac{\partial \mathbf{M}^{(t)}}{\partial \boldsymbol{\varepsilon}} \quad (7.19)$$

For sake of brevity, the derivation for a 2D problem is reported here. Extension to 3D can be also carried out following a similar procedure. In order to derive $\partial \mathbf{M}^{(t)} / \partial \boldsymbol{\varepsilon}$ and $\partial \mathbf{M}^{(c)} / \partial \boldsymbol{\varepsilon}$ let us assume that the eigenvalues (ϵ_1 and ϵ_2) are arranged in an ascending order ($\epsilon_2 \geq \epsilon_1$). Depending on the sign of the eigenvalues the following cases are possible:

1. $\epsilon_1 < 0$, and $\epsilon_2 > 0$:

According to (7.13) the tensile masking matrix can be written as:

$$\mathbf{M}^{(t)} = \mathbf{q}_2 \otimes \mathbf{q}_2. \quad (7.20)$$

As a result we can differentiate $\mathbf{M}^{(t)}$ w.r.t $\boldsymbol{\varepsilon}$ as:

$$\frac{\partial \mathbf{M}^{(t)}}{\partial \boldsymbol{\varepsilon}} = \frac{\partial \mathbf{q}_2}{\partial \boldsymbol{\varepsilon}} \otimes \mathbf{q}_2 + \mathbf{q}_2 \otimes \frac{\partial \mathbf{q}_2}{\partial \boldsymbol{\varepsilon}}. \quad (7.21)$$

Replacing the $\partial \mathbf{q}_2 / \partial \boldsymbol{\varepsilon}$ from (7.12) gives us:

$$\frac{\partial \mathbf{M}_{\alpha\beta}^{(t)}}{\partial \boldsymbol{\varepsilon}_{\theta\iota}} = \left[\frac{\mathbf{q}_{2,\iota} \mathbf{q}_{1,\theta}}{\epsilon_2 - \epsilon_1} \mathbf{q}_{1,\alpha} \right] \mathbf{q}_{2,\beta} + \mathbf{q}_{2,\alpha} \left[\frac{\mathbf{q}_{2,\iota} \mathbf{q}_{1,\theta}}{\epsilon_2 - \epsilon_1} \mathbf{q}_{1,\beta} \right] \quad (7.22)$$

which can be rewritten as:

$$\left(\frac{\partial \mathbf{M}^{(t)}}{\partial \boldsymbol{\varepsilon}} \right)_{\alpha\beta\theta\iota} = \frac{\mathbf{q}_{1,\alpha} \mathbf{q}_{2,\beta} \mathbf{q}_{1,\theta} \mathbf{q}_{2,\iota} + \mathbf{q}_{2,\alpha} \mathbf{q}_{1,\beta} \mathbf{q}_{1,\theta} \mathbf{q}_{2,\iota}}{\epsilon_2 - \epsilon_1}, \quad (7.23)$$

in index notation, which is equivalent to:

$$\frac{\partial \mathbf{M}^{(t)}}{\partial \boldsymbol{\varepsilon}} = \frac{\mathbf{q}_1 \otimes \mathbf{q}_2 \otimes \mathbf{q}_1 \otimes \mathbf{q}_2 + \mathbf{q}_2 \otimes \mathbf{q}_1 \otimes \mathbf{q}_1 \otimes \mathbf{q}_2}{\epsilon_2 - \epsilon_1}. \quad (7.24)$$

Having $\mathbf{M}^{(t)}$ and $\frac{\partial \mathbf{M}^{(t)}}{\partial \boldsymbol{\varepsilon}}$ calculated we compute $\frac{\partial \boldsymbol{\varepsilon}^{(t)}}{\partial \boldsymbol{\varepsilon}}$ using (7.17):

$$\left(\frac{\partial \boldsymbol{\varepsilon}^{(t)}}{\partial \boldsymbol{\varepsilon}} \right)_{\alpha\lambda\theta\iota} = \left(\frac{\partial \mathbf{M}^{(t)}}{\partial \boldsymbol{\varepsilon}} \right)_{\alpha\beta\theta\iota} \left(\boldsymbol{\varepsilon}_{\beta o} \mathbf{M}_{o\lambda}^{(t)} \right)_{\beta\lambda} + \mathbf{M}_{\alpha\theta}^{(t)} \mathbf{M}_{\iota\lambda}^{(t)} + \left(\mathbf{M}_{\alpha o}^{(t)} \boldsymbol{\varepsilon}_{o\lambda} \right)_{\alpha\gamma} \left(\frac{\partial \mathbf{M}^{(t)}}{\partial \boldsymbol{\varepsilon}} \right)_{\gamma\lambda\theta\iota}. \quad (7.25)$$

According to (7.14) and (7.19) we can calculate $\mathbf{M}^{(c)}$ and $\frac{\partial \mathbf{M}^{(c)}}{\partial \boldsymbol{\varepsilon}}$ easily. Having these two computed, the calculation of $\frac{\partial \boldsymbol{\varepsilon}^{(c)}}{\partial \boldsymbol{\varepsilon}}$ is similar to the calculation of $\frac{\partial \boldsymbol{\varepsilon}^{(t)}}{\partial \boldsymbol{\varepsilon}}$ expressed in (7.25).

2. $\epsilon_1 < 0$, and $\epsilon_2 < 0$, or $\epsilon_1 > 0$, and $\epsilon_2 > 0$:

All other cases are the ones in which all the eigenvalues are positive or all of them are negative. In such cases, all eigenvalues are positive $\mathbf{M}^{(t)} = \mathbf{I}$, $\mathbf{M}^{(c)} = \mathbf{0}$ and if all of the eigenvalues are negative, the masking matrices are constant and simply given by: $\mathbf{M}^{(t)} = \mathbf{0}$, $\mathbf{M}^{(c)} = \mathbf{I}$.

Either way, the value of $\mathbf{M}^{(t)}$ and $\mathbf{M}^{(c)}$ does not change as $\boldsymbol{\varepsilon}$ varies infinitesimally; therefore, we can take:

$$\frac{\partial \mathbf{M}^{(t)}}{\partial \boldsymbol{\varepsilon}} = \frac{\partial \mathbf{M}^{(c)}}{\partial \boldsymbol{\varepsilon}} = \mathbf{0}. \quad (7.26)$$

Therefore, for $\mathbb{C}^{(t)}$ and $\mathbb{C}^{(c)}$ can be obtained (based on (7.25)) according to:

$$\frac{\partial \boldsymbol{\varepsilon}^{(t)}}{\partial \boldsymbol{\varepsilon}} = \mathbf{M}^{(t)} \underline{\otimes} \mathbf{M}^{(t)T} \quad (7.27)$$

$$\frac{\partial \boldsymbol{\varepsilon}^{(c)}}{\partial \boldsymbol{\varepsilon}} = \mathbf{M}^{(c)} \underline{\otimes} \mathbf{M}^{(c)T} \quad (7.28)$$

3. special case:

The case that both of eigenvalues are zero and can cause a singularity even with eigenvalues with different signs. However, such cases do not cause issue as they cannot be associated with a damage situation, since such load state, certainly, does

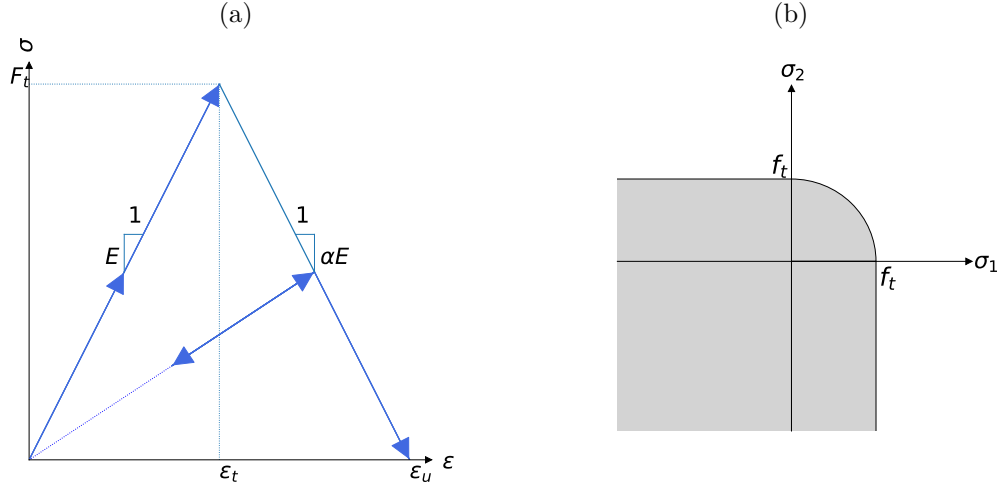


Figure 7.2: Constitutive law of the damage material in ASR damage example, a. stress-strain response of the damage material and b. Failure criterion of the damage material

not cross the damage surface and therefore the material behaves purely elastic.

We take both phases to be merely damaging in tensile loads since the driving damage mechanism in ASR damage is cracking (failure under tension) rather than crushing (failure under compression). We have basically adopted $v^{(t)} = 1$ and $v^{(c)} = 0$ in (7.8) to realize a constitutive law of the material that gets damaged merely in the tensile regime. The constitutive behavior of both aggregate and mortar phases is schematically shown in Figure 7.2 for a 2D material, where Figure 7.2a depicts the strain-stress behavior and Figure 7.2b illustrates the damage surface.

Following the aforementioned process makes it possible to compute the tangent stiffness of the tensile-compressive asymmetric material at the quadrature points of the discretization without any singularity problem.

Using continuum damage models in discretized models leads to so called crack band or cohesive band damage models (Berton and Bolander (2006); Hoover and Bažant (2014)). In these models, instead of lumping all the inelastic effects of a damage into a crack surface (discontinuity in extended-FEM (Belytschko and Black (1999); Moes et al. (1999); Sukumar et al. (2000))), the inelastic effects of crack is smeared across the width of a band of a finite thickness H . The corresponding normal strain in the solution is equivalent to $\epsilon = \llbracket u \rrbracket / H$, where $\llbracket u \rrbracket$ is the equivalent displacement jump between two faces of a crack.

In discretized models, the smallest possible band able to realize the crack is governed by the discretization size ($H \approx l_c$ where l_c is the discretization characteristic length). Therefore, the rate of damage energy release scales proportionally to the discretization characteristic size if the energy release volumetric density remains constant.

On the other hand, the mode-I fracture energy per unit area of the crack G_f (the mode happening in the ASR damage) is a constant and measurable material constant and needs to be preserved in modeling fracture and the constitutive law should be adjusted to realize G_f . The constitutive law can be correlated to the fracture energy via the variable $g_f \equiv G_f/l_c$ reflecting the dissipation energy per unit volume of the damage localization. g_f can be computed from the constitutive law according to:

$$g_f = \int_0^\infty \sigma(\varepsilon) d\varepsilon. \quad (7.29)$$

In other words, g_f is the area under the stress-strain curve. Without adjusting the constitutive law, the material response would be pathological and mesh-dependent.

A simple and effective remedy to avoid this pathological mesh-dependence of the material response is the adjustment of the softening part of the stress-strain law as a function of the element size. It is notable that such treatment is based on the assumption that the dissipation takes place in band of one element thick (Colombo and Comi (2019)). The modification of post-peak material parameters should realize equal energy dissipation per unit area of the crack for different discretization sizes. In other words, it should make energy dissipation per unit area invariant with respect to mesh size.

Taking the crack band localized at a band with the width of one element allows us to attribute the characteristic length l_c to the discretization size. For instance, in 2D, l_c can be taken as:

$$l_c = \sqrt{2A_{el}}, \quad (7.30)$$

where A_{el} is the area of the discretization elements evaluated numerically (Rizzi (1991)). However, it should also be noted that modification of strain-softening parameters such as material strength f_t or the ultimate strain ε_u can also affect the damage initiation and evolution. For instance, changing the value of the strength affects the damage initiation,

while manipulating the ultimate strain affects the crack opening at its fully damaged state. ASR damage modeling necessitates a realistic damage initiation; therefore, we need to take this into account when choosing a proper regularization. Further details on the regularization is presented later in the discretization study where the mesh refinement along with regularization are used to ensure the mesh independence of the simulation results.

7.3 Stress control in spectral methods

In this section, I present a modified projection operator in the context of the strain-based FFT-accelerated formulation, which enables us to impose the mean stress to the RVE. The approach is based on the modification of the projection operator introduced by Lucarini and Segurado (2019a). Lucarini and Segurado (2019a)'s idea is, here, applied in the context of the extended projection operator introduced by Leute et al. (2021). The projection operator presented in its generic format is based on the Helmholtz decomposition where an arbitrary field \mathbf{T} can be divided to its curl-free $\mathbf{T}_{||}$, gradient-free \mathbf{T}_{\perp} and mean contributions $\overline{\mathbf{T}}$ as:

$$\mathbf{T} = \mathbf{T}_{\perp} + \mathbf{T}_{||} + \overline{\mathbf{T}}. \quad (7.31)$$

The application of the projection operator yields the curl-free contribution of the field. In the Fourier space, application of the projection operator is a contraction:

$$\hat{\mathbf{T}}_{||} = \hat{\mathbb{G}} : \hat{\mathbf{T}}. \quad (7.32)$$

Leute et al. (2021) derived the operator $\hat{\mathbb{G}}$ for both small and finite strain formulation from the discrete gradient operator \mathcal{D} in a basis set of choice. Considering that the introduced projection operator \mathbb{G} , similar to FG, is meant to only keep the gradient contribution by killing the mean and the curl contributions of the field, the case of the zero wave-vector ($\mathbf{k} = \mathbf{0}$) is taken as a special case and the associated $\mathbb{G}(\mathbf{k})$ is taken to be zero. This projection operator makes it possible to find the fluctuation of the

strain field by solving the equilibrium for a given mean strain field $\bar{\varepsilon}$. In this research, in order to reproduce the boundary condition equivalent to the load scenario of the experimental ASR setups in the literature (Ben Haha (2006)), namely free expansion and uni-axial or bi-axial tension, it is necessary to be able to control the mean value of stress of the RVE.

Similar to Lucarini and Segurado (2019a), let us denote the alternative projection operator needed to enforce the mean value of the stress as \mathbb{G}^* . \mathbb{G}^* , unlike the original projection operator \mathbb{G} , should maintain the mean value of the field instead of suppressing it; therefore, the zero-mean condition is eliminated for \mathbb{G}^* . However, when applied to the stress fluctuation (with zero mean), its influence is identical to the application of the original projection. As a result, the equilibrium equation has the form of:

$$\mathbb{G}(\tilde{\boldsymbol{\sigma}}) = \mathbb{G}(\boldsymbol{\sigma} - \bar{\boldsymbol{\sigma}}) = \mathbf{0} \quad (7.33)$$

as derived in Lucarini and Segurado (2019a). Solving (7.33) gives the value of the full strain field, $\boldsymbol{\varepsilon}$ including both fluctuations and the mean value of the field:

$$\text{Find } \boldsymbol{\varepsilon} \mid \hat{\mathbb{G}}^* : \hat{\boldsymbol{\sigma}}(\boldsymbol{\varepsilon}) = \hat{\mathbb{G}}^* : \hat{\bar{\boldsymbol{\sigma}}}, \text{ for a given } \bar{\boldsymbol{\sigma}}. \quad (7.34)$$

The modified projection operator is identical to the original projection operator for all non-zero frequencies. For null-frequency in small strain, \mathbb{G}^* returns the symmetrized average of the input field. This can be achieved by taking the null-frequency component of the projection operator obtained in a FEM discretization with arbitrary elements inside a voxel as:

$$\hat{\mathbb{G}}_{\Theta\Lambda,ijkl}^*(\mathbf{0}) = \frac{1}{2} (\delta_{ik}\delta_{jl} + \delta_{il}\delta_{jk}), \quad (7.35)$$

in the small strain formulation. In (7.35), the capital Greek letters (Θ and Δ) denote quadrature points inside a voxel. similar to the notation of Leute et al. (2021). while the Latin letters are the tensor components. The zero frequency of the projection operator was set to the symmetrizing fourth-rank identity tensor for all of the elements of projection operator¹. Therefore, in the implementation of the $\hat{\mathbb{G}}^*$, it is only necessary to change the zero frequency component of the projection operator considering the type of boundary

¹Sufficient in this case since only discretizations with one nodal point per voxel were considered

condition needed to be imposed on the RVE.

The convergence criterion of the Newton solver of the strain-based scheme with mean strain as the imposed boundary condition is based on the evaluation of the norm of the solution step in the strain space normalized with respect to the size of the imposed change of the mean strain of the RVE. Since the change in the mean strain is unknown in the case of applying mean stress on the RVE we need to take another termination criterion. The replacement termination taken here is the L_∞ norm of the scalar field of norm of strain increment tensors at nodal points. In other words, the solution terminates as soon as the maximum of the norm of the strain field increment get smaller than η_{Newton} .

7.4 Simulation and results

In this section, I present ASR damage simulations as the use case of all of the machinery presented in this dissertation. The model I adopt for the meso-scale ASR damage modeling consists of the cement paste and aggregates as two explicit phases. I employ the strain-based FFT-accelerated solution scheme with FE discretization. The crack band damage model introduces a non-convex potential energy functional as the damage part of this constitutive law leads to a SNPSD system matrix. As a result, I use the modified trust region solver explained in Chapter 5.

In order to be able to compare our results with available ASR damage meso-scale simulation results of Cuba Ramos (2017), 2D meso-scale ASR damage model RVEs are considered here. In order to have same boundary conditions to Cuba Ramos (2017) we imposed mean stress value as the boundary condition of the RVE by means of modifying the projection operator as explained in Section 7.3 and according to findings of Lucarini and Segurado (2019a). Aggregates are placed inside a cement paste matrix in RVEs according to the Fuller size distribution (MotahariTabari and Shooshpasha (2018)) using the LS-RSA method explained in Section 7.1. Pixels considered to be containing growing ASR gel pockets have been randomly inserted inside aggregates. The structure of the 2D micro-structure is depicted in Figure 7.3a.

The constitutive laws of both aggregate and cement paste phases are bilinear crack

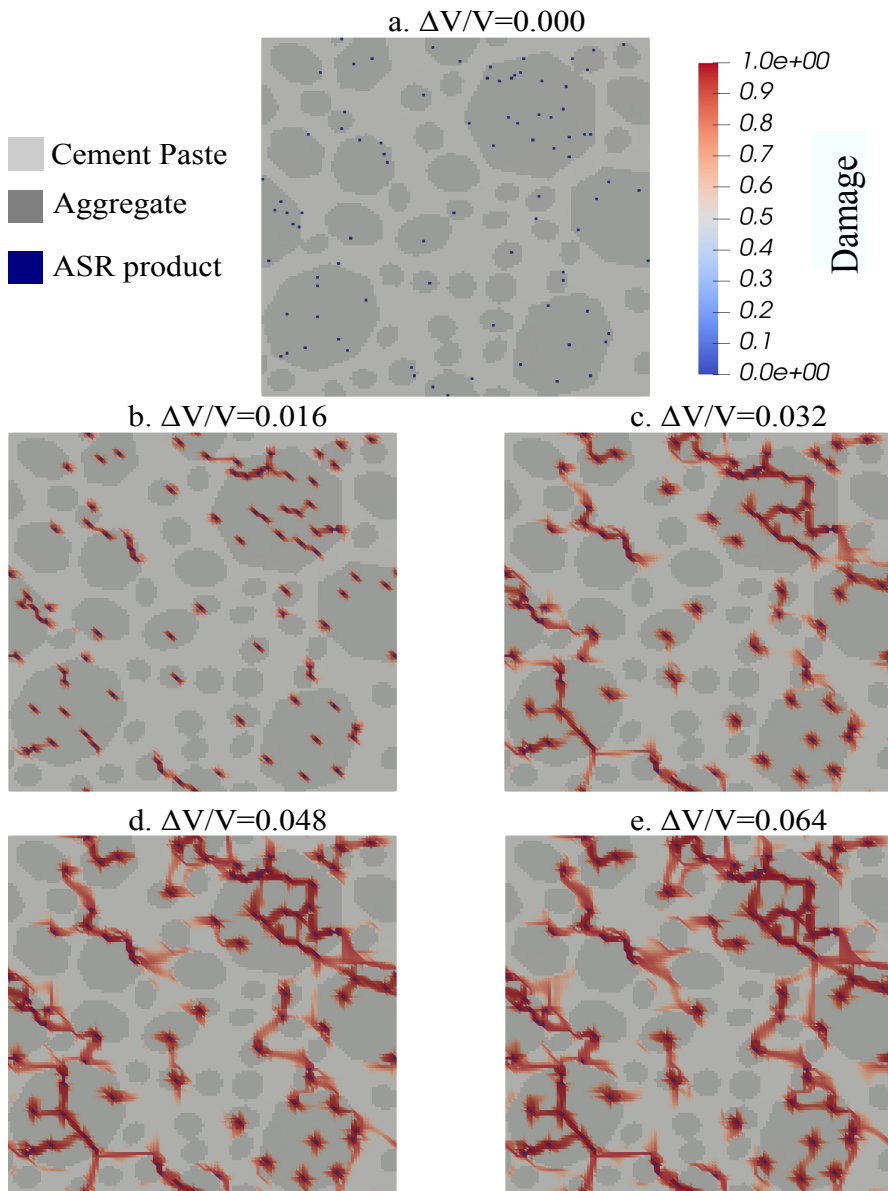


Figure 7.3: Evolution of crack pattern in the concrete micro-structure as a result of application of eigen-strain at ASR product sites shown as dark blue dots in the subfigure a. subfigures from a to e are arranged in a chronological sense and show snapshots of crack evolution inside the micro-structure as a function of increasing eigen-strain.

Table 7.1: Material properties of the non-convex damage example obtained from Gallyamov et al. (2020) for characteristic size $l_c = 5 \times 10^{-4}m$

	E [GPa]	μ [GPa]	ν	G_f [J/m ²]	f_t^0 [MPa]
Aggregates	59	22.6	0.3	160	10
Cement paste	12	4.6	0.3	60	3
ASR product	11	4.7	0.18	-	-

band damage with an isotropic damage measure (Mazars and Pijaudier-Cabot (1989)). Further details of the damage constitutive law is presented in Section 7.2. As discussed in Section 7.2, the damage material only fails under tensile loads (cracking under mode I). The parameters of the constitutive law, listed in Table 7.1 are obtained from work of Gallyamov et al. (2020).

I model the expansion of the ASR product sites by applying eigenstrain on the pixels containing them similar to Dunant (2009); Giorla et al. (2015); Cuba Ramos (2017); Gallyamov et al. (2020). Growing eigenstrain is added to the strain associated to these quadrature points before their constitutive law evaluation. These specific pixels are modeled as a linear elastic phase and assumed to contain the growing ASR gel pockets inside them. Line 28 of the Algorithm 4 is where eigenstrain is actually applied on the system. The mean value of stress is imposed as a boundary condition to be zero (free expansion) for the RVE. Imposing mean stress value as the boundary condition is implemented by means of modifying the projection operator following the idea of Lucarini and Segurado (2019a) explained in 7.3. This choice of boundary condition allows us to compare the results to similar results in the literature (Cuba Ramos (2017); Gallyamov et al. (2020)).

Crack pattern advancement inside a sample RVE of physical size of $0.1m \times 0.1m$ is depicted in Figure 7.3. As shown in Figure 7.3b, the damage initiation sites are adjacent to the growing gel pixel sites in the RVE. The advancement of the cracks caused by ASR damage is depicted in Figure 7.3c-e. These subfigures illustrate the crack coalescence process as the ASR expansion proceeds. Crack coalescence depends on the distance between the gel pocket and the aggregate boundary as well as the distance to other gel pockets. Crack coalescence occurs earlier at crack sites near the boundary of the

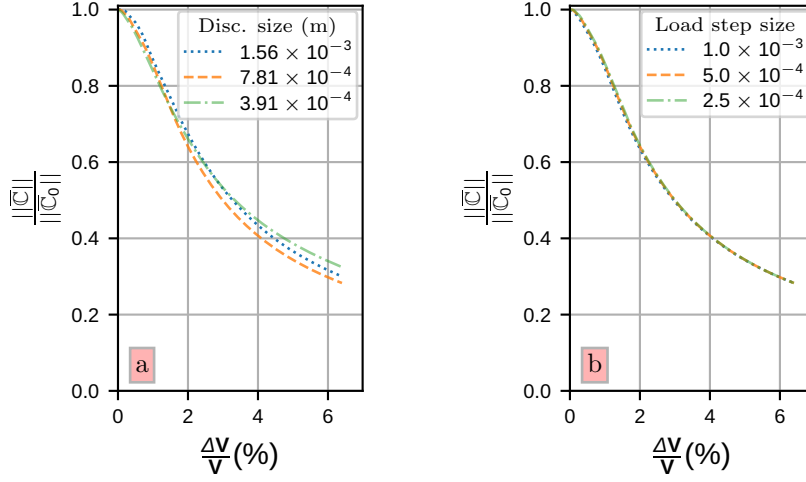


Figure 7.4: Discretization (mesh size) and load step study of the stiffness deterioration of 2D ASR damage simulation expressed as the ratio of the norm of the effective stiffness $\|\bar{C}\|$ tensor during ASR advancement divided by the norm of the effective stiffness tensor of the intact RVE $\|\bar{C}_0\|$. in subfigure a) the stiffness reduction of the same problem with fine ($h_f = 3.91 \times 10^{-4}m$), medium ($h_m = 2h_f$), and coarse ($h_c = 4h_f$) grid carried out with the medium load step size ($\Delta\varepsilon_m^{\text{eig}} = 5.0 \times 10^{-4}$) is plotted. In subfigure b) the stiffness reduction of the same problem with Load step study with small ($\Delta\varepsilon_s^{\text{eig}} = 2.50 \times 10^{-4}$), medium ($\Delta\varepsilon_m^{\text{eig}} = 2\Delta\varepsilon_s^{\text{eig}}$) and large load step of ($\Delta\varepsilon_l^{\text{eig}} = 4\Delta\varepsilon_s^{\text{eig}}$) carried out on h_m . is plotted.

aggregates or other gel pockets.

I conducted the discretization study and the load step study on a RVE with free expansion and growing gel pixels. In order to be able to realize nominally equivalent load scenarios we need to maintain the volume expansion induced. It necessitates variation of the applied eigenstrain by variation of the discretization size. Accordingly, we have kept the area expansion of the pixels containing ASR gel pockets constant by scaling the eigenstrain of the pixels containing ASR product. In other words, the eigenstrain induced is inversely proportional to the area of the pixels in the RVE.

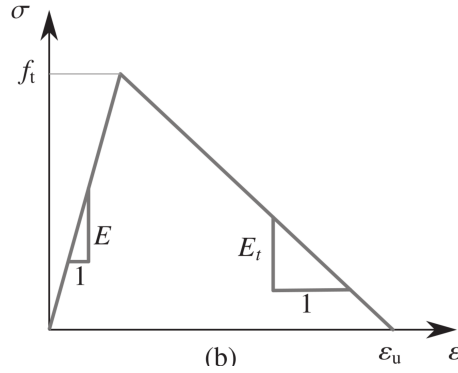


Figure 7.5: Schematic stress-strain response of a bilinear strain-softening damage constitutive law

In addition, we need to regularize the constitutive behavior, since the crack-band damage models yield pathological mesh dependent results without regularization as noted in Section 7.2. For a material with a bilinear stain-softening damage law (schematically depicted in Figure 7.5) the crack energy dissipation density (G_f) according to Equation 7.29 can be formulated as:

$$G_f = \underbrace{\left(\frac{f_t \epsilon_u}{2} \right)}_{g_f} l_c. \quad (7.36)$$

In order to maintain the value of G_f as a material constant by variation of l_c we need to scale either f_t or ϵ_u as strain-softening parameters to regularize the constitutive law.

In the ASR meso-scale model, in this research, nominally equivalent load cases have higher induced eigenstrain for smaller discretization sizes; and therefore the stress level induced in the pixels under the influence of the ASR gel expansion are also higher for RVEs with smaller pixels. So we need higher value for the strength, if we want the

crack to initiate at the same nominal load (area expansion) of the gel pixels. Accordingly, in the adopted regularization scheme, I take the ε_u constant and scale f_t inversely with l_c of the discretization. This choice of parameter regularization is vital to make the results mesh independent since it compensates the higher stress levels induced in the nominally equivalent RVEs for different pixel sizes. In other words, regulating f_t realizes equivalent damage (crack) initiation in equivalent ASR damage RVEs with different discretization sizes. It should also be noted that the material parameters presented in Table 7.1 correspond to the l_c of $5.00 \times 10^{-4}m$ as noted by Gallyamov et al. (2020) and they need to be regularized for the employed discretization size.

In order to quantify the advancement of ASR I evaluate the effective stiffness reduction of the RVEs experiencing ASR expansion. I use the algorithmically consistent tangent evaluation presented in Chapter 6 to evaluate the effective stiffness and then normalize it with the effective stiffness of the intact RVE. The RVE for conducting the discretization study and load step study are the RVE depicted in Figure 7.3a.

The results of the discretization size as well as load step size study are presented in Figure 7.4. The stiffness reduction of the RVE subjected to similar area expansion of gel pocket pixels is depicted in Figure 7.4a correspond to 3 different discretization sizes (fine ($h_f = 3.91 \times 10^{-4}m$), medium ($h_m = 2h_f$), and coarse ($h_c = 4h_f$) grids). The stiffness reduction with the advancement of the ASR process shows that the results are not mesh dependent. In addition, the stiffness reduction of a RVE with discretization size of h_m and three different load step sizes ($\Delta\varepsilon_s^{\text{eig}} = 2.50 \times 10^{-4}$), medium ($\Delta\varepsilon_m^{\text{eig}} = 2\Delta\varepsilon_s^{\text{eig}}$) large load step of ($\Delta\varepsilon_1^{\text{eig}} = 4\Delta\varepsilon_s^{\text{eig}}$) are shown in Figure 7.4a which suggests that the load step size is taken sufficiently small that the results are invariant with respect to load step size.

According to the results of the discretization study I have chosen the medium grid size and a load step size of 5.00×10^{-4} (the medium value of the considered load steps) to conduct the simulations with different randomly generated micro-structures presented in the following of the chapter whose results are depicted in Figure 7.6. I, then, subjected 100 randomly generated concrete 2D micro-structures to ASR expansion (imposed as eigenstrain in pixels containing gel pockets) under free expansion boundary condition.

The shaded blue area in Figure 7.6a shows the distribution of the stiffness loss of these micro-structure vs imposed volumetric expansion of the gel pixels. The mean of the distribution is also plotted as solid blue line. The stiffness loss of 3 representative micro-structures are plotted in Figure 7.6a and the Figure 7.6b-d are their corresponding final crack pattern.

In addition, the results obtained by Cuba Ramos (2017) modeling ASR damage in a similar configuration though using a FEM scheme and using a different approach for addressing the numerical instabilities due to the non-convexity of the problem (namely SLA) is also plotted in Figure 7.6a labeled as Ref which depicts reasonable agreement with our obtained results. By using our modified trust region solver in the strain-based scheme with FE discretization, our solution is much faster than their approach. According to correspondence with the authors of Cuba Ramos (2017); Gallyamov et al. (2020) their calculations on 28 cores take roughly 48 hours while our simulations, on average, take half an hour on 16 cores on the same machine (Fidis cluster at Ecole Polytechnique Fédérale de Lausanne (EPFL)) which shows significant improvement on a 2D ASR damage simulation, more than 2 order of magnitudes of speed-up.

The small differences, visible in Figure 7.6 is probably due to subtle differences between the models, namely we have used rectangular elements containing ASR gel pockets while they were triangular in their model. The aggregates in their model are assumed to have circular geometry while they were ellipsoidal in our model. The differences in the application of the boundary conditions can also be source of difference between the models as they have traction free boundary conditions while we have applied zero mean stress on our RVE. However, despite of all this subtle differences our obtained stiffness loss is in a good agreement with their results.

In addition, I carried out ASR meso scale damage simulations under uni-axial compression. The compression is applied through imposing the yy component of the mean stress direction $\bar{\sigma}_{22}$. The stiffness reduction of the RVE under uni-axial compression with different stress values is presented in Figure 7.7. Solid lines exhibit C_{1111}/C_{1111}^0 which is the normalized $C_{1111} = \partial\sigma_{11}/\partial\epsilon_{11}$ component of the tangent, while the dashed lines depict C_{2222}/C_{2222}^0 which is the normalized $C_{2222} = \partial\sigma_{22}/\partial\epsilon_{22}$ component of the tangent. As

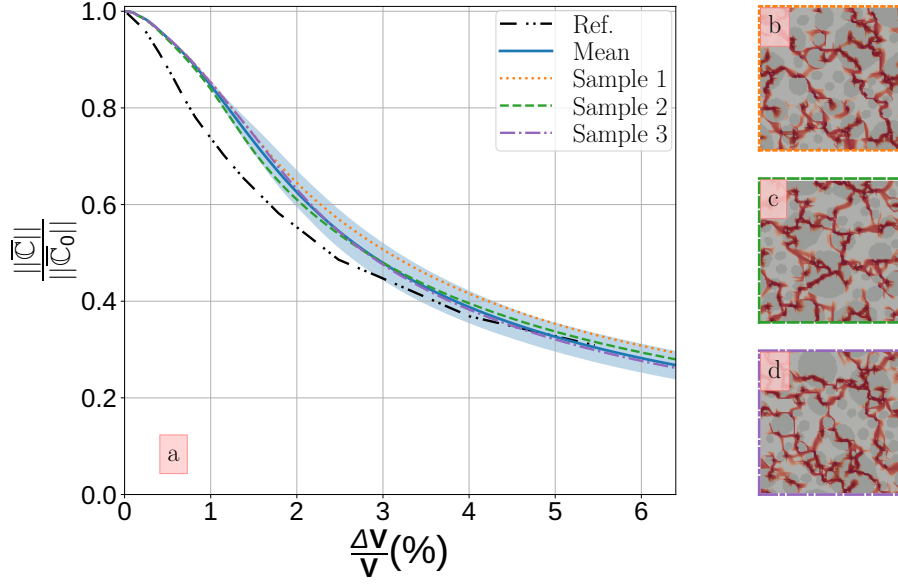


Figure 7.6: Stiffness reduction of sample micro-structures are shown in subfigure a). The light blue area is the area shaped between the maximum and minimum stiffness reduction of 100 samples. The solid blue line is the mean value of the stiffness reduction and the other 3 lines are the results corresponding to three representative micro-structures. Subfigures b. to d. show the final crack pattern developed in the micro-structure corresponding to the three samples (sample 1, 2 , and 3) noted in the subfigure a.

depicted, the stiffness reduction of the micro structures changes differently for different tangent components by variation of the imposed mean stress such that the C_{1111} tends to experience more stiffness reduction for higher compression stress imposed in the yy direction. The reduction of C_{2222} is less affected by the variation of the imposed mean stress $\bar{\sigma}_{22}$. It experiences slightly lower damage by increasing the mean stress but for the highest mean stress as the C_{1111} get substantially reduced (C_{1111} reduces to 20% of its initial value), the C_{2222} also experience higher reduction.

Opting for FE discretization and basis functions not only enables us to eliminate the ringing artifact, but also makes it possible for us to choose different FE elements. This can be specifically advantageous in simulating continuum damage, since the damage localization bands can be biased by the mesh orientation. i.e, in finite element solutions, the localization band tends to follow certain preferred directions dictated by the mesh, such as edges and diagonals (Belytschko et al. (1988); Sluys (1997)). This artifact is specifically pronounced when regular discretization is employed. Consequently, if the

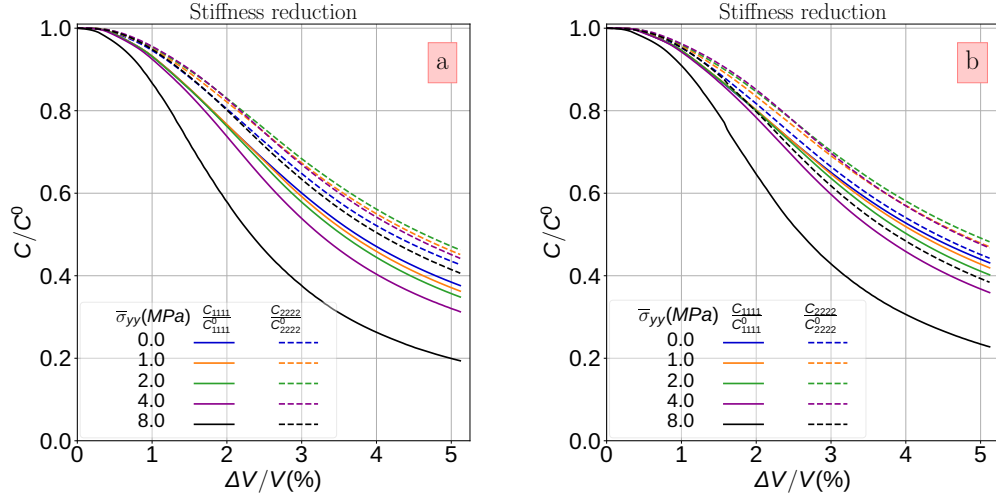


Figure 7.7: Stiffness reductions of two 2D concrete micro-structures under uniaxial compression ($\bar{\sigma}_{22}$) experiencing ASR induced expansion. Each of the subfigures correspond to a micro-structure.

crack band is not aligned with a layer of elements, a zig-zag band forms and the thickness of the crack band alters, which can introduce a mesh dependent crack band. Freedom in choosing FE discretization allows using a more isotropic discretization that reduces this kind of mesh dependence in the solution.

In order to illustrate this effect, I have modeled a 2D concrete micro-structure undergoing ASR damage simulation using 4 different element types. The crack pattern developed in the micro-structure using different FE discretizations is depicted in Figure 7.8. Firstly, it is notable that the bilinear element with 1 quadrature point was not successful in eliminating the ringing artifact and therefore the checker-board damage pattern is visible in Figure 7.8a. The presence of ringing artifact despite using FE discretization is due to the hourglass mode that occurs using the bilinear quadrangle elements with 1 quadrature point. Figure 7.8b shows that the vertical and horizontal directions are the preferred localization directions in a rectangular grided mesh. The bisector of the second quadrant (\nwarrow), and the horizontal and vertical directions afterwards, are the preferred localization bands for the triangular linear elements with right angle triangles (discretization shown in column b of Figure 1.6). As a result, the cracks with direction that are far from these preferred directions cannot localize in a single band of elements and make zig-zag crack band. This makes the first quadrant (\nearrow) the least favorable crack

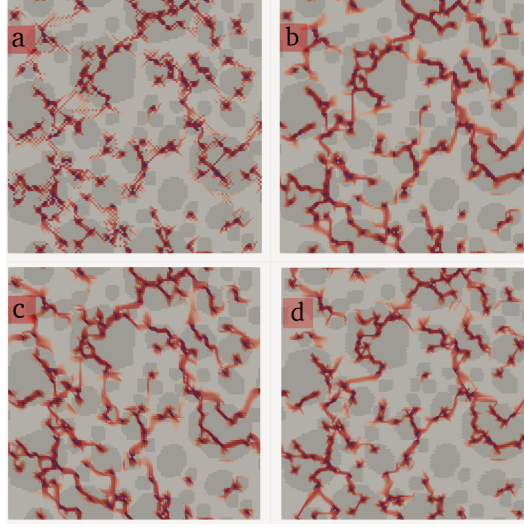


Figure 7.8: Crack pattern of a 2D ASR damage simulation with 4 different finite elements: **a.** Rectangular bilinear elements with 1 quadrature point, **b.** Rectangular bilinear elements with 4 quadrature point (corresponding to column **a** of Figure 1.6), **c.** Triangular linear elements with right angle triangles (corresponding to column **b** of Figure 1.6) , **d.** Triangular linear elements with equilateral triangles (corresponding to column **c** of Figure 1.6)

direction and therefore cracks close to the bisector of the first quadrant cannot localize in single-pixel band and also less cracks occur in this direction in the resulting crack pattern of the model. Figure 7.8b shows the crack pattern corresponding to triangular linear elements with equilateral triangles (the corresponding discretization is depicted in column c in Figure 1.6). It corresponds to the most isotropic element type that we used. Because in this discretization, the 3 preferred directions are more uniformly distributed in the angular coordinate (30° , 150° , and 270° with respect to x -axis), a crack band has a better chance of aligning with one of them and localize in a single element band. The flexibility that using arbitrary regular FE discretization offers allow us opt for the appropriate discretization for different use cases while enjoying the speed up offered by the FFT-accelerated solver.

7.5 Conclusion

In this chapter, I have reported how I constructed concrete micro-structure with high inclusion packing density. I have also worked out the tangent of a traction-compression

asymmetric damage constitutive law devoid of singularity issue. I also explained how mean stress boundary condition can be applied in the strain-based scheme with FE discretization. Afterwards, I presented the result of simulating ASR damage in a periodic RVE. It is also notable that the using the developed model in a homogenization application necessitates specific considerations to establish a rigorous coupling between the scales(Geers et al. (2010); Gitman et al. (2008)).

The results are in good agreement with the results obtained by Cuba Ramos (2017). In addition, I examined how the variation of the applied mean stress can affect the effective outcome of the ASR damage and showed that the concrete micro-structure tend to experience less stiffness reduction in the directions with higher compressive load. Finally I showed, how the FE discretization enables us to choose the desirable discretization for solving ASR damage homogenization problem. The solution method I used is roughly 200 times faster than the solution of the same problem with conventional FEM. Therefore, our solution method, capable of handling non-convex problems, has a great potential to be used as a fast and robust internal solver for multi-scale ASR damage simulation. However, it should be also noted that similar to the results of Cuba Ramos (2017) the developed model and solution scheme in this dissertation overestimates the loss of the loss of the effective tangent due to ASR damage compared to experimental results (Ben Haha (2006)). This discrepancy are most probably rooted in overlooking visco-elasticity in the constitutive law of the constituent phases, specifically the cement paste. This over-brittle response may also be explained by the 2d representation of ASR-affected concrete and the fact that ASR cracks contribute to the overall load-bearing capacity.

8 Conclusion

8.1 Summary and conclusions

This thesis focused on investigating the mechanical consequences of ASR in concrete at meso-scale by means of FFT-accelerated solution schemes. The key objective was to make FFT-based solvers capable of modeling damage mechanics problems and specifically ASR damage. To achieve this, we resolved the main issues with the existing FFT-based schemes. With my ringing-free non-convex FFT-based solution scheme, I was able to model ASR damage roughly 200 times faster than existing models.

The methods and schemes developed in this project have been implemented in a parallel open-source FFT-based solver library, μ Spectre, which can be used to solve a wide range of problems from solid mechanics to heat transfer. With the developed package, large sets of simulations could be executed quickly and efficiently utilizing EPFL's clusters to model ASR damage at meso-scale. μ Spectre's implementation supports both strain-based and displacement-based schemes explained in this dissertation. On top of efficient convex CG solvers, the modified trust region solver explained in Chapter 5 is also available in μ Spectre and can be used for generic RVEs containing materials with non-convex energy functional. μ Spectre comes with a Python user interface that makes its use convenient for end-users.

Two sub-pixel homogenization methods have been developed and used in this thesis. Both approaches have been explained in details in finite-strain formulation. Through

examples, it has been shown that they can mitigate the ringing issue; however, they cannot eliminate the ringing artifacts. Therefore, modeling ASR with them is not appropriate. Instead, the FFT-accelerated methods using FEM discretization was taken as the fast solution schemes capable of eliminating ringing artifacts and was used in the rest of the thesis.

Two mathematically equivalent schemes namely, strain-based (the projection-based FFT accelerated with FEM discretization) and displacement-based (FFT-accelerated preconditioned FEM), as ringing-free FFT-based solution schemes were investigated more thoroughly and their generalized equivalence (even with arbitrary admissible reference material) was shown in this dissertation. I demonstrated the identity of strain-based and displacement-method scheme both in terms of mathematical formulation and their performance in solving a nonlinear homogenization problem.

Modern FFT-accelerated solvers typically solve elliptic PDEs, i.e. those whose discretized form is equivalent to solving a convex optimization problem. However, some problems including damage mechanics are non-elliptic and their equivalent energy functional is non-convex. By introducing a modified trust region solver, I extended use of FFT-accelerated solvers to non-convex problems. I demonstrated the performance of the solver by simulating a strongly non-elliptic localizing damage mechanics problem in Chapter 7.

In addition, I developed an algorithmically consistent tangent based on the minimization of the potential energy of the simulation RVE. It enables us to compute the effective tangent of simulation RVEs efficiently and without any extra memory footprint. I have also shown that our algorithmically consistent tangent is faster than the FD effective tangent evaluation for nonlinear problems and can be used without the step size study that is required in the finite difference approximation approach.

I have used the tools and methods developed and implemented in this project to carry out ASR damage modeling in concrete. I have also worked out a formulation to compute the tangent of tension-compression asymmetric damage law devoid of singularity that enables robust use of FFT-based schemes for simulating micro-structures containing damage materials. The stiffness reduction of the micro-structure, as a quantitative measure of ASR advancement has been evaluated for concrete micro-structures undergoing ASR

expansion for free expansion and uni-axial loading scenarios. The results obtained are in agreement with the results obtained in the literature using similar constitutive laws. I have also shown that by altering the used FE discretization, it is possible to minimize the mesh-dependence of crack band damage modeling. As a result, we can conclude that the developed machinery has a great potential to serve as the fast and reliable core solver for a multi-scale ASR damage modeling.

8.2 Perspectives

As mentioned in Chapter 7, extending the simulations to 3D models is one possible improvement that might be helpful to make the resulting stiffness loss match with the corresponding experimental results. The computation time of a RVE discretized as 128^2 voxels is 0.5 hour on 16 cores. Considering that the solution methods developed and discussed in this dissertation scale with $\mathcal{O}(n \log n)$, a proper 3D ASR RVE with 128^3 pixels is expected to roughly take 1.5 days (36 hours) on 28 cores of a node on Fidis high-performance computing (HPC) cluster at EPFL. Therefore, we expect the developed ringing-free non-convex solution method to serve as a robust RVE solver for a multi-scale real-world ASR damage modeling.

Another important aspects of the developed meso-scale ASR damage model that has room and probably requires improvement is complying and improving the constitutive laws of the underlying phases of the concrete micro-structure in order to be able to achieve results matching with the experimental findings. One possible modification would be defining a crack closure constitutive law as proposed by Gallyamov et al. (2020) such that the parts of the already damaged areas of the micro-structure can experience stiffness recovery as they are unloaded due to approaching the stress field of another crack. One other possible improvement would be considering visco-elasticity in the constitutive law that will definitely reduce the stiffness reduction of a RVE undergoing ASR damage process.

The introduction of FAIEF allows using modern quasi-Newton solvers such as LBFGS. It would be interesting to find out how this quasi-Newton solver family can handle the non-convex damage mechanics homogenization problems. Therefore, implementing

and using quasi-Newton solvers is also another field to explore in modeling non-convex problems such as damage mechanics and specifically ASR damage problems.

In this dissertation, a robust and fast solution model for meso-scale ASR damage modeling was developed by resolving the drawbacks of FFT-accelerated scheme hindering them from simulating exotic mechanical problems such as damage mechanics. All the required machinery was implemented in an efficient, parallel, and open-source C++ library named μ Spectre as a generic homogenization solver capable of being adopted as the RVE solver for a wide range of problems. In order to realize a comprehensive ASR model, it is required to adopt the developed library (μ Spectre) as the core solver of a FEM solver to be capable to conduct a multi-scale ASR damage modeling and be able to enjoy the obtained speed-up in a comprehensive model of ASR damage. By doing so, the weak coupling assumption of macro- and meso-scale can be tested and validated. In addition, a wide range of parametric studies will also become possible with reasonable computational costs. This will help make a better understanding the phenomenon and its driving parameters.

Bibliography

- Aboudi, J. (1987). Stiffness reduction of cracked solids. *Engineering Fracture Mechanics*, 26(5):637–650.
- Bažant, Z. P. (1976). Instability, ductility, and size effect in strain-softening concrete. *Journal of the Engineering Mechanics Division*, 102(2):331–344.
- Belytschko, T. and Black, T. (1999). Elastic crack growth in finite elements with minimal remeshing. *International Journal for Numerical Methods in Engineering*, 45(5):601–620.
- Belytschko, T., Fish, J., and Engelmann, B. E. (1988). A finite element with embedded localization zones. *Computer Methods in Applied Mechanics and Engineering*, 70(1):59–89.
- Belytschko, T., Liu, W. K., Moran, B., and Elkhodary, K. I. (2014). *Nonlinear Finite Elements for Continua and Structures*. Wiley.
- Ben Haha, M. (2006). *Mechanical effects of alkali silica reaction in concrete studied by SEM-image analysis*. PhD thesis, EPFL.
- Bercovier, M. and Rosenthal, A. (1986). Using the conjugate gradient method with preconditioning for solving FEM approximations of elasticity problems. *Engineering computations*.
- Bernstein, G. (2007). Cork boolean library.
- Berton, S. and Bolander, J. E. (2006). Crack band model of fracture in irregular lattices. *Computer Methods in Applied Mechanics and Engineering*, 195(52):7172–7181.
- Bhattacharya, K. (2003). *Microstructure of martensite: why it forms and how it gives rise to the shape-memory effect*, volume 2. Oxford University Press.
- Boyd, J. P. (2000). *Chebyshev and Fourier Spectral Methods*. Dover Publications, New York.

Bibliography

- Brisard, S. and Dormieux, L. (2012). Combining Galerkin approximation techniques with the principle of Hashin and Shtrikman to derive a new FFT-based numerical method for the homogenization of composites. *Comput. Method. Appl. M.*, 217-220:197–212.
- Budiansky, B. (1965). On the elastic moduli of some heterogeneous materials. *Journal of the Mechanics and Physics of Solids*, 13(4):223–227.
- Carrica, P. M., Wilson, R. V., and Stern, F. (2006). An unsteady single-phase level set method for viscous free surface flows. *International Journal for Numerical Methods in Fluids*, 53(2):229–256.
- Chacon, A. and Vladimirovsky, A. (2012). Fast two-scale methods for eikonal equations. *SIAM Journal on Scientific Computing*, 34(2):A547–A578.
- Charière, R., Marano, A., and Gélébart, L. (2020). Use of composite voxels in FFT based elastic simulations of hollow glass microspheres/polypropylene composites. *International Journal of Solids and Structures*, 182-183:1–14.
- Charlwood and Scrivener (2011). *Expanding concrete in dams—long term challenges*. CRC Press Taylor & Francis Group Boca Raton FL. USA.
- Charlwood, R., Solymar, S., and Curtis, D. (1992). A review of alkali aggregate reactions in hydroelectric plants and dams. In *Proceedings of the international conference of alkali-aggregate reactions in hydroelectric plants and dams*, volume 129.
- Colombo, M. and Comi, C. (2019). A regularized damage model for structural analyses of concrete dams in the presence of alkali-silica reaction. In *COUPLED VIII: proceedings of the VIII International Conference on Computational Methods for Coupled Problems in Science and Engineering*, pages 789–800. CIMNE.
- Comby-Peyrot, I., Bernard, F., Bouchard, P.-O., Bay, F., and Garcia-Diaz, E. (2009). Development and validation of a 3d computational tool to describe concrete behaviour at mesoscale. application to the alkali-silica reaction. *Computational Materials Science*, 46(4):1163–1177.
- Contrafatto, L. and Cuomo, M. (2007). Comparison of two forms of strain decomposition in an elastic-plastic damaging model for concrete. *Modelling and Simulation in Materials Science and Engineering*, 15(4):S405–S423.
- Cuba Ramos, A. I. (2017). *Multi-Scale Modeling of the Alkali-Silica Reaction in Concrete*. PhD thesis, EPFL, Lausanne.

- Curnier, A. (1994). *Computational methods in solid mechanics*, volume 29. Springer Science & Business Media.
- Dai, Y.-H., Liao, L.-Z., and Li, D. (2004). On restart procedures for the conjugate gradient method. *Numerical Algorithms*, 35(2):249–260.
- de Geus, T. W. J., Vondřejc, J., Zeman, J., Peerlings, R. H. J., and Geers, M. (2017). Finite strain FFT-based non-linear solvers made simple. *Comput. Method. Appl. M.*, 318:412–430.
- de Souza Neto, E. A., Peri, D., and Owen, D. R. J. (2008). *Computational Methods for Plasticity*. John Wiley & Sons, Ltd.
- DeJong, M. J., Hendriks, M. A., and Rots, J. G. (2008). Sequentially linear analysis of fracture under non-proportional loading. *Engineering Fracture Mechanics*, 75(18):5042–5056.
- Doitrand, A., Fagiano, C., Irisarri, F.-X., and Hirsekorn, M. (2015). Comparison between voxel and consistent meso-scale models of woven composites. *Composites Part A: Applied Science and Manufacturing*, 73:143–154.
- Dunant, C. F. (2009). *Experimental and modelling study of the alkali-silica-reaction in concrete*. PhD thesis, EPFL, Lausanne.
- Dunant, C. F. and Scrivener, K. L. (2010). Micro-mechanical modelling of alkali-silica-reaction-induced degradation using the amie framework. *Cement and Concrete Research*, 40(4):517 – 525. Special Issue: ICAAR 13, Trondheim, Norway, June 16-20, 2008.
- Dunant, C. F. and Scrivener, K. L. (2012). Effects of uniaxial stress on alkali-silica reaction induced expansion of concrete. *Cement and Concrete Research*, 42(3):567 – 576.
- Eerenstein, W., Mathur, N. D., and Scott, J. F. (2006). Multiferroic and magnetoelectric materials. *Nature*, 442(7104):759–765.
- Eisenlohr, P., Diehl, M., Lebensohn, R., and Roters, F. (2013). A spectral method solution to crystal elasto-viscoplasticity at finite strains. *International Journal of Plasticity*, 46:37 – 53. Microstructure-based Models of Plastic Deformation.
- Eshelby, J. D. (1957). The determination of the elastic field of an ellipsoidal inclusion, and related problems. *P. Roy. Soc. A-Math. Phys.*, 241(1226):376–396.

Bibliography

- Eshelby, J. D. (1959). The elastic field outside an ellipsoidal inclusion. *P. Roy. Soc. A-Math. Phy.*, 252(1271):561–569.
- Falsafi, A., Leute, R. J., Ladecký, M., and Junge, T. (2022). Non-convex, ringing-free, FFT-accelerated solver using an incremental approximate energy functional. *ArXiv*.
- Fernandes, I., Noronha, F., and Teles, M. (2004). Microscopic analysis of alkali–aggregate reaction products in a 50-year-old concrete. *Materials Characterization*, 53(2-4):295–306.
- Frigo, M. and Johnson, S. G. (2005). The design and implementation of FFTW3. *Proceedings of the IEEE*, 93(2):216–231.
- Gaboriaud, F., Nonat, A., Chaumont, D., and Craievich, A. (2002). Aggregation processes and formation of silico-calco-alkaline gels under high ionic strength. *Journal of Colloid and Interface Science*, 253(1):140–149.
- Gallyamov, E., Leemann, A., Lothenbach, B., and Molinari, J.-F. (2022). Predicting damage in aggregates due to the volume increase of the alkali-silica reaction products. *Cement and Concrete Research*, 154:106744.
- Gallyamov, E. R., Ramos, A. C., Corrado, M., Rezakhani, R., and Molinari, J.-F. (2020). Multi-scale modelling of concrete structures affected by alkali-silica reaction: Coupling the mesoscopic damage evolution and the macroscopic concrete deterioration. *International Journal of Solids and Structures*, 207:262–278.
- Ganesh, M. and Morgenstern, C. (2020). A coercive heterogeneous media helmholtz model: formulation, wavenumber-explicit analysis, and preconditioned high-order FEM. *Numerical Algorithms*, 83(4):1441–1487.
- Garcia-Diaz, E., Riche, J., Bulteel, D., and Vernet, C. (2006). Mechanism of damage for the alkali–silica reaction. *Cement and Concrete Research*, 36(2):395 – 400.
- Geers, M. (2004). Finite strain logarithmic hyperelasto-plasticity with softening: a strongly non-local implicit gradient framework. *Computer Methods in Applied Mechanics and Engineering*, 193(30-32):3377–3401.
- Geers, M. G. D., Kouznetsova, V. G., and Brekelmans, W. A. M. (2010). Multi-scale computational homogenization: Trends and challenges. *J. Comput. Appl. Math.*, 234(7):2175–2182.
- Gergelits, T., Mardal, K.-A., Nielsen, B. F., and Strakoš, Z. (2019). Laplacian precondi-

- tioning of elliptic PDEs: Localization of the eigenvalues of the discretized operator. *SIAM Journal on Numerical Analysis*, 57(3):1369–1394.
- Giorla, A. B., Scrivener, K. L., and Dunant, C. F. (2015). Influence of visco-elasticity on the stress development induced by alkali–silica reaction. *Cement and Concrete Research*, 70:1 – 8.
- Gitman, I., Askes, H., and Sluys, L. (2008). Coupled-volume multi-scale modelling of quasi-brittle material. *European Journal of Mechanics - A/Solids*, 27(3):302–327.
- Glasser, L. D. and Kataoka, N. (1981). The chemistry of ‘alkali-aggregate’ reaction. *Cement and Concrete Research*, 11(1):1–9.
- Glasser, L. D. and Kataoka, N. (1982). On the role of calcium in the alkali-aggregate reaction. *Cement and Concrete Research*, 12(3):321–331.
- Golub, G. H. and Van Loan, C. F. (2013). *Matrix computations*. JHU press.
- Göküzüm, F. S. and Keip, M.-A. (2017). An algorithmically consistent macroscopic tangent operator for FFT-based computational homogenization. *International Journal for Numerical Methods in Engineering*, 113(4):581–600.
- He, H. (2010). *Computational Modelling of Particle Packing in Concrete*. PhD thesis, Delft University of Technology.
- Hill, R. (1963). Elastic properties of reinforced solids: some theoretical principles. *Journal of the Mechanics and Physics of Solids*, 11(5):357–372.
- Hill, R. (1965). A self-consistent mechanics of composite materials. *Journal of the Mechanics and Physics of Solids*, 13(4):213–222.
- Hill, R. (1985). On the micro-to-macro transition in constitutive analyses of elastoplastic response at finite strain. In *Mathematical proceedings of the Cambridge philosophical society*, volume 98, pages 579–590. Cambridge University Press, Cambridge University Press (CUP).
- Hobbs, D. W. (1988). *Alkali-silica reaction in concrete*. Thomas Telford Publishing.
- Holzapfel, G. A., Gasser, T. C., and Ogden, R. W. (2000). A new constitutive framework for arterial wall mechanics and a comparative study of material models. *Journal of elasticity and the physical science of solids*, 61(1):1–48.
- Hoover, C. G. and Bažant, Z. P. (2014). Cohesive crack, size effect, crack band and work-of-fracture models compared to comprehensive concrete fracture tests. *International Journal of Fracture*, 187(1):133–143.

Bibliography

- Hsia, C.-Y., Zhu, Y., and Lin, C.-J. (2017). A study on trust region update rules in newton methods for large-scale linear classification. In *Asian conference on machine learning*, pages 33–48. PMLR.
- Junge, T., Falsafi, A., Patweska, L., Leute, R., Ladescky, M., and Zeman, J. (2022). <https://gitlab.com/muspectre/muspectre>.
- Kabel, M., Merkert, D., and Schneider, M. (2015). Use of composite voxels in FFT-based homogenization. *Computer Methods in Applied Mechanics and Engineering*, 294:168–188.
- Kachanov, L. M. (1958). Rupture time under creep conditions. *International Journal of Fracture*, 97(1):11–18.
- Kaßbohm, S., Müller, W. H., and Feßler, R. (2006). Improved approximations of fourier coefficients for computing periodic structures with arbitrary stiffness distribution. *Comp. Mater. Sci.*, 37(1):90–93.
- Keip, M.-A., Steinmann, P., and Schröder, J. (2014). Two-scale computational homogenization of electro-elasticity at finite strains. *Computer Methods in Applied Mechanics and Engineering*, 278:62–79.
- Khorrami, M., Mianroodi, J. R., Shanthraj, P., and Svendsen, B. (2020). Development and comparison of spectral algorithms for numerical modeling of the quasi-static mechanical behavior of inhomogeneous materials. *arXiv:2009.03762*.
- Krajcinovic, D. and Fonseka, G. U. (1981). The continuous damage theory of brittle materials, part 1: General theory. *Journal of Applied Mechanics*, 48(4):809–815.
- Ladecký, M., Pultarová, I., and Zeman, J. (2021). Guaranteed Two-Sided Bounds on All Eigenvalues of Preconditioned Diffusion and Elasticity Problems Solved by the Finite Element Method. *Appl. Math.*, 66(1):21–42.
- Ladecký, M., Leute, R. J., Falsafi, A., Pultarová, I., Pastewka, L., Junge, T., and Zeman, J. (2022a). On the equivalence of projection based FFT-accelerated scheme with FE discretization and the FFT-accelerated preconditioned FE scheme. *Under Preparation*.
- Ladecký, M., Leute, R. J., Falsafi, A., Pultarová, I., Pastewka, L., Junge, T., and Zeman, J. (2022b). Optimal FFT-accelerated finite element solver for homogenization. *arXiv*.
- Ladecký, M., Pultarová, I., Zeman, J., Leute, R. J., Pastewka, L., Falsafi, A., and Junge, T. (2021). Well-conditioned micromechanical solver with FFT-based preconditioner. *in preparation*.

- Lahellec, N., Michel, J. C., Moulinec, H., and Suquet, P. (2003). Analysis of inhomogeneous materials at large strains using fast fourier transforms. In *IUTAM Symposium on Computational Mechanics of Solid Materials at Large Strains*, pages 247–258. Springer Netherlands.
- Lebensohn, R. A. and Needleman, A. (2016). Numerical implementation of non-local polycrystal plasticity using fast fourier transforms. *J. Mech. Phys. Solids*, 97(SI):333–351.
- Léger, P., Côté, P., and Tinawi, R. (1996). Finite element analysis of concrete swelling due to alkali-aggregate reactions in dams. *Computers and Structures*, 60(4):601–611.
- Leuschner, M. and Fritzen, F. (2018). Fourier-accelerated nodal solvers (fans) for homogenization problems. *Computational Mechanics*, 62(3):359–392.
- Leute, R. J., Ladecký, M., Falsafi, A., Jödicke, I., Pultarová, I., Zeman, J., Junge, T., and Pastewka, L. (2021). Elimination of ringing artifacts by finite-element projection in FFT-based homogenization. *arXiv preprint arXiv:2105.03297*.
- Li, A. (2017). *"Micro-architected Metamaterials: Design and Analysis"*. Mechanical engineering research theses and dissertations. 2., Southern Methodist University.
- Lucarini, S. and Segurado, J. (2019a). An algorithm for stress and mixed control in galerkin-based FFT homogenization. *International Journal for Numerical Methods in Engineering*, 119(8):797–805.
- Lucarini, S. and Segurado, J. (2019b). DBFFT: A displacement based FFT approach for non-linear homogenization of the mechanical behavior. *International Journal of Engineering Science*, 144:103131.
- Lucarini, S., Upadhyay, M. V., and Segurado, J. (2021). FFT based approaches in micromechanics: fundamentals, methods and applications. *Modelling and Simulation in Materials Science and Engineering*, 30(2):023002.
- Ma, X., Parvathaneni, K.-K., Lomov, S. V., Vasiukov, D., Shakoor, M., and Park, C.-H. (2019). Quantitative comparison between fast fourier transform and finite element method for micromechanical modeling of composite. In *FiBreMoD Conference*, Leuven, Belgium.
- Ma, X., Shakoor, M., Vasiukov, D., Lomov, S. V., and Park, C. H. (2021). Numerical artifacts of fast fourier transform solvers for elastic problems of multi-phase materials: their causes and reduction methods. *Comput. Mech.*, pages in press, .

Bibliography

- Marvi-Mashhadi, M., Lopes, C., and LLorca, J. (2020). High fidelity simulation of the mechanical behavior of closed-cell polyurethane foams. *Journal of the Mechanics and Physics of Solids*, 135:103814.
- Marzouk, H. and Langdon, S. (2003). The effect of alkali-aggregate reactivity on the mechanical properties of high and normal strength concrete. *Cement and Concrete Composites*, 25(4-5):549–556.
- Mazars, J. (1984). Application of the mechanics of damage to non-linear behavior and the breakage of the structural bevel. *THESIS OF DOCTOR ES SCIENCES PRESENTED AT THE UNIVERSITY PIERRE AND MARIE CURIE-PARIS 6*.
- Mazars, J. and Pijaudier-Cabot, G. (1989). Continuum damage theory—application to concrete. *Journal of Engineering Mechanics*, 115(2):345–365.
- Mean, S., Unami, K., and Fujihara, M. (2020). Level-set methods applied to the kinematic wave equation governing surface water flows. *Journal of Environmental Management*, 269:110784.
- Mehta, P. K. and Monteiro, P. J. (2014). *Concrete: microstructure, properties, and materials*. McGraw-Hill Education.
- Meng, C., Heltsley, W., and Pollard, D. D. (2012). Evaluation of the eshelby solution for the ellipsoidal inclusion and heterogeneity. *Comput. Geosci.*, 40:40–48.
- Miehe, C. (2003). Computational micro-to-macro transitions for discretized microstructures of heterogeneous materials at finite strains based on the minimization of averaged incremental energy. *Computer Methods in Applied Mechanics and Engineering*, 192(5-6):559–591.
- Miehe, C., Schotte, J., and Schröder, J. (1999). Computational micro–macro transitions and overall moduli in the analysis of polycrystals at large strains. *Computational Materials Science*, 16(1-4):372–382.
- Milton, G. W. (1995). The theory of composites. *Materials and Technology*, 117:483–93.
- Milton, G. W. and Sawicki, A. (2003). Theory of composites. cambridge monographs on applied and computational mathematics. *Appl. Mech. Rev.*, 56(2):B27–B28.
- Moes, N., Dolbow, J., and Belytschko, T. (1999). A finite element method for crack growth without remeshing. *International Journal for Numerical Methods in Engineering*, 46(1):131–150.

- Mori, T. and Tanaka, K. (1973). Average stress in matrix and average elastic energy of materials with misfitting inclusions. *Acta Metallurgica*, 21(5):571–574.
- MotahariTabari, S. and Shooshpasha, I. (2018). Evaluation of coarse-grained mechanical properties using small direct shear test. *Int. J. Geotech. Eng.*, 15(6):667–679.
- Moulinec, H. and Suquet, P. (1994). A fast numerical method for computing the linear and nonlinear properties of composites. *C. R. Acad. Sci. II B-Mec.*, 318:1417–1423.
- Moulinec, H. and Suquet, P. (1998). A numerical method for computing the overall response of nonlinear composites with complex microstructure. *Comput. Method. Appl. M.*, 157(1):69–94.
- Multon, S. and Toutlemonde, F. (2006). Effect of applied stresses on alkali-silica reaction-induced expansions. *Cement and Concrete Research*, 36(5):912 – 920.
- Mura, T. (1982). *Micromechanics of Defects in Solids*. Kluwer Academic Publishers Group.
- Müller, W. H. (1996). Mathematical vs. experimental stress analysis of inhomogeneities in solids. *J. Phys. IV France*, 06(C1):139–148.
- Nemat-Nasser, S. and Hori, M. (2013). *Micromechanics: overall properties of heterogeneous materials*. Elsevier.
- Nocedal, J. and Wright, S. (2006). *Numerical optimization*. Springer Science & Business Media.
- Norris, A. (1985). A differential scheme for the effective moduli of composites. *Mechanics of Materials*, 4(1):1–16.
- Pan, J. W., Feng, Y. T., Wang, J. T., Sun, Q. C., Zhang, C. H., and Owen, D. R. J. (2012). Modeling of alkali-silica reaction in concrete: a review. *Frontiers of Structural and Civil Engineering*, 6(1):1–18.
- Papilloud, S. (2019). Lenouvelliste.ch, <https://www.lenouvelliste.ch/>.
- Pari, M., Rots, J. G., and Hendriks, M. (2022). Recent advancements in sequentially linear analysis (SLA) type solution procedures. In *Computational Modelling of Concrete and Concrete Structures*, pages 432–442. CRC Press.
- Petersen, K. B., Pedersen, M. S., et al. (2008). The matrix cookbook. *Technical University of Denmark*, 7(15):510.
- Peterson, K., Gress, D., Dam, T. V., and Sutter, L. (2006). Crystallized alkali-silica gel in concrete from the late 1890s. *Cement and Concrete Research*, 36(8):1523–1532.

Bibliography

- Pijaudier-Cabot, G. and Bažant, Z. P. (1987). Nonlocal damage theory. *J. Eng. Mech.*, 113(10):1512–1533.
- Pippig, M. (2013). PFFT: An extension of FFTW to massively parallel architectures. *SIAM Journal on Scientific Computing*, 35(3):C213–C236.
- Ponce, J. and Batic, O. (2006). Different manifestations of the alkali-silica reaction in concrete according to the reaction kinetics of the reactive aggregate. *Cement and Concrete Research*, 36(6):1148–1156.
- Powell, M. J. D. (1977). Restart procedures for the conjugate gradient method. *Mathematical programming*, 12(1):241–254.
- Pultarová, I. and Ladecký, M. (2021). Two-sided guaranteed bounds to individual eigenvalues of preconditioned finite element and finite difference problems. *Numerical Linear Algebra with Applications*, 28(5):e2382.
- Ramyar, K., Çopuroğlu, O., Andıç, Ö., and Fraaij, A. (2004). Comparison of alkali-silica reaction products of fly-ash- or lithium-salt-bearing mortar under long-term accelerated curing. *Cement and Concrete Research*, 34(7):1179–1183.
- Rizzi, E. (1991). Fracture-energy based regularization of a scalar damage model. *Atti Ottavo Convegno Italiano di Meccanica Computazionale, AIMETA*, pages 107–112.
- Rots, J. (2001). Sequentially linear continuum model for concrete fracture. *Fracture mechanics of concrete structures*, 2:831–840.
- Rots, J. G., Belletti, B., and Invernizzi, S. (2008). Robust modeling of rc structures with an “event-by-event” strategy. *Engineering Fracture Mechanics*, 75(3-4):590–614.
- Rots, J. G. and Invernizzi, S. (2004). Regularized sequentially linear saw-tooth softening model. *International journal for numerical and analytical methods in geomechanics*, 28(7-8):821–856.
- Rüter, M. O. (2019). Numerical integration. In Rüter, M. O., editor, *Error Estimates for Advanced Galerkin Methods*, pages 149–170. Springer International Publishing, Cham.
- Saad, Y. (2003). *Iterative Methods for Sparse Linear Systems*. Society for Industrial and Applied Mathematics.
- Schlangen, E. and Çopuroğlu, O. (2007). Concrete damage due to alkali-silica reaction: a new method to determine the properties of expansive gel. *Fracture mechanics of concrete and concrete structures—high-performance concrete, brick-masonry and environmental aspects*. Taylor & Francis Group, London, pages 1835–1841.

- Schneider, M. (2021). A review of nonlinear FFT-based computational homogenization methods. *Acta Mech.*, pages in press, .
- Schneider, M., Merkert, D., and Kabel, M. (2016a). FFT-based homogenization for microstructures discretized by linear hexahedral elements. *International Journal for Numerical Methods in Engineering*, 109(10):1461–1489.
- Schneider, M., Ospald, F., and Kabel, M. (2016b). Computational homogenization of elasticity on a staggered grid. *Int. J. Numer. Meth. Eng.*, 105(9):693–720.
- Schröder, J. (2014). *A numerical two-scale homogenization scheme: the FE2-method*, pages 1–64. Springer Vienna, Vienna.
- Sellier, A., Grimal, É., Multon, S., and Bourdarot, E. (2017). *Swelling concrete in dams and hydraulic structures: DSC 2017*. John Wiley & Sons.
- Sethian, J. A. (1996). A fast marching level set method for monotonically advancing fronts. *P. Natl. Acad. Sci. USA*, 93(4):1591–1595.
- Simo, J. (1992). Algorithms for static and dynamic multiplicative plasticity that preserve the classical return mapping schemes of the infinitesimal theory. *Computer Methods in Applied Mechanics and Engineering*, 99(1):61–112.
- Simo, J. C. and Hughes, T. J. (2006). *Computational inelasticity*, volume 7. Springer Science & Business Media.
- Sluys, L. (1997). Discontinuous modeling of shear banding. *Computational plasticity: Fundamentals and applications*, pages 735–744.
- Sonon, B., Francois, B., and Massart, T. (2012). A unified level set based methodology for fast generation of complex microstructural multi-phase rves. *Computer methods in applied mechanics and engineering*, 223:103–122.
- Stanton, T. E. (1942). Expansion of concrete through reaction between cement and aggregate. *Transactions of the American Society of Civil Engineers*, 107(1):54–84.
- Steihaug, T. (1983). The conjugate gradient method and trust regions in large scale optimization. *SIAM Journal on Numerical Analysis*, 20(3):626–637.
- Sukumar, N., Moes, N., Moran, B., and Belytschko, T. (2000). Extended finite element method for three-dimensional crack modelling. *International Journal for Numerical Methods in Engineering*, 48(11):1549–1570.
- Suwito, A., Jin, W., Xi, Y., and Meyer, C. (2002). A mathematical model for the pessimum size effect of ASR in concrete. *Concrete Science and Engineering*, 4(13):23–34.

Bibliography

- Swamy, R. (1991). *The Alkali-Silica Reaction in Concrete*. Blackie Glasgow.
- Swamy, R. N. and Al-Asali, M. M. (1988). Engineering properties of concrete affected by alkali-silica reaction. *ACI Materials Journal*, 85(5).
- Vakulenko, A. and Kachanov, M. (1971). Continuum theory of medium with cracks [in russian], *izv. AN SSSR, MTT*, 4:159–166.
- Vidyasagar, A., Tan, W. L., and Kochmann, D. M. (2017). Predicting the effective response of bulk polycrystalline ferroelectric ceramics via improved spectral phase field methods. *J. Mech. Phys. Solids*, 106:133–151.
- Vondřejc, J. and de Geus, T. (2017). Energy-based comparison between fourier-galerkin and finite element method within numerical homogenisation. *arXiv preprint arXiv:1709.08477*, 8.
- Vondřejc, J., Zeman, J., and Marek, I. (2014). An FFT-based Galerkin method for homogenization of periodic media. *Comput. Math. Appl.*, 68(3):156–173.
- Walker, H. N., Lane, D. S., and Stutzman, P. E. (2006). Petrographic methods of examining hardened concrete: A petrographic manual, revised 2004. Revised manual, federal Highway administration.
- Widom, B. (1966). Random sequential addition of hard spheres to a volume. *The Journal of Chemical Physics*, 44(10):3888–3894.
- Willot, F. (2015). Fourier-based schemes for computing the mechanical response of composites with accurate local fields. *C. R. Mécanique*, 343(3):232–245.
- Willot, F., Abdallah, B., and Pellegrini, Y.-P. (2014). Fourier-based schemes with modified green operator for computing the electrical response of heterogeneous media with accurate local fields. *Int. J. Numer. Meth. Engng.*, 98(7):518–533.
- Yvonnet, J. (2019). *Computational homogenization of heterogeneous materials with finite elements*, volume 258. Springer.
- Zdenek, Bažant, and Steffens, A. (2000). Mathematical model for kinetics of alkali-silica reaction in concrete. *Cement and Concrete Research*, 30(3):419 – 428.
- Zeman, J., de Geus, T. W. J., Vondřejc, J., Peerlings, R. H. J., and Geers, M. G. D. (2017). A finite element perspective on nonlinear FFT-based micromechanical simulations. *Int. J. Numer. Meth. Eng.*, 111(10):903–926.
- Zeman, J., Vondřejc, J., Novák, J., and Marek, I. (2010). Accelerating a FFT-based

solver for numerical homogenization of periodic media by conjugate gradients. *Journal of Computational Physics*, 229(21):8065–8071.

Glossary

1D 1-dimensional. x, 79, 80, 82

2D 2-dimensional. xiii, xiv, 10, 40, 41, 47, 72, 73, 77, 81, 83, 93, 98–100, 107, 108, 113, 115, 116, 119, 122, 124, 125, 127, 128

3D 3-dimensional. 40, 42, 47, 77, 107, 133

ASR alkali-silica reaction. iii, iv, ix, 1–5, 11, 27, 29–35, 54, 67, 79, 86, 89, 90, 98, 104–106, 110, 115–119, 121–125, 127–129, 131–134

CG conjugate gradient. iii, 3, 25–27, 55, 56, 61, 71, 72, 77, 78, 82, 85–88, 93, 95, 101

DFT discrete Fourier transform. 9

DoF degree of freedom. 12, 13, 15, 57, 62, 63

EPFL Ecole Polytechnique Fédérale de Lausanne. 125, 131, 133

FAIEF first order approximation incremental energy functional. 72, 76, 77, 86, 133

FD finite difference. 5, 90, 95, 96, 101–104, 106, 132

FE finite element. 4, 5, 9, 12, 18, 19, 22, 23, 25, 27, 37, 54–56, 64, 67, 81, 105, 119, 125–129, 133

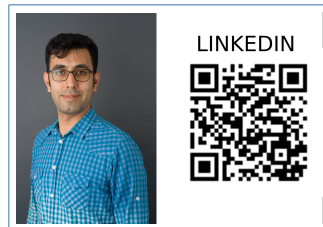
FE² FE squared. 2, 33–35, 105

FEM finite element method. iii, iv, 2, 3, 5, 7–9, 12, 16, 18, 20, 22, 31, 34, 35, 37, 55, 56, 71, 90, 106, 115, 118, 125, 129, 132, 134

- FFT** fast Fourier transform. iii, iv, 2–5, 8, 12, 13, 27, 35, 37, 38, 53–56, 58, 64, 71, 90, 103, 105, 111, 117, 119, 128, 131, 132, 134
- FG** Fourier-Galerkin. 15, 90, 117
- HPC** high-performance computing. 133
- LBFGS** limited-memory Broyden–Fletcher–Goldfarb–Shanno. 71, 78, 86, 133
- LS** level set. 107, 108, 119
- PCG** preconditioned conjugate gradient. 25, 26, 58, 61, 63, 64
- PDE** partial differential equation. iv, 8, 132
- PSD** positive semi definite. 76
- RSA** random sequential addition. 107, 108, 119
- RVE** representative volume element. xi, 2, 5, 8, 13, 14, 23, 25, 32, 34, 35, 38, 39, 46–51, 55, 57, 60–62, 64, 65, 71, 74, 82, 89–91, 93, 95–100, 102, 103, 105–108, 117–119, 121–125, 129, 131–134
- SLA** sequential linear algorithm. 34, 35, 125
- SNPSD** symmetric non-positive semi definite. 71, 73, 80, 119
- SPSD** symmetric positive semi definite. 27, 71
- TR** trust-region. 71, 72, 74–80, 82, 84–86
- TRM** trust-region method. 72, 73

Ali Falsafi

Av. de Beaumont 5
1012, Lausanne
Switzerland
☎ +41 78 229 0022
✉ ali.falsafi@epfl.ch
in [afalsafi](#)



23-Feb-1991

More Info: My publications: [My Google Scholar](#) and my experiences: [My LinkedIn](#), and [My Gitlab](#)

Key Competencies

- Doctoral researcher in computational mechanics and mechanical engineer by training
- Expert in computer programming and software development (6 years of coding experience)
- Expert in data science and machine learning (projects on real world data)

Education (Mechanical Engineering)

- 2018-Now **PhD, EPFL, LAMMM**, École Polytechnique Fédérale de Lausanne, Switzerland.
Thesis Title *Efficient Multi-Scale Modeling of Alkali-Silica-Reaction Damage in Concrete*
- 2013–2016 **Master, Sharif University of Technology(SUoT)**, Tehran, Iran, *summa cum laude*.
Thesis Title *Modeling of Interactions between Scanning Probe Microscopy Tip in Trolling Mode and Environment*
- 2009–2013 **Bachelor, Shiraz University**, Shiraz, Iran, *summa cum laude*.
Thesis Title *Control of under-actuated pole and cart system*

Experience

- 03.2018 – 08.2022 **Researcher, μ Spectre Developer, EPFL**, coded in **C++**, 1000x faster than conventional FEM, **Python** interface developed using **Pybind**, **Multi-OS/Multi-compiler** compatibility maintained through **CI/CD** pipelines running unit tests on **Docker** containers, collaboration with researchers from Prague and Freiburg University.
Contribution: Development and implementation of
- FFT-accelerated ringing-free homogenization scheme and its equivalent FEM formulation
 - Non-convex solvers applicable in computational homogenization
 - Fast/efficient ASR model (real-world use case of the developed methodology and machinery)
- 03.2021 – 08.2021 **Senior Data Scientist manager, Managing Scrum teams (JIRA)** to process and analyze marketing data to make recommendation for companies and businesses using **Google Analytics**, **Python**, **Pandas**, and **Scikit**, CREWASIS, 5 months, part-time.
- 03.2019–03.2021 **Courses at EPFL**, Parallel programming, Scientific programming for engineers, Applied data analysis, Deep learning, Machine learning for engineers.
- 08.2015 – 10.2015 **Internship**, Developing particle based model for intestinal tissue growth using **C** programming language, Jülich Forschungszentrum, 3 months.

Projects (links to projects' source available by clicking on their title and also in my linkedin)

- 2019 **Particles Simulator**, 5 **C++** core projects on applying scientific programming for engineering.
- 2019 **Different thread based Paralleling methods**, Comparison of different thread based parallelization methods such as **OpenMP**, **Intel Thread Building Block**, and **C++17 threads**.
- 2020 **Time, Temperature, and Mobility**, Data analysis on the location data from two social media vs. weather data and holiday, using **Pandas** and **Scikit**.
- 2021 **Deep learning framework**, Implementing a deep-learning framework from scratch, **Python**.
- 2021 **NN architectures**, Examined different archs for classification-comparison task, using **Pytorch**.
- 2021 **Clinical Data Analysis**, Statistical analysis of clinical data on COVID-19 patients with acute kidney injury, using **Pandas** and **Scikit**.

Skills

Computer Skills

Coding and programming	Git, C++, Python, OpenMP, MPI parallel programming	● ● ● ● ●
General	Dockers, Linux, Windows, SLURM, L ^A T _E X, Office	● ● ● ● ●

Data Science Skills

Data Analysis and Big Data	Pandas, Seaborn, Spark, Apache, ...	● ● ● ● ●
Machine Learning	Scikit, Statsmodel	● ● ● ● ●
Deep Learning	PyTorch, TensorFlow, Jax, Flex (CNN, RNN, Attention models, ...)	● ● ● ● ●

Mechanical Engineering Skills

Solid Mechanics	FEM Simulation, FFT-based RVE solvers	● ● ● ● ●
Particle Based model	Molecular and coarse-grained simulations (LAMMPS,...)	● ● ● ● ●

Soft Skills

- Dedicated team player with good communication skills
- Hardworking and Flexible
- Troubleshooting skills

Honors & Awards

- 2016 Ranked 1st among 126 classmates in Master, Sharif University of Technology, GPA: 19.13/20.00
- 2013 Ranked 1st among 113 classmates in Bachelor, Shiraz University, GPA: 18.51/20.00
- 2012 Ranked 14th among 500 participants in National Mechanical Engineering Olympiad (top 3%)
- 2008 Ranked 318th in National Entrance exam among over 200,000 participants (top 0.02%)

Languages

English: Proficient **Deutsch:** Intermediate(B2) **Français:** Beginner(A1) **Persian:** Native

Others

- Hobbies: ○ Hiking, Solo Traveling, Podcasts, Cooking, Volleyball (University team at SUoT)
- Voluntary activities: ○ Member of Iranian Student Association (IRSA) Committee

Publications

Ali Falsafi, Till Junge, and et al. Non-convex, ringing free, fft-accelerated solver using an incremental approximate energy functional. *arXiv*.

Ali Falsafi and Hossein Nejat Pishkenari. Martini coarse-grained model of solid-liquid interface. *The Journal of Physical Chemistry C*, 120(46):26259–26269, 2016.

Ali Falsafi and Hossein Nejat Pishkenari. A many-body dissipative particle dynamics study of nanoneedle-liquid interface. *Journal of Applied Physics*, 124(21):214301, 2018.

Richard J. and Ali Falsafi et al. Elimination of ringing artifacts by finite-element projection in fft-based homogenization, 2021.

Ladescky M. and Ali Falsafi et al. Optimal fft-accelerated finite element solver for homogenization, 2022.

Thahereh Sabaghian, et al, and Ali Falsafi. Prognostic factors in patients with aki and covid-19. *Under Review*, 2021.